Doctoral Thesis

Generation Mechanism of Low-Energy Electron Precipitation in Pulsating Aurora Elucidated with Arase Satellite, Ground-Based Optical and Radar Observations, and Computed Tomography

Mizuki Fukizawa

Department of Geophysics

Graduate School of Science

Tohoku University

Thesis Committee Members

Associate Professor Takeshi Sakanoi (Chair, Supervisor)

Professor Yuto Katoh

Professor Yasumasa Kasaba

Associate Professor Fuminori Tsuchiya

Professor Yoshizumi Miyoshi (Nagoya Univ.)

Specially Appointed Associate Professor Yoshimasa Tanaka (NIPR)

2021

博士論文

あらせ衛星と地上光学・レーダー観測ならびに コンピュータ・トモグラフィによる 脈動オーロラ中の低エネルギー電子降下現象の解明

吹澤 瑞貴

東北大学大学院理学研究科

地球物理学専攻

論文審査委員

坂野井 健 准教授 (指導教員 · 主査)

加藤 雄人 教授

笠羽 康正 教授

土屋 史紀 准教授

三好 由純 教授 (名古屋大学)

田中 良昌 特任准教授 (国立極地研究所)

令和 3 年

Acknowledgments

The present dissertation has been achieved through the doctoral course of the Department of Geophysics, Graduate School of Science, Tohoku University.

During the present research, I have been supported by many people. Firstly, I would like to thank Associate Professor Takeshi Sakanoi, who was my supervisor since I was an undergraduate student. He has provided a lot of support to me and he has introduced me to several researchers inside and outside the university.

Regarding my research using the Arase satellite, I am deeply grateful to Professor Yoshizumi Miyoshi, Nagoya University, and Dr. Yoichi Kazama, at Institute of Astronomy and Astrophysics. Prof. Miyoshi has supported me since I was a Master's student, and he provided me with very meaningful discussions on my research. Whenever I got stuck, his advice paved the way. Dr. Kazama gave very meaningful comments to my research; especially, his comments about particle data have improved the quality of my work.

Regarding research using the EISCAT radar, I am deeply grateful to Associate Professor Yasunobu Ogawa at the National Institute of Polar Research (NIPR): his extensive and deep knowledge on the ionosphere and his keen insights on the EISCAT data have greatly contributed to my research. Also, he took me to Tromsø and let me experience personally the operation of the EISCAT radar, which was very valuable for me.

Regarding research using the Aurora Computed Tomography, I am deeply grateful to Specially Appointed Associate Professor Yoshimasa Tanaka at NIPR: he has been very helpful, from the preparation of analysis tools to interpretation of analysis results. Thanks to his keen insights into the inverse problem, I was able to successfully reconstruct the two- and three-dimensional distributions of precipitating electrons and pulsating auroral patches.

Regarding research on pulsating auroras, I am deeply grateful to Professor Keisuke Hosokawa and Associate Professor Takuo T. Tsuda at University of Electro-Communications. Thanks to their deep knowledge and careful consideration, I was able to deeply discuss the results of my study.

I am also grateful to Professors Yasumasa Kasaba and Takahiro Obara, Associate Professors Hiroaki Misawa and Fuminori Tsuchiya, Assistant Professor Masato Kagitani, Professor Emeriti Shoichi Okano and Akira Morioka for their helpful suggestions during seminars and meetings in the Planetary Plasma and Atmospheric Research Center (PPARC) at Tohoku University.

I am also grateful to all members of PPARC, Space and Terrestrial Plasma Physics (STPP) Laboratory, and Planetary Atmospheric Physics (PAT) Laboratory at Tohoku University for their suggestions and discussions through associated seminars of Space Physics and Planetary Science Group in Tohoku University.

I would like to express my gratitude to the secretaries of PPARC, Ms. Yukari Kanno, and Ms. Hiromi Arihara for their continuous supports. I am also grateful to the secretary of STPP, Ms. Kimiko Saijo, for her support in business trips and participation in scientific meetings.

Science data of the ERG (Arase) satellite were obtained from the ERG Science Center operated by ISAS/JAXA and ISEE/Nagoya University (https://ergsc.isee.nagoya-u.ac.jp/index.shtml.en, [Miyoshi *et al*., 2018a]). In Chapter 2, we used MGF-L2 v03_03 [Matsuoka *et al*., 2018a], PWE/OFA-L2 v02_01 data [Kasahara *et al*., 2018d], and LEPe-L1 version 6 (calibrated, equivalent to L2 v02_02 using MGF-L2 v03_03). In Chapter 3, we used the LEPe Level-1a v7 data (calibrated, identical to Level-2 v03_01 data), PWE/OFA L2-v02_01 data [Kasahara *et al*., 2018d], PWE/HFA L3-v03_05, v03_06, v03_07, v04_05, and v04_06 data [Kasahara *et al*., 2021] and MGF L2-v03_04 and v04_04 data [Matsuoka *et al*., 2018a] obtained by ERG. The ERG orbital data L2-v02 [Miyoshi *et al*., 2018b] and L3-v02 [Miyoshi *et al*., 2018c] were also used. The SPEDAS software [Angelopoulos *et al*., 2019] and ERG plug-in tools were used for data analysis in this study. The work in Chapter 4 was performed using data from NIPR. The electron density and temperature data used in this study are a part of the EISCAT database in the NIPR, which is available at http://polaris.nipr.ac.jp/~eiscat/eiscatdata/. EISCAT is an international association supported by research organizations in China (CRIRP), Finland (SA), Japan (NIPR), Norway (NFR), Sweden (VR), and the United Kingdom (UKRI). The database construction for the imager data at Skibotn and the EISCAT radar data has been supported by the IUGONET (Inter-university Upper atmosphere Global Observation NETwork) project (http://www.iugonet.org/). The all-sky images used in Chapter 4 are available at http://pc115.seg20.nipr.ac.jp/www/AQVN/evs1.html. The spectrograph data are available at http://ttt01.cei.uec.ac.jp/sg01/. We thank Kirsti Kauristie, Kellinsalmi Mirjam, and Carl-Fredrik Enell for maintaining the Magnetometers Ionospheric Radars All-sky Cameras Large Experiment camera network and data flow.

The author is a Research Fellow (DC) of Japan Society for the Promotion of Science (JSPS). The studies in Chapters 2 and 3 are the joint research program of the Institute for Space-Earth Environmental Research (ISEE), Nagoya University, and are also supported by JSPS Bilateral Open Partnership Joint Research Projects (JPJSBP120192504), JSPS KAKENHI Grant Numbers JP15H05815, JP17H00728, JP17K05672, JP18H03727, JP20H01959, and JP20J11829. The research in Chapter 5 is also supported by JSPS KAKENHI Grant Numbers JP17K05672, JP20J11829, and JP21H01152.

Finally, I am deeply grateful to my family. Thanks to their devoted support, I have been able to live my life as I wish.

Abstract

In the inner magnetosphere of the Earth, various plasma waves are excited by wave–particle interactions. Lower band chorus (LBC) waves scatter $\sim$10 keV electrons into a loss cone by the cyclotron resonance, and cause pulsating auroras (PsAs). On the other hand, upper band chorus (UBC) waves cause stable precipitations at $\sim$1 keV. Furthermore, electrostatic electron cyclotron harmonic (ECH) waves scatter a few hundred eV to a few keV electrons. In recent decades, observations and theories regarding LBC waves have been developed, and the relationship between LBC waves and PsAs has been almost revealed. However, there has been no observational evidence that ECH waves actually scatter electrons into a loss cone. In addition, the relationship between PsAs and low-energy ($<$ a few keV) electron precipitation caused by UBC or ECH waves has not been fully understood.

In this study, we aim to understand the following subjects. (1) Observational evidence of the scattering of electrons into a loss cone by ECH waves. (2) Statistical analysis to examine the energy dependence and occurrence rate of pitch angle (PA) scattering by LBC, UBC, and ECH waves. (3) How often the *F* region electron density enhancement caused by soft electron precipitation occurs as associated with PsAs. (4) Reconstruction of three-dimensional (3-D) distribution of volume emission rate (VER) and horizontal distribution of precipitating electrons in a PsA patch. Results for each subject are summarized as follows.

(1) To verify whether ECH waves scatter electrons into a loss cone, we compared the ECH wave intensity with the electron flux inside the loss cone obtained with the Arase satellite. The cross-correlation coefficient between the ECH wave intensity and the loss cone electron flux at an energy of $\sim$5 keV was statistically significant, while that with LBC wave intensity at the same energy was small. We calculated the PA diffusion coefficient of ECH waves, assuming that the wave normal angle is 87.0°, and the electron temperature is 1 eV. We found that the diffusion coefficient of 5-keV electrons is 10 times larger than that of other energies where cross-correlation coefficients were small. The linear growth rate of ECH waves is also large when the wave normal angle and electron temperature satisfy these conditions. We demonstrated that the electron flux correlated with the ECH wave intensity would cause the 557.7-nm auroral emissions, with an emission rate of 200 R according to a model calculation. As a result, we verified for the first time the observational evidence of PA scattering of electrons into a loss cone by ECH waves.

(2) From the statistical analysis of wave and electron data obtained with the Arase satellite from March 24, 2017 to August 31, 2020, we examined the characteristics of the strong electron scattering by LBC, UBC, and ECH waves, in the energy range from 0.1 to 20 keV. We revealed that the energy ranges where LBC, UBC, and ECH waves contribute to scatter electrons into loss cones are as follows. The regression

line slopes for wave amplitudes versus loss cone filling ratios are positive, while correlation coefficients between them are statistically significant in the energy range greater than $\sim$2 keV for LBC, of $\sim$1–10 keV for UBC, and smaller than $\sim$2 keV for ECH waves. In these energies, the occurrence rate of the strong PA scattering was also high for each wave. These energies are consistent with those predicted by the quasi-linear theory, in the case that PA diffusion coefficients exceed the strong diffusion level. We clarified from the statistical analysis of the Arase data that a few keV electron precipitation scattered by ECH waves was not common, while electrons with energy less than 1 keV were commonly scattered by ECH waves.

(3) We conducted two case studies to investigate the relationship between the electron density height profile and auroral type, such as discrete, diffuse, and pulsating aurora, using the data obtained with the EISCAT radar and an auroral all-sky imager at Tromsø on February 18, 2018 and October 27, 2019. We also carried out statistical studies on 14 events to clarify how often the F region electron density enhancement occurs as associated with PsAs. We consequently found that 76% of electron density height profiles showed a local peak in the F region with an electron temperature enhancement. Compared with the model ionization profiles by electron precipitation, we suggest that 76% of these local peaks were caused by precipitating electrons in the energy range lower than 100 eV. The occurrence rate of these profiles exceeded 80% in the range of 22–3 magnetic local time. We suggest that the electron density enhancement in the F region would be caused by the low-energy electrons scattered by ECH waves in the magnetosphere.

(4) We reconstructed for the first time the 3-D VER and horizontal distribution of precipitating electrons in a PsA patch by Aurora Computed Tomography (ACT). All-sky images at 427.8-nm auroral emission obtained at Abisko, Kilpisjärvi, and Skibotn have been used. We improved the previous ACT used for discrete auroras to apply diffuse and dimmer PsAs in the following three points: first, the subtraction of background diffuse aurora from auroral images before conducting ACT, secondly, the estimation of the relative sensitivity between all-sky cameras, and third, the determination of hyperparameters of the regularization term. As a result, we succeeded to reconstruct the 3-D VER and horizontal distribution of precipitating electrons in the PsA patch. The characteristic energy of the reconstructed precipitating electron flux ranges from 6 to 23 keV, while the peak altitude of the reconstructed VER ranges from 90 to 104 km, consistently with previous studies. We found that the horizontal distribution of precipitating electron's characteristic energy was neither uniform nor stable in the PsA patch during the pulsation. The observed spatial and temporal variations of PsAs are important to understand the background magnetic and plasma conditions that would cause changes in the cyclotron resonance energy of LBC waves in the magnetospheric source region. Our reconstruction results are a great advantage of multiple ground-based data, since such 3-D distributions cannot be obtained by rockets and satellites. We quantitively evaluated the reconstruction results using a model PsA patch with adding artificial noises, and compared with the ionospheric electron density observed by the EISCAT radar. Considering the time derivative term in the electron continuity equation, the electron density was reconstructed with sufficient accuracy even when the PsA intensity decreased from $\sim$1 to $\sim$0.1

kR. If the time derivative term is not considered, the electron density rapidly decreases as the PsA intensity decreases. This result suggests that the time derivative term should be considered when we derive the electron density associated with PsAs from the continuity equation.

Contents

List of Figures

List of Tables

1 Introduction

The present research focuses on pulsating auroras (referred to as PsAs), which are caused by wave–particle interaction near the magnetic equator of Earth's inner magnetosphere. In this chapter, we describe the general characteristics of the Earth's magnetosphere as a source region of PsAs, and we review past studies on the morphology and generation mechanism of PsAs. A general description of Earth's magnetosphere is described in Section 1.1 [Ono and Miyoshi, 2012, and references therein] and references therein; the substorm, which is closely related to PsAs, is introduced in Section 1.2; a detailed PsAs review is given in Section 1.3. Furthermore, waves that could cause PsAs, as well as chorus and electrostatic electron cyclotron harmonic (ECH) waves are introduced in Sections 1.4 and 1.5. The wave–particle interaction near the magnetic equator is reviewed in Section 1.6. Previous studies on our research topic are reviewed in Section 1.7. Section 1.8 describes the purpose of this thesis.

1.1 Magnetosphere of the Earth

The Earth is one of the planets in our solar system with an intrinsic magnetic field. The dipole magnetic field, whose magnetic moment is 8.05×10^{22} A m^2, is often used to assume the Earth magnetic field. More in detail, the magnetosphere is the area controlled by the planetary magnetic field: several studies on this topic have been conducted over the past hundred years [Russell, 1991, and references therein]. The dipole model well describes the configuration of magnetic field near the Earth. The precise configuration of magnetosphere, which is shown in Figure 1.1, is rather complicated, due to the interaction with solar wind and other factors. The solar wind speed generally exceeds the sound speed: therefore, a shock front, called bow shock, is generated and, in its downstream side, the solar wind is slowed down. This region is called the magnetosheath, while the boundary between magnetosheath and magnetosphere is called magnetopause. Plasma processes at the bow shock convert some of the bulk flow energy into the thermal energy of plasma. Typical temperature of ions and electrons in the magnetosheath is $\sim$100 and $\sim$30 eV, respectively. The magnetosphere shape depends on the strength of planetary magnetic field and solar wind flow. The solar wind dynamic pressure causes a compression of Earth's magnetosphere at the dayside of the magnetopause, while the solar wind flow stretches field lines radially behind the Earth and forms the magnetotail, which consists of two lobes of opposite polarity of magnetic field, and represent regions of low-density plasma ($\sim$0.01 cm^{-3}), which directly connects the solar wind with polar cap ionosphere through the mantle. Under sunlit conditions, both thermal-energy ions and ionospheric photoelectrons, which are generated by ioniza-

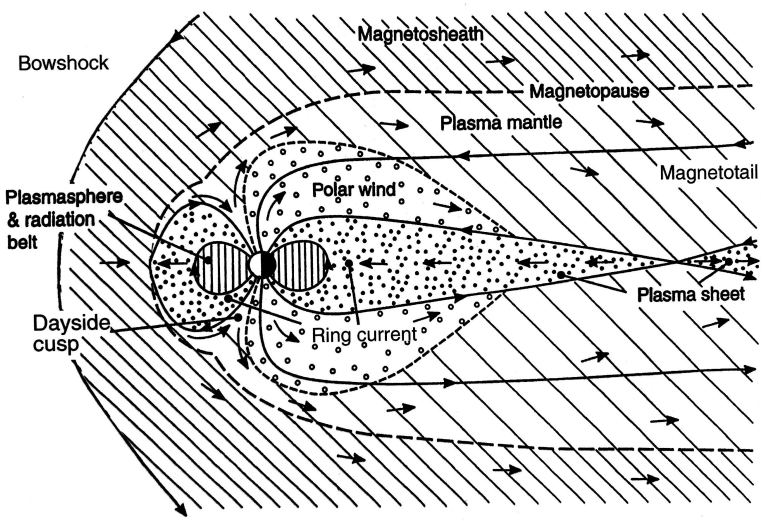

Figure 1.1. Schematic illustration of the Earth's magnetic field, in which plasma regions are indicated [Cowley, 1995]. Solid arrowed lines indicate magnetic field, the thick long-dashed line indicates the magnetopause, while arrows represent the direction of plasma flow. Diagonal hatching indicates plasma in, or directly derived from, the solar wind or magnetosheath. Outflowing ionospheric plasma is indicated by open circles; solid dots indicate hot plasma accelerated in the tail, while the vertical hatching shows the corotating plasmasphere.

tion of the atmosphere by solar extreme ultraviolet radiation, escape along the open field lines in the polar cap: this ambipolar diffusion process is one of the most fundamental processes which cause ion outflow, and is referred to as polar wind. On the other hand, the thin region in the nightside of the magnetotail, which separates field lines of two lobes, is referred to as neutral or current sheet. Typically, its thickness is 4–8$R_{\rm E}$, where $R_{\rm E}$ is the Earth radius. In this neutral sheet, the magnetic field strength is minimal, while the plasma density is maximal ($\sim$0.1–1 cm^{-3}). Magnetic reconnection takes place in the nightside neutral sheet (at a distance range of 20–25$R_{\rm E}$) and plasma is accelerated toward the Earth [e.g., Nagai *et al*., 1998]: this accelerated flow is sometimes called bursty bulk flow (BBF) [McPherron *et al*., 1973, Miyashita *et al*., 2009].

From low to high electron energies, the Earth's energy regimes in the inner magnetosphere are the plasmasphere (several eV), ring current ($\sim$1–100 keV), and radiation belts ($>$100 keV) (Figure 1.2). The region from $\sim$1 to $\sim$8$R_{\rm E}$ is called inner magnetosphere. Both the ring current and radiation belt play an important role on energy transfer, dynamics, and on acceleration and deceleration of magnetospheric plasmas. More in detail, the ring current is the torus-like region where particles carrying the current mainly consist of ions with energy of several tens of keV and of electrons with energy of $\sim$10 keV at a distance of $\sim$3–8$R_{\rm E}$. On the other hand, the plasmasphere is the region where the number density of low energy (several eV) charged particle is high ($\sim$10^3 cm^{-3}). The density sharply drops to approximately several cm^{-3} at a distance of $\sim$4$R_{\rm E}$ [Carpenter and Park, 1973]: this boundary is referred to as plasmapause. Additionally, regions in the magnetosphere where high energy (more than a few hundred keV) charged particles are trapped in the

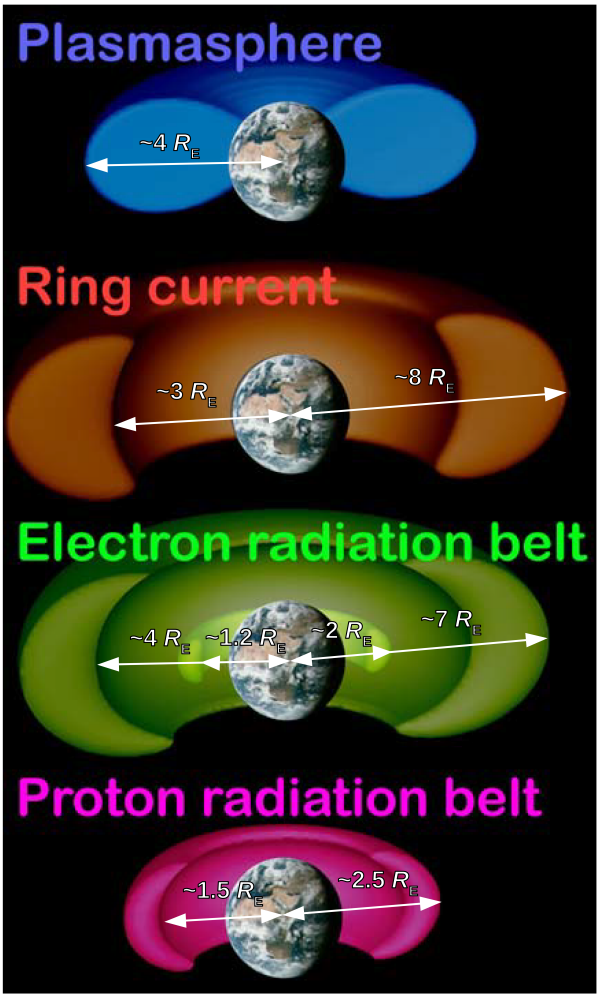

Figure 1.2. Energy structures of charged particles trapped in the inner magnetosphere [after Ebihara and Miyoshi, 2011].

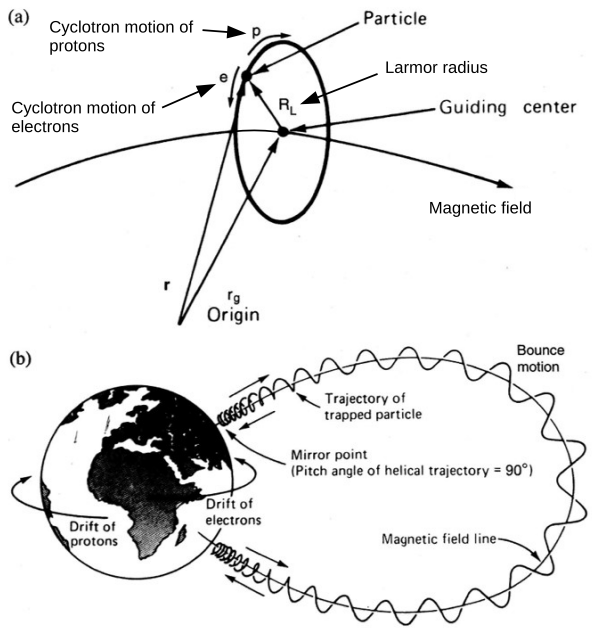

Figure 1.3. Motion of charged particles: (a) cyclotron (gyro), (b) bounce along a field line, and drift motions around the Earth [after Lyons and Williams, 1984].

dipole magnetic field are called radiation or Van Allen belts [Van Allen and Frank, 1959]: these consist of inner ($\sim$1.2–2$R_{\rm E}$) and outer ($\sim$4–7$R_{\rm E}$) radiation belts [e.g., Thorne *et al*., 2007]. The electron flux of space between them is small: this region is called slot region [Lyons and Thorne, 1973]. On the other hand, the proton or ion radiation belts consist of a single belt at a distance of $\sim$1.5–2.5$R_{\rm E}$ [e.g., Looper *et al*., 2005]. The particles in radiation belts gyrate around and bounce up and down along magnetic field lines, while they drift around the Earth (Figure 1.3).

1.2 Substorm

Substorm represents an important phenomena for the dynamics of magnetosphere and for spatial and temporal variations of aurora, and it has been studied using satellite and ground-based observation data, theories, and numerical modeling [e.g., Akasofu, 1991]. When the direction of the interplanetary magnetic field becomes southward, the magnetic reconnection is promoted at the dayside magnetopause, and the magnetospheric convection is enhanced. In this case, the magnetic field flux in the lobe is enhanced, the neutral sheet becomes thin, and the magnetic field is stretched toward the anti-sunward. In the ionosphere, one or more auroral arcs gradually move equatorward: this period is called growth phase of substorm, and continues for about 1 hour (Figure 1.4A). This phase suddenly transits to the expansion phase, and, at this timing, the most equatorward arc begins to increase its brightness (initial brightening) (Figure 1.4B), and then it expands to the poleward and east-westward (auroral breakup) (Figure 1.4C). The start time of expansion phase (substorm onset) is usually defined by that of the initial brightening. The overall region

where auroral arcs expand poleward is called auroral bulge, while the westward expansion of bulges is called westward traveling surge. While active discrete auroral arcs appear at higher latitudes after the poleward expansion, diffuse auroras appear mainly at lower latitudes (Figure 1.4D). Eventually, the aurora ceases to expand poleward (Figure 1.4E), and starts to dim and become more homogeneous, thus ending the expansion phase, and starting the recovery phase (Figure 1.4F). In the morning sector, diffuse auroral patches begin to blink quasi-periodically. These patches are PsAs [e.g., Omholt, 1957].

At the beginning of the expansion phase, a magnetic neutral line is formed, and the magnetic reconnection occurs between 20 and $25R_{\mathrm{E}}$ in the nightside neutral sheet [e.g., Nagai *et al*., 1998]. Plasma is accelerated in the neutral line, and an earthward plasma flow (BBF), whose velocity is more than 400 km/s, is generated [Baumjohann *et al*., 1990]. The magnetic field line, which is stretched at the growth phase, returns to the original configuration (dipolarization). Ions and electrons with energies of tens to hundreds keV are injected from the plasma sheet to the inner magnetosphere [e.g., Baker *et al*., 1982], and then move to the dusk and dawnside, respectively, due to the gradient-$\mathbf{B}$ and curvature drift.

1.3 Pulsating Aurora

PsAs are a subset of diffuse auroras, which play an important role on the magnetosphere-ionosphere coupling system, since they dominantly carry 84% of the energy flux from the magnetosphere into the ionosphere during low solar wind driving conditions and 71% during high solar wind driving conditions [Newell *et al*., 2009]. In particular, PsAs show characteristic modulations in their luminosity [e.g., Lessard, 2012]; they typically appear immediately after the substorm onset in the equatorward part of auroral oval, and are continuously observed mainly in the morning side during the recovery phase of substorms. PsAs are composed of luminous patches of irregular shape (Figure 1.5), having a horizontal size of $\sim$10–200 km [e.g., Royrvik and Davis, 1977]. The drift speed of patches is consistent with the $\mathbf{E} \times \mathbf{B}$ drift speed, suggesting that the patch structure corresponds to the cold plasma density distributions in the magnetosphere [Nakamura and Oguti, 1987]. PsAs are known to have two dominant periodicities: main (a few to a few tens of second), and higher-frequency internal modulations (a few Hertz, known as 3 Hz modulation) [e.g., Royrvik and Davis, 1977]. Yamamoto [1988] reported that the pulsation ON and OFF times of the main modulation were 6.2 ± 1.7 s and 14.5 ± 5.3 s, respectively. By applying principal component analysis (PCA) to time series image data of PsAs, Nishiyama *et al*. [2016] showed that the internal modulation was excited only in substructures embedded in a whole PsA patch. In this thesis, we focus on the main pulsation.

The emission altitude of aurora has been investigated through either ground-based stereoscopic imaging or measurement of electron density profiles. Auroral stereoscopy is based on the triangulation from two locations with the base distance of $\sim$10 km. Stenbaek-Nielsen and Hallinan [1979] estimated that the emission altitude of PsAs ranges from 83 to 135 km with a mean altitude of 98.5 km, while Brown *et al*. [1976] estimated that it ranges from 82 to 105 km with a median altitude of 92 km (Figure 1.6). A primary

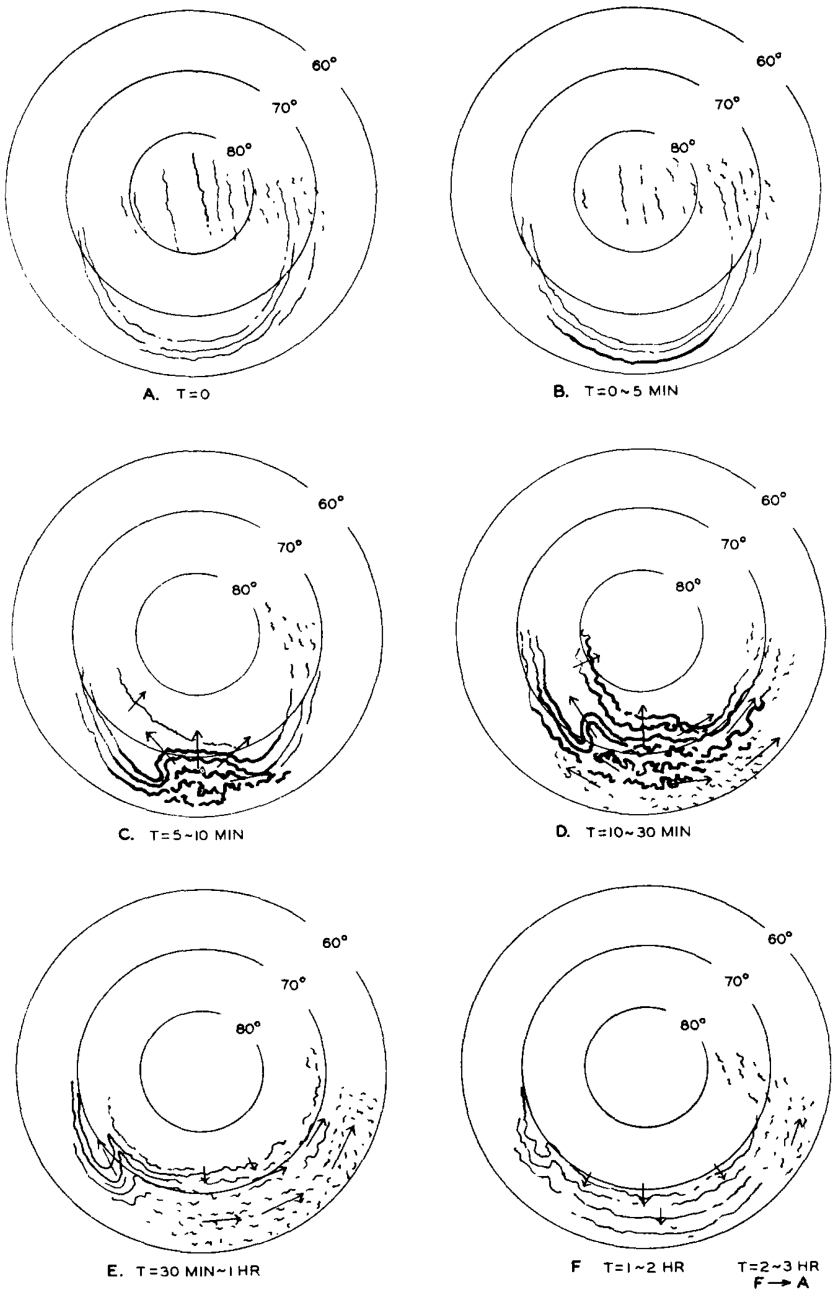

Figure 1.4. Schematic illustration of the development of auroral substorm. The center of concentric circles in each stage is the north geomagnetic pole, while the sun is toward the top of diagram [Akasofu, 1964].

Figure 1.5. A picture of PsA patches taken by Fukizawa at Poker Flat Research Range at 13:35 UT on March 22, 2018.

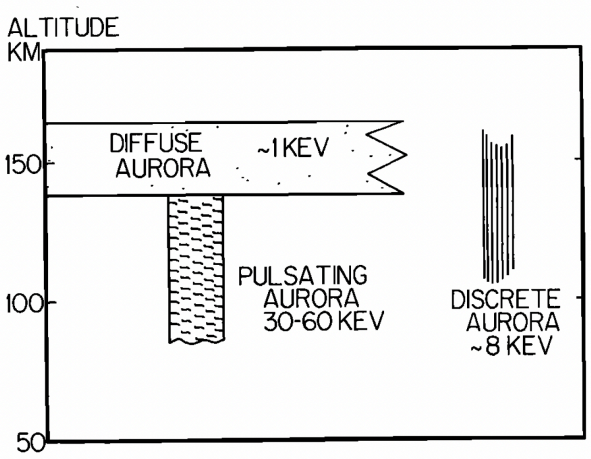

Figure 1.6. Schematic illustration of the altitude differences between discrete, diffuse, and pulsating aurora [Brown *et al.*, 1976].

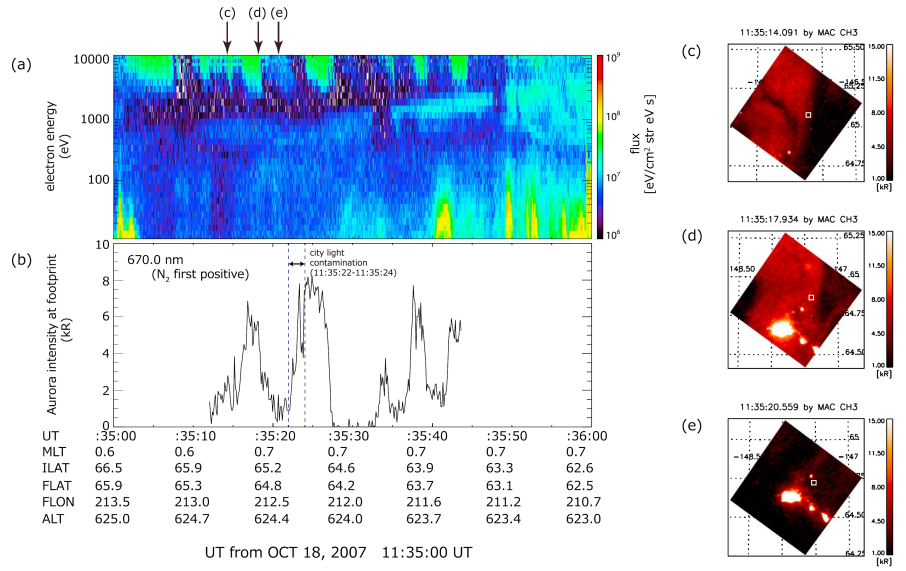

Figure 1.7. Summary plot of Reimei satellite observations on October 18, 2007 [Miyoshi *et al*., 2015b].

electron energy near 30 keV is required to reach 92 km altitude, while energy near 60 keV is required to produce the lowest altitude of 82 km [Rees, 1963]. PsAs are often embedded in a background diffuse aurora: its emission altitude was estimated to be near 150 km (Figure 1.6), which is caused by about 1-keV electron precipitation. Kataoka *et al*. [2016] performed for the first time stereoscopic imaging observation of PsAs with 100-fps speed: they used two sCMOS cameras with a narrow field lens ($15^\circ \times 15^\circ$). As a result, the PsA emission altitude was estimated to be 85–95 km. Furthermore, Jones *et al*. [2009] showed that the electron density profile associated with PsA patches had a thickness of 15–25 km, by using the data taken by the incoherent scatter radar at Poker Flat.

Precipitating electrons that cause PsAs have been investigated by observations with sounding rockets and low-altitude satellites: Figure 1.7 shows the energy-time spectrogram of precipitating electrons and simultaneous aurora image obtained by the Reimei satellite [Miyoshi *et al*., 2015b]. Reimei was located at 0.6 to 0.7 magnetic local time (MLT), at invariant latitudes (ILATs) from 66.5 to 62.6 (L =6.3 to 4.7), and at an altitude of $\sim$620 km; the satellite identified clear modulations of electron flux above 2.4 keV. As shown in Figure 1.7b, the periodic auroral intensifications at the footprint of magnetic field through the satellite have been identified at the wavelength of 667 nm (N_2 first positive band) from the multispectral auroral imaging camera (MAC) [Obuchi *et al*., 2008, Sakanoi *et al*., 2003] observations at 11:35:12 UT to 11:35:45 UT, when the footprint existed within the field of view of MAC. Note that there are city light contaminations in the images at 11:35:22 UT to 11:35:24 UT. Figures 1.7c, 1.7d, and 1.7e show auroral images at the timings of (c), (d), and (e) shown in Figures 1.7a; Figures 1.7c and 1.7d correspond to the images for the on time of PsAs; Figure 1.7e corresponds to the period without auroral emissions, although most of the area overlaps with Figure 1.7d; Figures 1.7d and 1.7e show that modulations above a few keV represent a main driver of the PsA, since a clear one-to-one correspondence between the precipitation and

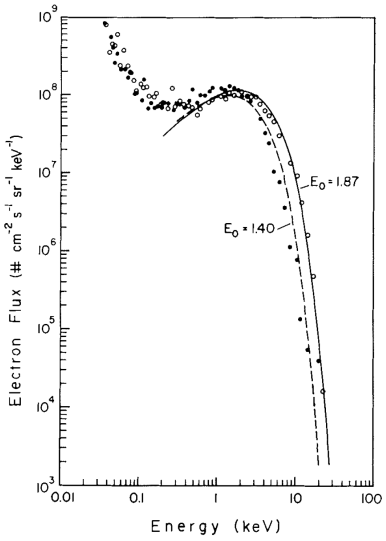

Figure 1.8. Typical electron spectra recorded by a rocket during a pulsation maximum at 11:47:11 UT (circles) showing its fit to a Maxwellian energy distribution with E_0=1.87 keV (solid line). It is compared with a spectrum recorded during a pulsation minimum at 11:47:01.98 UT (dots) with E_0=1.40 keV (dashed line) [McEwen *et al.*, 1981]

optical emission with a modulation period of a few seconds has been observed. On the other hand, electron precipitation near 1 keV is stable. These low-energy electrons would cause the background diffuse aurora accompanied by PsAs. Modulations of precipitating electrons near 10 keV and stable electron precipitation near 1 keV have also been reported using sounding rocket observations [McEwen *et al.*, 1981, Sandahl *et al.*, 1980, Smith *et al.*, 1980].

The generation mechanism of PsAs has been inferred from electron energy spectra [e.g., McEwen *et al.*, 1981]: examples of spectra associated with PsAs are shown in Figure 1.8. The rocket was launched at 11:43:24 UT on February 15, 1980, from Southend, Saskatchewan, and flew into the typical PsA with an emission intensity of $\sim$0.5–1 kR and background intensity of 275 R at N_2^+ 427.8 nm, showing $\sim$17 s pulsations. It was noted that the spectra were in general extremely well fitted by a Maxwellian energy distribution, expressed with $N = N_0 E \exp(-E/E_0)$, where N is total number flux, N_0 is a constant source density, E is electron energy, and E_0 is the characteristic energy: the latter was estimated by a least mean square fitting the Maxwellian to the spectral data ranging from 0.3 to 22 keV. The electron energy spectra, associated with PsAs, are primarily Maxwellian, and suggest that there is no acceleration by parallel electric fields, whereas typical electron spectra associated with discrete auroras show mono-energetic peaks, which imply the acceleration process caused by parallel electric fields (Figure 1.9). Thus, it is suggested that electrons precipitations which cause PsAs are not accelerated by parallel electric field but probably caused by pitch-angle (PA) scattering process near the magnetic equator. There are two candidates for the interaction between waves and electrons to cause PsAs: chorus, and ECH waves [e.g., Kennel *et al.*, 1970, Lyons, 1974, Nishimura *et al.*, 2010, 2011].

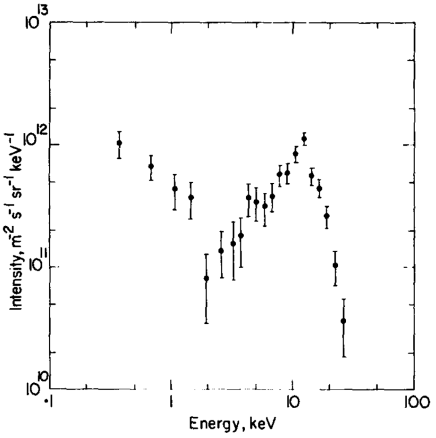

Figure 1.9. A typical electron spectrum recorded by a rocket during an auroral arc [Bryant *et al.*, 1978].

1.4 Chorus Waves

Chorus waves are electromagnetic and right-handed polarized whistler mode waves, which characteristically have two frequency bands, a lower (0.1–$0.5 f_{\text{ce\_eq}}$), where $f_{\text{ce\_eq}}$ is equatorial electron cyclotron frequency, and an upper band (0.5–$0.8 f_{\text{ce\_eq}}$), with a minimum wave power near $0.5 f_{\text{ce\_eq}}$. These are naturally excited in the low-density region outside the plasmapause, in association with the injection of plasma sheet hot electrons into the inner magnetosphere [Burtis and Helliwell, 1976, Meredith *et al.*, 2001, 2003, Tsurutani and Smith, 1974]. In the magnetic equatorial region, the ambient magnetic field intensity increases as the distance from the Earth decreases. The velocity distribution function of injected hot electrons becomes anisotropic due to the conservation of first adiabatic invariant μ as given by

$$\mu = mv_{\perp}^2/2B, \tag{1.1}$$

where m is the mass of electron, B is the ambient magnetic field intensity, and $v_{\perp}$ is the velocity of electron perpendicular to the ambient magnetic field. Anisotropic electrons drive an instability generating a band of whistler mode waves [Kennel and Petschek, 1966, Summers *et al.*, 2009, 2011], which play an essential role in triggering the generation of whistler mode chorus waves. The dispersion relation of whistler mode waves in cold plasma can be written as [Gurnett and Bhattacharjee, 2005]

$$c^2k^2 = \omega^2 + \frac{\omega - \omega_p^2}{\omega_c - \omega}, \tag{1.2}$$

where c is the speed of light, k is wave number, ω is wave frequency, ω_{c} is cyclotron frequency, and ω_{p} is plasma frequency. The linear growth rate of whistler mode waves γ is given by

$$\gamma = \pi\omega_{\text{ce}}\left(1 - \frac{\omega}{\omega_{\text{ce}}}\right)\eta(V_{\text{R}})\left[A(V_{\text{R}}) - \frac{1}{(\omega_{\text{ce}}/\omega - 1)}\right], \tag{1.3}$$

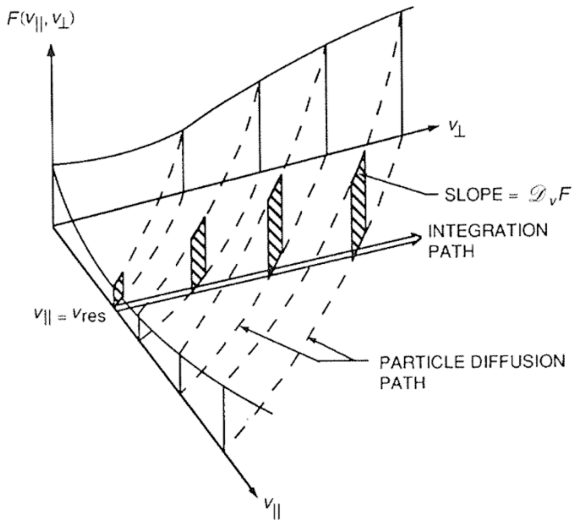

Figure 1.10. Schematic illustration of integration path of Eq. 1.4 [Walt, 1994].

where ω is the angular frequency, $\omega_{\rm ce}$ is the electron cyclotron angular frequency, $V_{\rm R}$ is the resonance velocity, and η is a positive definite factor given by

$$\eta = 2\pi\frac{\omega_{\rm ce}-\omega}{k}\int_0^\infty v_\perp dv_\perp f(v_\perp,\, v_\parallel = V_{\rm R}), \tag{1.4}$$

where f is the velocity distribution function, $v_\parallel$ is the velocity of electrons parallel to the ambient magnetic field [Swift, 1981]. The factor η is simply the fraction of particles that resonate with the wave according to the cyclotron resonance

$$\omega - k_\parallel v_R = n\omega_{\rm ce}, \tag{1.5}$$

where k is the wave number, and n is a positive integer. A schematic illustration of integration path is shown in Figure 1.10. The function A in Eq. 1.3 is the anisotropy factor

$$A = \left.\frac{\int_0^\infty v_\perp dv_\perp \tan(\alpha(\partial f/\partial\alpha))}{2\int_0^\infty v_\perp dv_\perp f}\right|_{v_\parallel = V_{\rm R}}, \tag{1.6}$$

where α is the PA

$$\alpha = \tan^{-1}(v_\perp/v_\parallel). \tag{1.7}$$

For the simple case in which f has the discontinuous loss cone form

$$f(v_\parallel,\, v_\perp) = \left(\frac{m}{2\pi k_B T}\right)^{3/2}\exp\left[-\frac{m}{2k_B T}(v_\parallel^2+v_\perp^2)\right] \qquad (\alpha>\alpha_0), \tag{1.8}$$

$$f(v_\parallel,\, v_\perp) = 0 \qquad (\alpha<\alpha_0), \tag{1.9}$$

the growth rate is given by

$$\gamma = \pi^{1/2}\omega_{ce}V_R\left(\frac{m}{2k_BT}\right)^{1/2}\left(1-\frac{\omega}{\omega_{ce}}\right)^2 \cdot \exp\left[-\frac{mV_R^2}{2k_BT}\sec^2(\alpha_0)\right]\left[A(V_R)-\frac{1}{\omega_{ce}/\omega-1}\right], \tag{1.10}$$

and the anisotropy factor can be written as

$$A = \frac{mV_R^2}{2k_BT}\tan(\alpha_0)\sec^2(\alpha_0), \tag{1.11}$$

where α_0 is a loss cone angle, k_B is the Boltzmann constant, and T is temperature. To excite whistler mode waves, γ in Eq. 1.10 must be positive ($\gamma > 0$). Under this condition, A must exceed 0.33 when we assume that $\omega = \omega_\mathrm{ce}/4$, which is a typical frequency of lower-band chorus (LBC) waves. When A exceeds 0.33, the term $mV_\mathrm{R}^2/2k_\mathrm{B}T$ in Eq. 1.11 becomes large, because of the small factor $\tan(\alpha_0)$. When the term $mV_\mathrm{R}^2\sec{\alpha_0}^2/2k_\mathrm{B}T$ in Eq. 1.10 is large, γ in Eq. 1.3 is too small to excite whistler mode waves. For example, we assume $\alpha_0 = 1$–3°, the term $mV_\mathrm{R}^2/2k_\mathrm{B}T$ becomes $\sim$6–19 and $\gamma/\omega_\mathrm{ce}$ becomes $\sim 1.5\times10^{-3}$–3.4×10^{-9}.

On the other hand, for the case where f is a two-temperature Maxwellian,

$$f = \left(\frac{m}{2\pi k_BT_\parallel}\right)^{1/2}\frac{m}{2\pi k_BT_\perp}\exp\left[-\frac{m}{2k_B}\left(\frac{v_\parallel^2}{T_\parallel}+\frac{v_\perp^2}{T_\perp}\right)\right], \tag{1.12}$$

the anisotropy factor can be written as

$$A = \frac{T_\perp}{T_\parallel}-1. \tag{1.13}$$

From Eq. 1.3, when we assume that $\gamma > 0$ and $\omega = \omega_\mathrm{ce}/4$,

$$A(V_\mathrm{R})-\frac{1}{\omega_\mathrm{ce}/\omega-1} = \frac{T_\perp}{T_\parallel}-\frac{4}{3} > 0. \tag{1.14}$$

This suggests that temperature anisotropy ($T_\perp > 4T_\parallel/3$) excites whistler mode waves.

When we consider cold and warm plasma, the linear growth rate of whistler waves is large when the cold plasma density is enhanced [e.g., Cuperman and Landau, 1974]. Fu *et al*. [2014] showed that a warm (a few hundred eV) anisotropy drives the quasi-electrostatic upper band chorus (UBC), while a hot (a few keV) anisotropy derives electromagnetic LBC, by using Van Allen Probes observations and particle-in-cell simulations (Figure 1.11).

Whistler mode chorus waves are mainly generated in the dawn sector, since electrons drift to the dawn side due to the gradient-$\mathbf{B}$ and curvature drift (Figure 1.12). Meredith *et al*. [2012] statistically analyzed data from five satellites (Dynamics Explorer1, Combined Release and Radiation Effects (CRRES), Cluster 1, Equatorial satellite (TC-1), Time History of Events, and Macroscale Interactions during Substorms

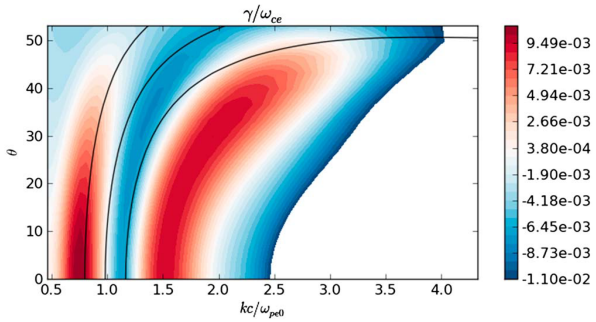

Figure 1.11. Growth rate of whistler mode chorus waves on the basis of a kinetic linear theory using observed parameters, except for temperature anisotropies [Fu *et al.*, 2014].

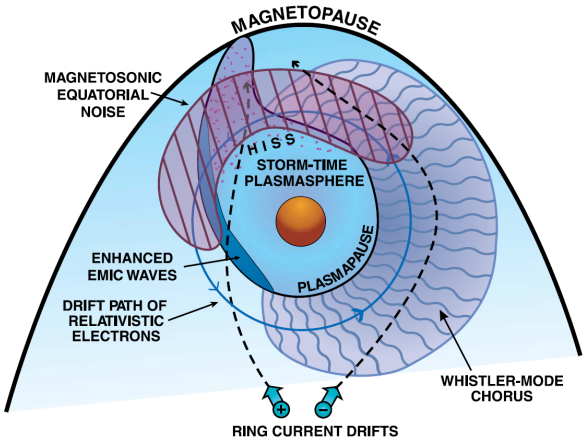

Figure 1.12. Schematic illustration of the spatial distribution of important waves in the inner magnetosphere in relation to the plasmasphere, the drift-paths of ring current electrons, ions (10–100 keV), and relativistic electrons ($\geq$0.3 MeV) [Thorne, 2010].

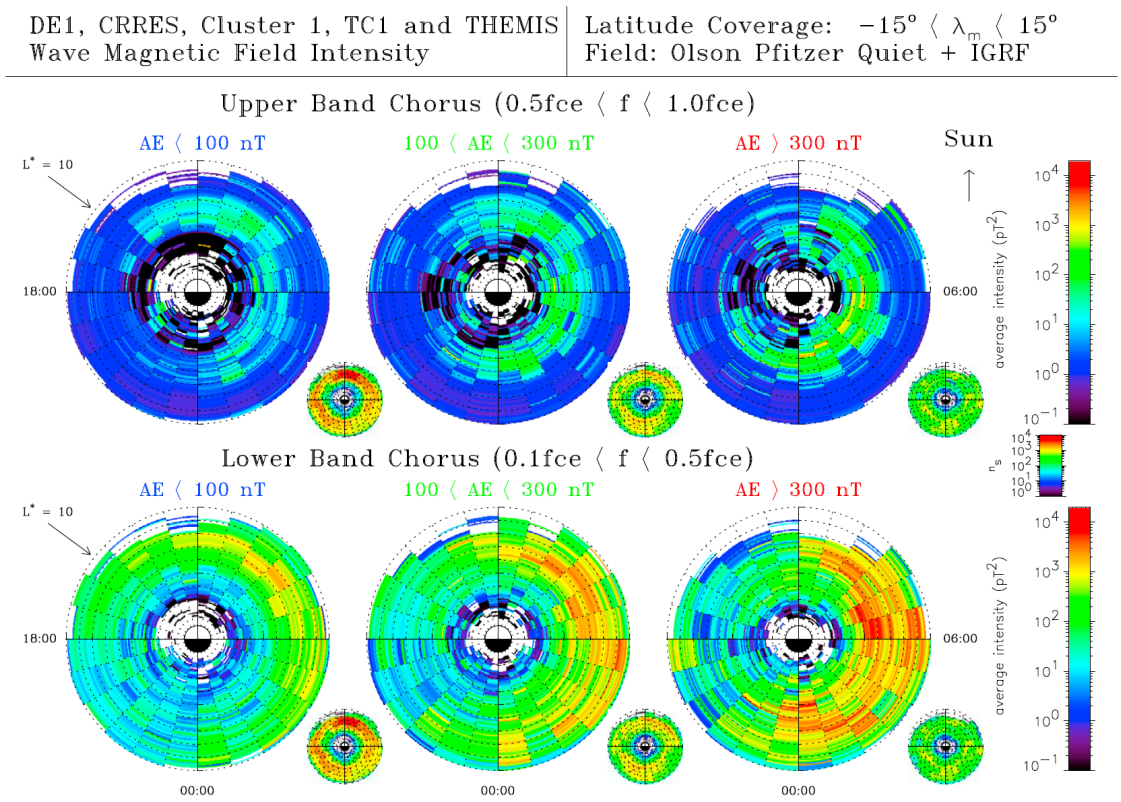

Figure 1.13. Combined satellite model of the equatorial wave intensity for (top) UBC and (bottom) LBC as a function of L^*, MLT, and geomagnetic activity. Average intensities are shown in the large panels, while corresponding sampling distributions in the small panels [Meredith *et al.*, 2012].

(THEMIS)), and investigated a global distribution of LBC and UBC. They found that equatorial LBC is strongest during geomagnetically active conditions with peak intensities in the order of 2000 pT^2 in the region of $4 < L^* < 9$ between 23:00 and 12:00 MLT, while equatorial UBC is both weaker and less extensive with peak intensities in the order of a few hundred pT^2 during active conditions between 23:00 and 11:00 MLT from $L^* = 3$ to $L^* = 7$ (Figure 1.13). The Roederer-L shell, L^*, is given by [Roederer, 1970]

$$L^* = \frac{2\pi k_0}{R_\mathrm{E}\Phi}, \tag{1.15}$$

where k_0 is the dipole moment value and Φ is the third adiabatic invariant

$$\Phi = \oint \mathbf{B} \cdot d\mathbf{S}. \tag{1.16}$$

Average UBC and LBC wave intensities for the evening to dawn sectors (21–06 MLT) are shown in Figure 1.14 as a function of the radial distance from the center of the Earth projected on the plane of the magnetic equator (r), Solar Magnetospheric (SM) coordinate system z, and geomagnetic activity: UBC (Figure 1.14, top) occurs predominantly in the region $3 < L^* < 7$, and is tightly confined to the equatorial plane, mostly lying within $6°$ of the magnetic equator, while LBC (Figure 1.14, bottom) covers a large region of geospace,

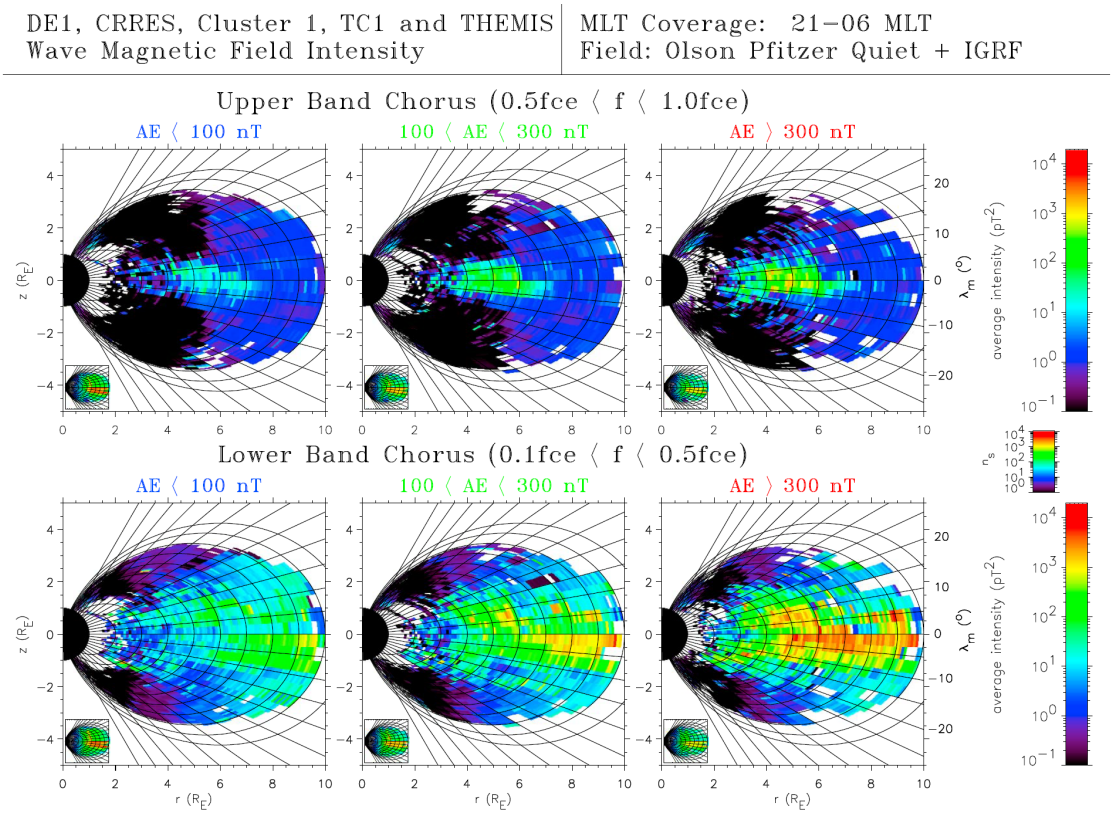

Figure 1.14. Combined satellite model result of the distribution of wave intensity for (top) UBC and (bottom) LBC as a function of radial distance from the center of the Earth projected in the Solar Magnetospheric (SM) coordinate system, and geomagnetic activity for the 21–06 MLT sector. Average intensities are shown in the large panels, while corresponding sampling distributions in the small panels [Meredith *et al.*, 2012].

extending from $4 < L^* < 10$. The largest LBC intensities in this region are seen during geomagnetically active conditions, and are confined to within about 12° latitude centering the magnetic equator.

A typical electric spectrum of UBC and LBC waves measured by the VAP spacecraft is shown in Figure 1.15 (top). UBC and LBC emission are separated by a gap at approximately $\omega_{ce}/2$ (denoted by the white dashed line), where ω_{ce} is calculated using local magnetic field. Quasi-periodic UBC and LBC bursts were observed: their period was like that of the quasi-periodic modulation of pulsating auroral luminosity. Figures 1.15a and 1.15b show the spectra of electric and magnetic fluctuations, respectively. The ellipticity and propagation angle of waves, as shown in Figures 1.15c and 1.15d, demonstrate that both lower and upper bands have the right-hand polarization characteristic of whistlers, but LBC propagates at directions quasi-parallel to B_0 with $\theta \leq 20^\circ$ (where θ is the angle between wave number vector **k** and B_0), while UBC has a predominantly oblique propagation, with $40^\circ \leq \theta \leq 60^\circ$. Furthermore, UBC is quasi-electrostatic, with a propagation angle close to the resonance cone angle $\theta_{res} \approx 57^\circ$ for $\omega = 0.55\omega_{ce}$, where $\theta_{res} \equiv \cos(\omega/\omega_{ce})^{-1}$. The resonance cone is defined as the locus of points where the index of refraction goes to infinity. The combination of parallel LBC and oblique UBC is commonly observed in magnetospheric banded chorus, as shown in several statistical studies [e.g., Agapitov *et al*., 2012, Li *et al*., 2013]. Several rising tone elements were embedded in each LBC burst. Observationally, whistler mode chorus usually consists of discrete elements with rising or falling tones and sometimes short impulsive bursts [e.g., Burtis and Helliwell, 1969, Burton and Holzer, 1974, Hayakawa *et al*., 1984, Li *et al*., 2011, Santolík *et al*., 2003]. Burtis and Helliwell [1976] showed that rising, falling, and constant frequency tones, as well as hooks were observed respectively with a ratio of 77%, 16%, 12%, and 5% of samples. Miyoshi *et al*. [2015b] showed that a train of rising tone elements embedded in LBC bursts drives the internal modulations, while a close set of UBC waves causes the stable precipitations at ∼1 keV (Figure 1.16).

1.5 Electrostatic Electron Cyclotron Harmonic Waves

ECH waves are electrostatic Bernstein mode waves observed in bands between the harmonics of local electron cyclotron frequency (f_{ce_loc}), and are sometimes called $(n+1/2)f_{ce\_loc}$ waves, since emissions tend to appear in narrow bands close to odd integral half-harmonics of f_{ce_loc} [Kennel *et al*., 1970]. Notably, the wave frequency is not centered exactly at half-harmonics of f_{ce} [Zhou *et al*., 2017]. Typical spectra of ECH waves are shown in Figure 1.17. The dispersion relation of Bernstein mode waves is given by [Bernstein, 1958]

$$1 - \sum_{n=1}^{\infty} \frac{2\omega_{pe}^2}{\beta_{ce}^2 \omega_{ce}^2} \frac{\exp(-\beta_{ce}^2 I_n(\beta_{ce}^2))}{(\omega/n\omega_{ce})^2 - 1} = 0, \tag{1.17}$$

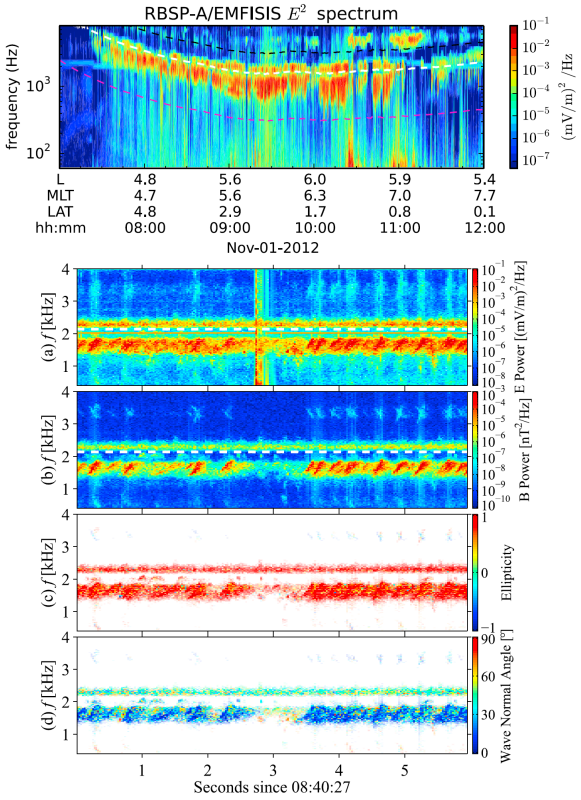

Figure 1.15. (top) The electric field spectrogram measured by the VAP spacecraft from 07:00 UT to 12:00 UT on November 1, 2012. Magenta, white, and black curves denote $0.1f_{ce}$, $0.5f_{ce}$, and f_{ce}, respectively. (bottom) The spectrogram of fluctuating (a) electric and (b) magnetic fields observed with the burst mode from 8:40:27 to 8:40:33 UT. A gap appears near half of the local electron cyclotron frequency f_{ce}, denoted by white dashed lines. (c) Ellipticities and (d) propagation angles of the waves [Fu *et al.*, 2014].

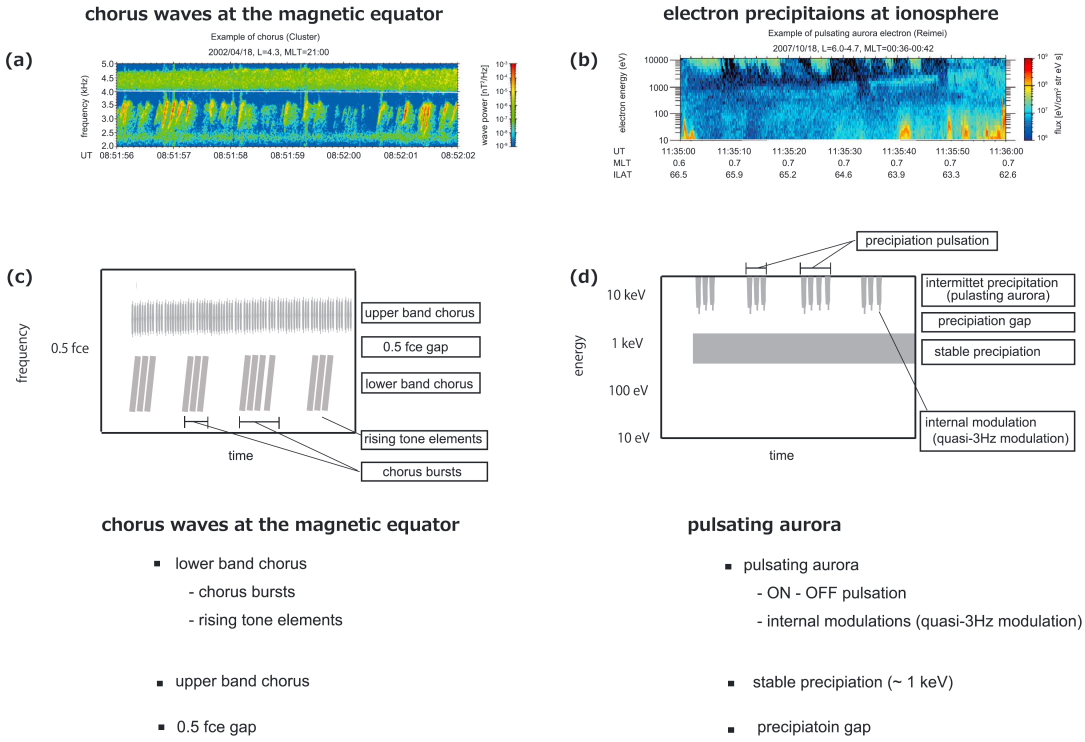

Figure 1.16. (a) Example of chorus frequency spectrum observed by the Cluster satellite. (b) Example of energy spectrum which cause the PsA observed by the Reimei satellite. (c–d) Schematic diagram indicating the relationship between the frequency spectrum of chorus waves and the energy spectrum of precipitating electrons for the PsA, together with typical frequency-time spectrogram of chorus waves and energy-time diagram of precipitating electrons for the PsA [Miyoshi *et al.*, 2015b].

where ω_{pe} is the electron plasma frequency, I_n is the modified Bessel function of order n, and β_{ce} is defined by

$$\beta_{\text{ce}} = k_{\perp}\rho_{\text{ce}}, \tag{1.18}$$

where $k_{\perp}$ is the wave number perpendicular to the ambient magnetic field, and ρ_{ce} is the electron cyclotron radius. The function $I_n(x)$ can be computed as

$$I_n(x) = \sum_{m=0}^{\infty} \frac{1}{m!(m+|n|)!} \left(\frac{x}{2}\right)^{2m+|n|}. \tag{1.19}$$

Meredith *et al*. [2009] performed a comprehensive survey of ECH waves using the entire 15-month CRRES wave data (see Figure 1.18). Meredith *et al*. [2009] reported that ECH wave intensity increases with increasing geomagnetic activity and is higher in the evening sector (00:00–06:00 MLT). During active periods, strong ECH waves with amplitudes greater than 1 mV/m have been observed within $\pm 3^{\circ}$ centering at the magnetic equator in the range of $L = 4$–7 from 21:00 to 06:00 MLT approximately 20% of the total observation time. The CRRES data coverage is mostly confined within $7R_{\text{E}}$ with pronounced gap in the pre-noon sector for $L > 5$. Using THEMIS wave data, Ni *et al*. [2017] reported that ECH emissions are preferentially a nightside phenomenon primarily confined to the 21:00–06:00 MLT range, and that the most intense ECH waves commonly exist at $L = 5$–9 in the 23:00–03:00 MLT range within 3° centering at the magnetic equator (Figure 1.19). Moderately strong ($\sim$0.1 mV/m) ECH emissions can still be observed up

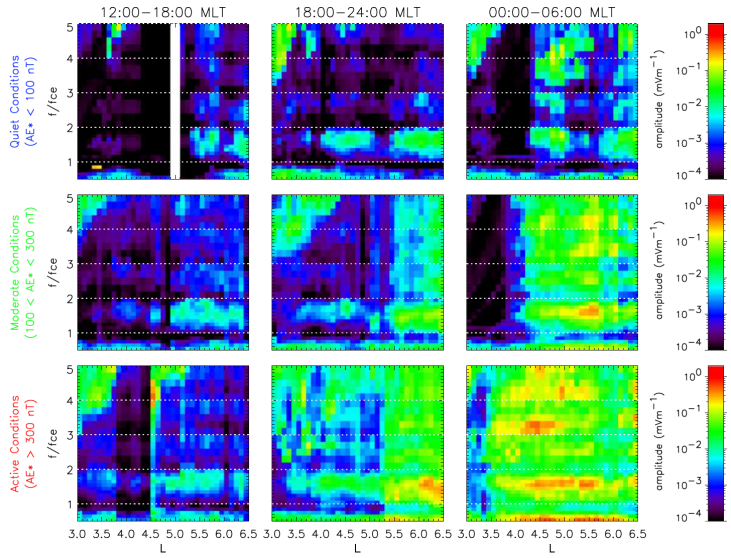

Figure 1.17. Averaged equatorial ($-3^{\circ} < \lambda_{\text{m}} < 3^{\circ}$) wave amplitudes as a function of frequency and L, where λ_{m} is the magnetic latitude. The results are shown for, from left to right, the afternoon (12:00–18:00 MLT), evening (18:00–24:00 MLT), and morning (00:00–06:00 MLT) sectors for, from top to bottom, quiet ($AE^* < 100$ nT), modern ($100 < AE^* < 300$ nT), and active ($AE^* > 300$ nT) conditions. In each panel, the local electron cyclotron frequency and its harmonics are plotted as dashed lines [after Meredith *et al*., 2009].

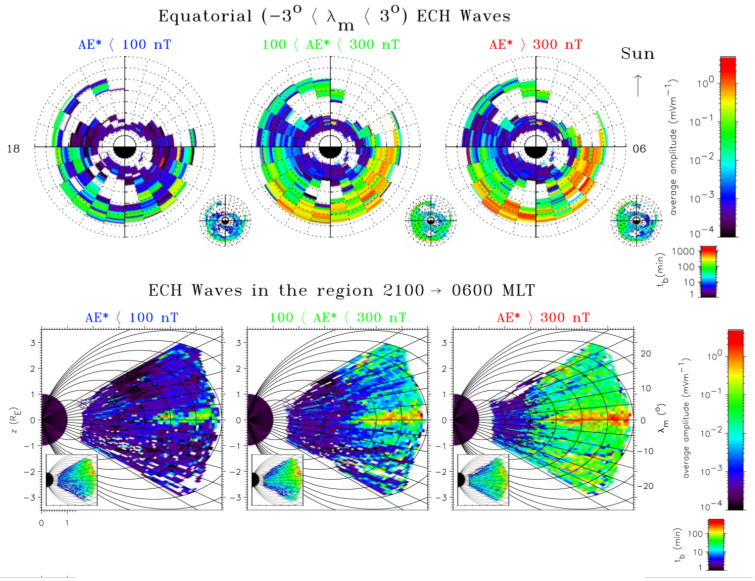

Figure 1.18. (top) Averaged wave electric field amplitudes of ECH waves around the magnetic equator ($-3 < \lambda_m < 3°$), as a function of L and MLT and (bottom) in the sector 21:00–06:00 MLT, as a function of the radial distance from the center of the Earth projected in the SM coordinate system. From left to right, results are presented for quiet ($AE^* < 100$ nT), moderate ($100 < AE^* < 300$ nT), and active ($AE^* > 300$ nT) conditions. Average amplitudes are shown in the large panels, while corresponding sampling distributions are in the small panels [Meredith *et al*., 2009].

to $L \sim 12$ near the pre-midnight sector during geomagnetically active periods.

Predominantly, ECH waves propagate with large wave normal angles to the ambient magnetic field, namely ∼90°: they might propagate $1R_E$ in the azimuthal direction, and reflect about the magnetic equator [Horne *et al*., 2003]. Furthermore, ECH waves are slowly propagating, and the rays grow for a period of up to 50 s during propagation, while chorus waves grow for typically less than 0.5 s [Horne *et al*., 2003]. The excitation of ECH waves has been thought to result from the loss cone instability of ambient, hot electron distribution in the presence of a low-density cold component [Ashour-Abdalla and Kennel, 1978, Horne, 1989, Horne *et al*., 2003]. The occurrence rate of ECH waves with different wave amplitudes under various geomagnetic activities suggests that the triggering of ECH waves does not necessarily require dramatic intensification of geomagnetic activity, thus supporting the idea that a loss cone distribution is the major mechanism for ECH wave generation. However, the disturbed conditions associated with enhanced convection and/or substorm activity can gain ECH wave intensification [Zhang *et al*., 2014]. Since the electron distribution function within the loss cone, and that of cold electron measurements, have been rarely observed so far, it is difficult to establish the theory for ECH excitation mechanism. Despite the difficulty to measure all electron populations and loss cone anisotropy, parametric studies of growth as a function of these variables have been explored [e.g., Horne *et al*., 2003, Ni *et al*., 2012]. For example, Ni *et al*. [2012] reproduced the unstable wave frequencies and wave normal angles which are consistent with observations.

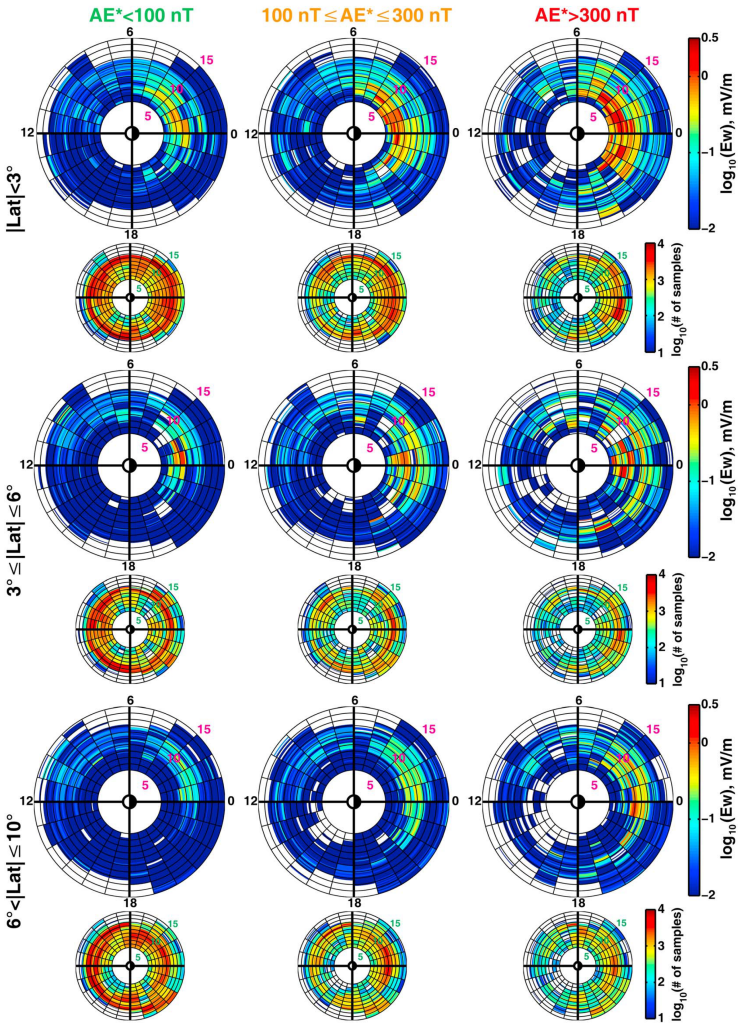

Figure 1.19. Global distributions of the averaged electric field amplitude (E_w) of the first-band ECH waves for the indicated three geomagnetic conditions and three magnetic latitude intervals, based on a survey of the THEMIS data from May 1, 2010 to December 31, 2015. Larger plots show the results of E_w, while smaller plots show the number of total samples in each panel [Ni *et al.*, 2017].

1.6 Wave–Particle Interaction

Trapped particles in the Earth's magnetosphere undergo three types of quasi-periodic motions: gyration around magnetic field lines, bounce motion between the mirror points, and azimuthal drift around the Earth. Each periodic motion is associated with an adiabatic invariant: the first, μ (Eq. 1.1), is associated with a gyromotion of a particle in the guiding center reference frame. If the magnetic field change for a gyro-period is negligible, then μ is conserved. As a fundamental process in the Earth's magnetosphere, wave–particle interactions can generate the growth or damping of waves and particle diffusion, and consequently modify the dynamics of plasma environment. When the wave frequency matches the characteristic frequency of one of the particle's periodic motions, the corresponding adiabatic invariant can be violated, and particle diffusion in the phase space can take place from higher to lower density regions, due to the random exchange of energy between waves and particles. For a charged particle, the full cyclotron resonance condition requires

$$\omega - k_{\parallel} v_{\parallel} = \frac{N\omega_j}{\gamma}, N = 0, \pm 1, \pm 2..., \tag{1.20}$$

where $\omega_j (= qB_0/m_j)$ is the nonrelativistic particle cyclotron frequency for the particle species j of charge q and rest mass m_j, and $\gamma = (1 - v^2/c^2)^{-1/2}$ is the Lorentz factor (c is the speed of light) [Gurnett and Bhattacharjee, 2005]. Eq. 1.20 means that wave–particle resonance occurs when the Doppler-shifted wave frequency experienced by the particle equals an integer multiple of its cyclotron frequency. Landau resonance (N=0) occurs when the particle travels along the ambient magnetic field with the wave parallel speed. For the diffuse and pulsating auroral source population, since their energies are relatively low (a few keV to a few tens of keV), the relativistic effect can be reasonably ignored. In this case Eq. 1.20 is modified as

$$\omega - k_{\parallel} v_{\parallel} = N\omega_j. \tag{1.21}$$

The cyclotron resonant interaction leads to particle diffusions in PA and/or energy, potentially resulting in wave amplification or damping. In the stationary frame of reference, the wave magnetic field for a wave moving in the negative z direction can be written as

$$\mathbf{B} = B[\hat{\mathbf{e}}_x \cos(\omega t + kz) - \hat{\mathbf{e}}_y \sin(\omega t + kz)], \tag{1.22}$$

where $\mathbf{e}_x$ and $\mathbf{e}_y$ are unit vectors in x and y axes, respectively. The position of an electron whose guiding center moves in the positive z direction at velocity v_z can be written as

$$z = v_z t + z_0. \tag{1.23}$$

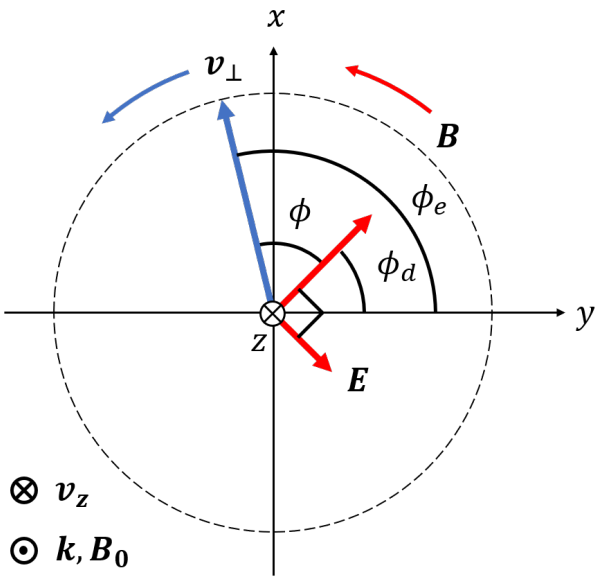

Figure 1.20. The definition of phase angle (ϕ) between the magnetic field ($\mathbf{B}$) of wave and the velocity of electron ($\mathbf{v}_\perp$) perpendicular to the ambient magnetic field ($\mathbf{B_0}$).

The electron therefore experiences the Doppler-shifted waves as

$$\begin{aligned}\mathbf{B} = B[&\hat{\mathbf{e}}_x \cos((\omega + kv_z)t + kz_0) \\ &-\hat{\mathbf{e}}_y \sin((\omega + kv_z)t + kz_0)],\end{aligned} \tag{1.24}$$

where the Doppler-shifted frequency is

$$\omega_\mathrm{d} = \omega + kv_z. \tag{1.25}$$

The electron sees the $\mathbf{E}$ and $\mathbf{B}$ rotate with ω_d, and the phase of $\mathbf{B}$ is (see Figure 1.20)

$$\phi_d = \int \omega_\mathrm{d} dt = \int (\omega + kv_z) dt. \tag{1.26}$$

The perpendicular velocity of electron ($\mathbf{v}_\perp$) gyrates about field line with phase

$$\phi_\mathrm{e} = \int \omega_\mathrm{ce} dt = \omega_\mathrm{ce} t + \phi_0. \tag{1.27}$$

From equations (1.26) and (1.27), the angular difference between $\mathbf{v}_\perp$ and $\mathbf{B}$ is

$$\phi = \phi_\mathrm{e} - \phi_\mathrm{d} = (\omega_\mathrm{ce} - \omega - kv_z)t + \phi_0. \tag{1.28}$$

The electric and magnetic components of wave exert forces on the electron (Figure 1.21)

$$\dot{\mathbf{v}} = -\frac{e}{m}(\mathbf{E} + \mathbf{v} \times \mathbf{B}). \tag{1.29}$$

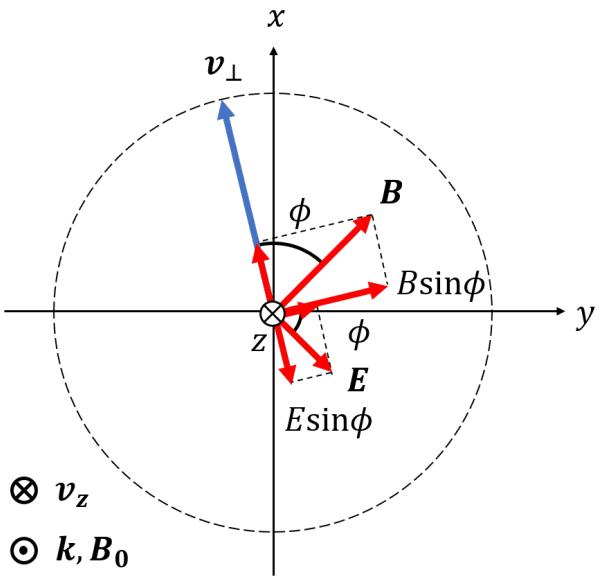

Figure 1.21. The magnetic and electric field, **B** and **E**, which exert forces on the electron.

The components of $\dot{\mathbf{v}}$ perpendicular and parallel to z are

$$\dot{v}_z = -\frac{e}{m} B v_\perp \sin(\phi), \tag{1.30}$$

and

$$\begin{aligned} \dot{v}_\perp &= \frac{e}{m}(E\sin(\phi) + B v_z \sin(\phi)) \\ &= \frac{e}{m} B(v_p + v_z)\sin(\phi), \end{aligned} \tag{1.31}$$

where $v_\mathrm{p} = |E|/|B|$ is the phase velocity. The rate of energy changes is given by

$$\begin{aligned} \frac{d}{dt}\left[\frac{m}{2}(v_z^2 + v_\perp^2)\right] &= m(v_z \dot{v}_z + v_\perp \dot{v}_\perp) \\ &= -v_z e B v_\perp \sin(\phi) + v_\perp e B(v_p + v_z)\sin(\phi) \\ &= e B v_p v_\perp \sin(\phi). \end{aligned} \tag{1.32}$$

Only the term of electric field from Eq. 1.31 contributes to Eq. 1.32. The rate of pith angle changes is given by

$$\dot{\alpha} = \frac{d}{dt}\left[\tan^{-1}\left(\frac{v_\perp}{v_z}\right)\right] = \frac{v_z \dot{v}_\perp - \dot{v}_z v_\perp}{v_z^2 + v_\perp^2} = \frac{e}{m} B\left(1 + \frac{v_p \cos(\alpha)}{v}\right)\sin(\phi). \tag{1.33}$$

In general, ϕ is a rapidly changing function of time given by Eq. 1.28. In this case, $\dot{\alpha}$ displays a rapid sinusoidal variation. On the other hand, if the parallel velocity of a particle, v_z, satisfies the resonant condition of Eq. 1.21, ϕ and $\dot{\alpha}$ are constant from equations (1.28) and (1.33), and appreciable changes in α can accumulate. The sign of $\dot{\alpha}$ and $d(mv^2/2)$ is determined by the phase angle ϕ. The energy and PA of electrons increase in the case of $0 < \phi < \pi(\mathbf{v}_\perp \cdot \mathbf{E} < 0)$ and decrease in the case of $\pi < \phi < 2\pi(\mathbf{v}_\perp \cdot \mathbf{E} > 0)$

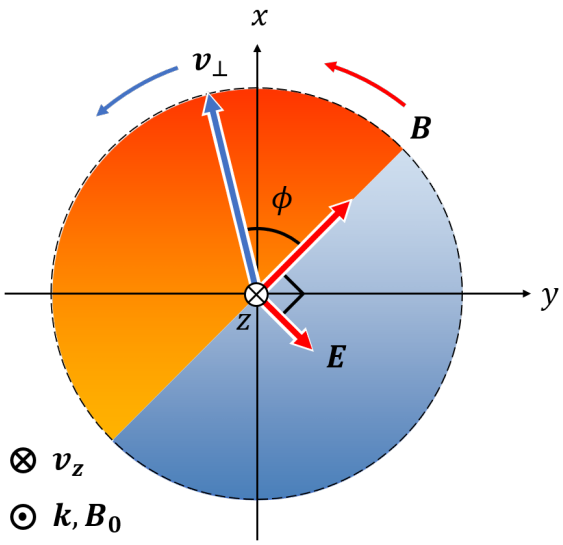

Figure 1.22. Region where the electron gains energy (red region) and where it loses energy (blue region).

(see Figure 1.22). A single frequency wave of infinite duration will impart net deflections only for particles in exact resonance frequency. Waves even slightly off-resonance will successively increase and decrease α as the phase angle ϕ rotates through 2π. If, however, the wave is of finite duration, off-resonance can change α permanently during the duration of wave. If the duration of wave with width ($\Delta\omega$) is long, the phase angle ϕ is likely to shift from acceleration (deceleration) phase into deceleration (acceleration) phase. The wave band width $\Delta\omega$ for a wave of duration Δt is obtained as follows [Gurnett and Bhattacharjee, 2005]. If the change in ϕ is limited to π in Δt:

$$\Delta\phi = (\omega_{\text{ce}} - \omega - kv_z)\Delta t = \pi. \tag{1.34}$$

Consider the first factor on the right as a function ω, and expand it in a Taylor series about the resonant frequency $\omega = \omega_{\text{ce}} - kv_z$:

$$\begin{aligned} \Delta\phi &= (\Delta\phi)_{\omega=\omega_{\text{ce}}-kv_z} + \frac{\partial}{\partial\omega}(\Delta\phi)\cdot\Delta\omega + \ldots = \pi \\ &\sim -\left(1+\frac{v_z}{v_g}\right)\Delta\omega\Delta t = \pi, \end{aligned} \tag{1.35}$$

and

$$|\Delta t| \approx \frac{\pi}{(1+v_z/v_{\text{g}})\,\Delta\omega}, \tag{1.36}$$

where v_g is the wave group velocity. The diffusion coefficient, $D_{\alpha\alpha}$, can be estimated for a series of waves of duration Δt interacting with particle. With denoting change per unit time:

$$\begin{aligned} D_{\alpha\alpha} = \frac{\langle(\Delta\alpha)^2\rangle}{2} &\approx \frac{1}{2}\left\langle\left(\frac{d\alpha}{dt}\right)^2(\Delta t)^2\right\rangle \\ &\approx \frac{1}{2}\left(\frac{e}{m}\right)^2\frac{B^2}{\Delta\omega}\left(1+\frac{v_p\cos(\alpha)}{v}\right)^2(\sin^2(\phi))_{ave}\frac{\pi}{(1+v_z/v_g)} \\ &\approx \frac{\pi}{4}\left(\frac{e}{m}\right)^2\frac{B^2}{\Delta\omega}\left(1+\frac{v_p\cos(\alpha)}{v}\right)^2\frac{1}{1+v_z/v_g}, \end{aligned} \tag{1.37}$$

since $(\sin^2(\phi))_{ave} = 1/2$ for particles uniformly distributed in ϕ_0. The factor $B^2/\Delta\omega$ is interpreted as the power spectral density of waves at the resonant frequency. In situations where $v_p \ll v$ and $v_g \ll v_z$, $D_{\alpha\alpha}$ can be approximated as

$$D_{\alpha\alpha} \approx \frac{\pi}{4}\left(\frac{e}{m}\right)^2\left(\frac{B^2}{\Delta\omega}\right)\frac{v_g}{v_z}. \tag{1.38}$$

Other approximations give slightly different results [e.g., Glauert and Horne, 2005, Su *et al*., 2009]. Pitch-angle diffusion coefficients for ECH, UBC, and LBC waves are summarized in Figure 1.23: they were calculated using the Full Diffusion Code [Shprits and Ni, 2009], which was developed at the University of California, Los Angeles (UCLA), on the basis of the field-aligned code [Shprits *et al*., 2006], and is capable of computing resonance scattering rate including high-order scattering by obliquely propagating waves, and a wave model. ECH waves can resonate with electrons in the energy range from a few hundred eV to a few keV for PAs below about 20°. In contrast, UBC waves can resonate with electrons ranging from tens of eV to a few keV, while LBC waves can resonate with electrons from a few keV to a few hundred of keV for a wide PA range. Tao *et al*. [2011] suggested that the formation of the electron PA distribution observed by THEMIS spacecraft at $L = 6$ is mainly due to resonant interactions with a combination of UBC and LBC waves. Khazanov *et al*. [2015a] showed that the majority of both upward and downward particle and energy flux contribution comes from LBC waves, which contribute between 45–50% of the flux, while UBC waves contribute for the $\sim$35%, and ECH waves for 10–20% at $L = 6.8$.

1.7 Review of Previous Observation and Theory for the Generation of PsAs

In recent decades, observations and theories on chorus waves have been developed, and the relationship between these waves and PsAs has been revealed. Nishimura *et al*. [2010, 2011] demonstrated that temporal variations of LBC wave intensity observed by THEMIS satellites near the magnetic equator had one-to-one correlations with main modulations of PsA emission intensity observed by the all-sky images at THEMIS ground-based observations (GBOs) [Mende *et al*., 2008]. Miyoshi *et al*. [2015b] demonstrated that the

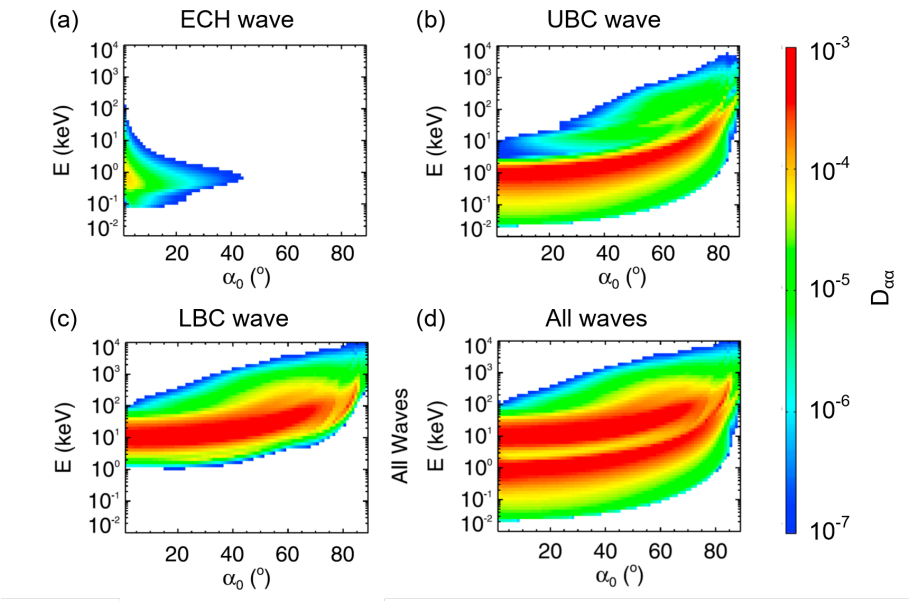

Figure 1.23. Pitch-angle diffusion coefficients of (a) ECH, (b) UBC, (c) LBC, and (d) all waves [after Tao *et al*., 2011].

main and internal modulations of PsAs are caused by LBC bursts and rising tone elements, respectively, and that the stable precipitation at about 1 keV is caused by UBC waves thanks to a computer simulation. Kasahara *et al*. [2018a] showed one-to-one correlations between the loss cone electron flux and LBC wave intensity, using the data obtained with Onboard Frequency Analyzer (OFA) [Matsuda *et al*., 2018], and medium-energy particle experiments–electron analyzer (MEPe) [Kasahara *et al*., 2018b] onboard the Arase satellite: this implies that wave–particle interactions are indeed taking place between LBC waves and electrons. Hosokawa *et al*. [2020] identified an excellent one-to-one correlation between chorus elements and internal PsA modulations by coordinating experiments using high-resolution all-sky imagers (with 100-Hz sampling) with the Arase satellite (Figure 1.24). It was suggested that relativistic electron precipitation by LBC waves could yield significant production of odd hydrogen and nitrogen, followed by catalytic reactions that destroy ozone [Miyoshi *et al*., 2021, Tesema *et al*., 2020a, Thorne, 1977, Turunen *et al*., 2016]. Using Van Allen Probes, Ma *et al*. [2020] found that the most significant electron precipitation due to chorus waves was from the nightside to dawn sectors over $4 < L < 6.5$. Although Van Allen Probes usually cannot resolve the flux inside loss cone, Ma *et al*. [2020] calculated the loss cone filling ratio based on the wave measurements and quasilinear theory.

In addition to the chorus waves, ECH waves are theoretically expected to fill a loss cone, called strong diffusion, in the energy range from a few hundred eV to a few keV, as described in Section 1.5. Liang *et al*. [2010] showed that mean peak-to-peak intervals of a PsA ($\sim$13.3 s) and ECH wave intensity ($\sim$10.2 s) were similar, through the analysis of data taken by the Fort Smith all-sky imager and the THEMIS satellite. However, correlation between them was not high, probably because of the nonideal conjugacy between the ground and the satellite. Furthermore, it was reported that the auroral red emission at 630 nm were

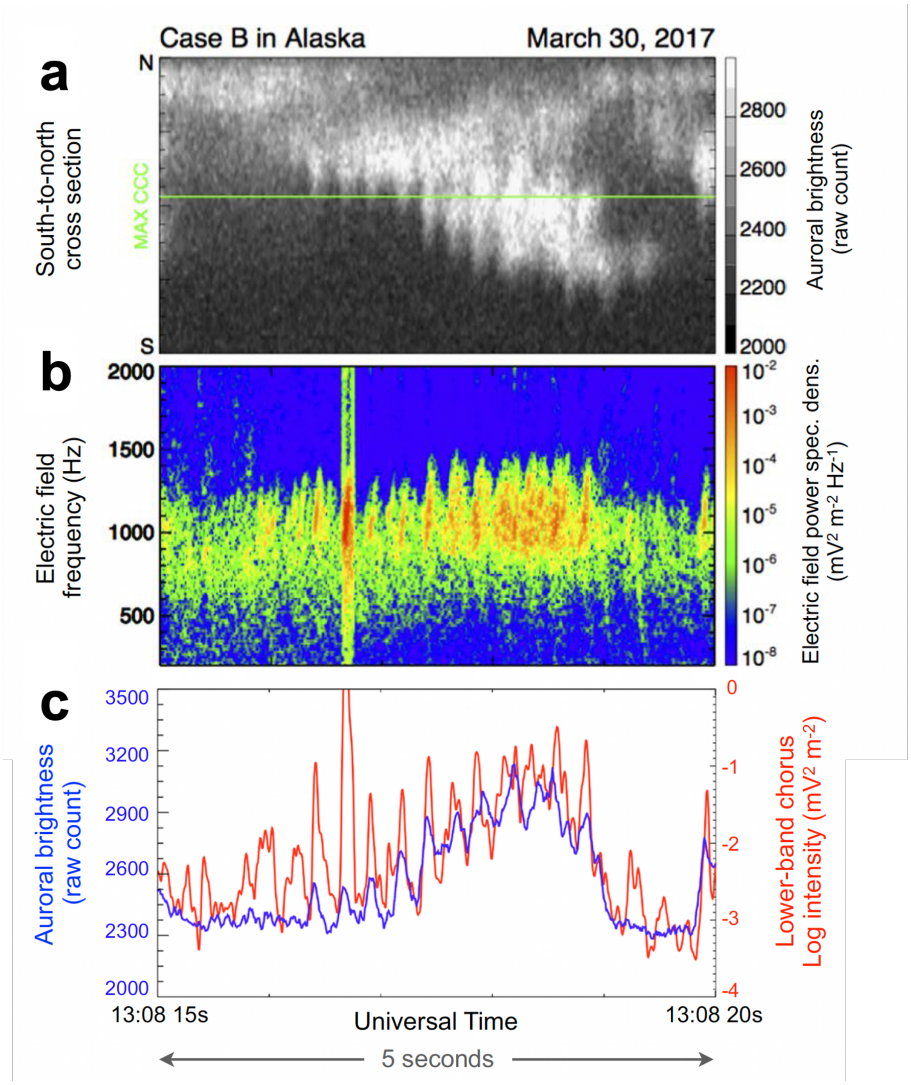

Figure 1.24. A direct comparison between internal PsA modulations and chorus elements [after Hosokawa *et al.*, 2020]. (a, b) A zoomed view of (a) the single chorus burst structure, and (b) the corresponding PsA pulse. (c) A zoomed view of optical and wave data. The blue line represents the auroral luminosity time series, while the red line denotes the integrated wave power over the LBC frequency range.

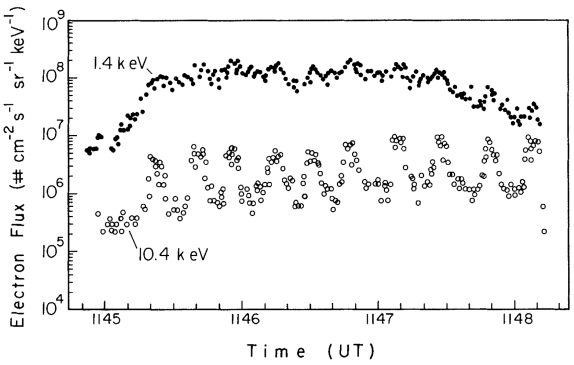

Figure 1.25. Time variations in electron fluxes at PAs below 90° during a flight into auroral pulsations [McEwen *et al.*, 1981].

modulated by pulsating electron precipitation, with a typical period of approximately 10 s, in spite of the long emission time constant ($\sim$110 s) [Eather, 1969, Liang *et al.*, 2016]. McEwen *et al.* [1981] showed that the electron flux had main modulations at 10.4 keV and minor variations at 1.4 keV during a rocket flight into a PsA (Figure 1.25). Liang *et al.* [2016] suggests that low-energy electrons ($<$1 keV) are scattered by ECH or UBC waves as a candidate mechanism of red-line PsAs. It should be noted that Tsuda *et al.* [2020] performed observations of PsAs with an optical spectrograph, and found that pulsations seen in 630 nm data were due to the contamination of the N_2 1PG (10,7) 632.3-nm band. Tsuda *et al.* [2020] suggested that the OI 844.6 nm would be a most probable candidate for investigating PsA in the *F* region caused by low-energy electrons, since they were relatively less contaminated by other emissions.

Low-energy electron precipitation in PsAs is important for ion upflows, which provide heavy ions into the magnetosphere. Liang *et al.* [2018] reported that low-energy electron precipitation produced a strong enhancement of electron temperatures and ion upflows in the upper *F* region ionosphere, associated with PsAs from the Poker Flat Incoherent Scatter Radar (PFISR) observation data and simulations. More in detail, the authors suggested that the electron temperature enhancement in the upper *F* region may increase the electron scale height, hereby giving rise to an ambipolar electric field that drives ion upflows. Thus, a better understanding of ECH waves as drivers of precipitating low-energy electrons is important not only for PsA emissions, but also for ion upflows, since this can affect magnetospheric dynamics. Furthermore, density modulation of low-energy ($\sim$100 eV) ions correlated with chorus wave intensity modulation was observed by the THEMIS satellite [Nishimura *et al.*, 2015]: these low-energy ions are field-aligned with major peaks at 0° (for northern hemisphere winter event) and 180° (for northern hemisphere summer event), indicating that the source of low-energy plasma density modulation observed near the magnetic equator is outflowing plasma from the sunlit hemisphere (Figure 1.26).

PsAs are often overlapped with a background diffuse aurora, probably caused by soft electrons [McEwen *et al.*, 1981, Sandahl *et al.*, 1980, Smith *et al.*, 1980]. Evans *et al.* [1987] suggested that these electrons originate from the opposite hemisphere in conjunction with simultaneously occurring PsAs: they showed

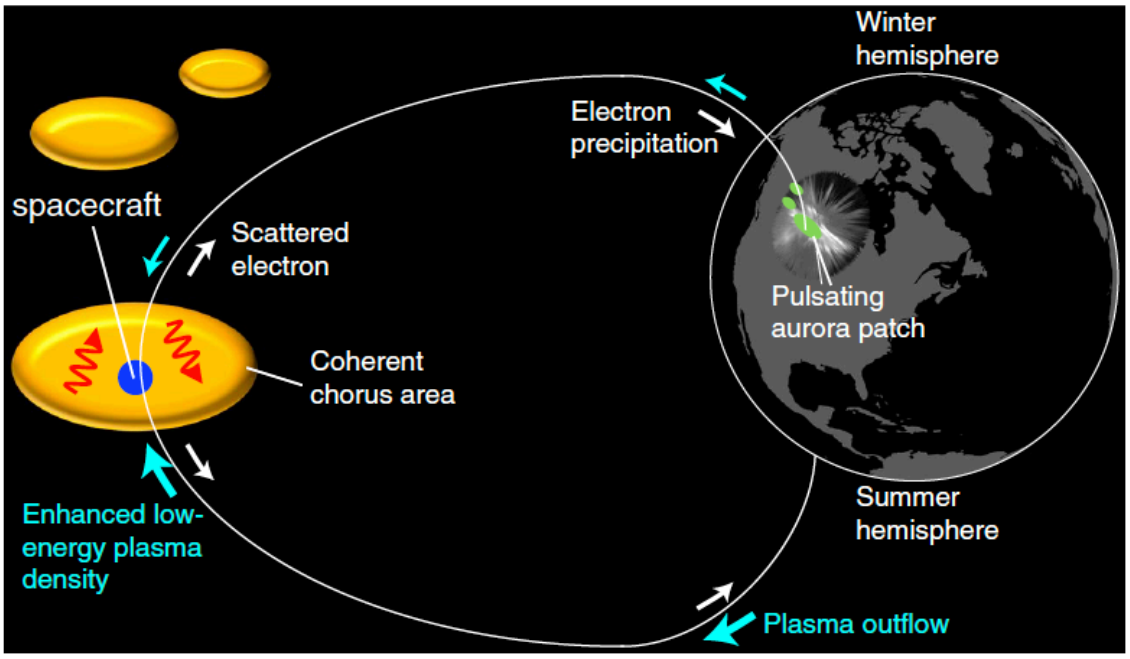

Figure 1.26. Schematic illustration of the chorus intensity modulation mechanism proposed by Nishimura *et al*. [2015].

that this population arises from secondary and backscattered electrons, produced by the primary high energy pulsating electrons. Moreover, the e-POP satellite observed upgoing low-energy electrons over PsAs, which are considered to be backscattered and secondary electrons [Knudsen *et al*., 2015]. Soft electron precipitation by UBC and ECH waves also causes background diffuse auroras [Miyoshi *et al*., 2015b]; however, their contributions in causing background diffuse auroras are still not fully understood.

Recent high-time resolution ground-based optical observations of PsAs revealed that the brightness of PsAs sometimes decreases below the diffuse background level (Figure 1.27) [Dahlgren *et al*., 2017, Hosokawa *et al*., 2021, Kataoka *et al*., 2012]. Such "over-darkening PsA" happens both immediately before and after the pulsation ON phase [Dahlgren *et al*., 2017]. Hosokawa *et al*. [2021] demonstrated that

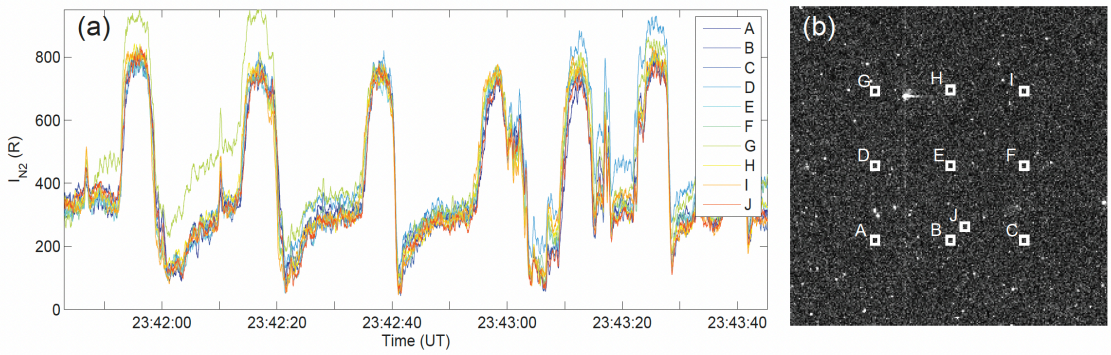

Figure 1.27. (a) N_2 emission brightness in 10 different locations across the field of view of the multispectral instrument ASK (Auroral Structure and Kinetics). Locations where brightness has been measured are shown in (b) [Dahlgren *et al*., 2017].

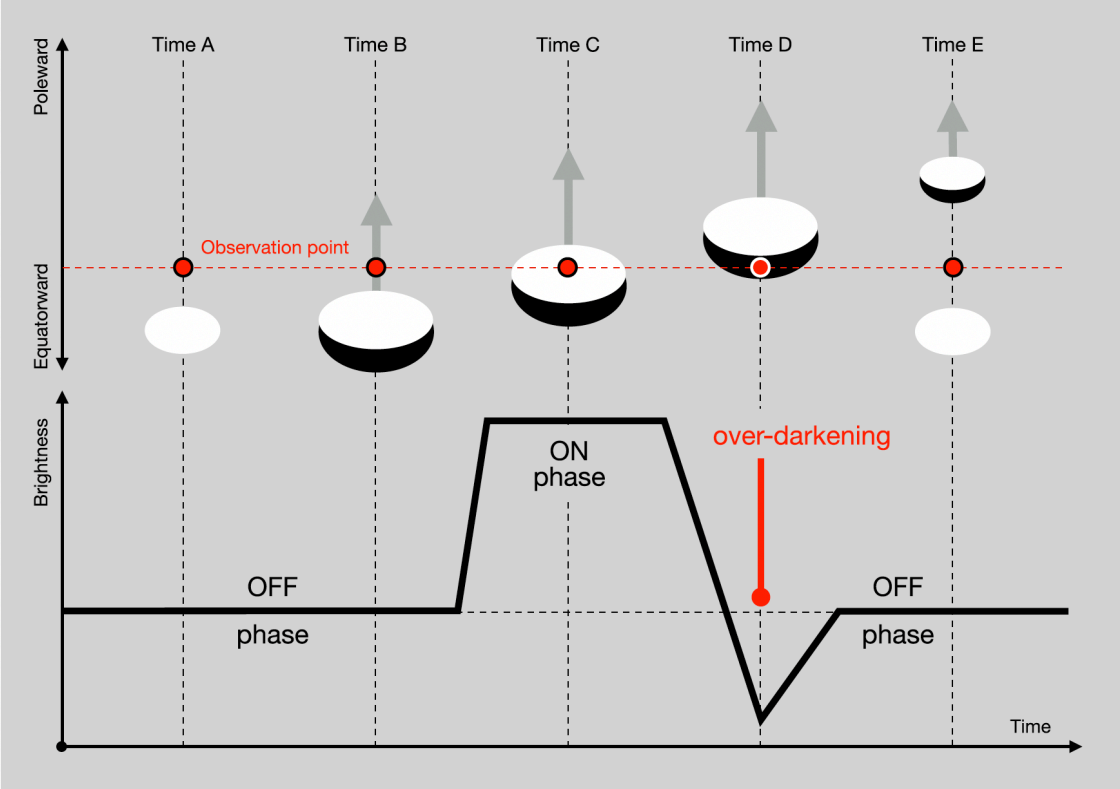

Figure 1.28. Schematic illustration of the over-darkening PsA created by the poleward propagation of a PsA patch accompanied by a dark region along its trailing edge [Hosokawa *et al*., 2021].

the over-darkening region already appeared on the trailing edge of the patch at the start of the ON phase, while the dark region propagated poleward together with the main part of the patch (Figure 1.28). That is, the over-darkening PsA is a result of compounding effects of spatial structure and dynamical motion of PsA patches. Although the mechanism that creates the dark area is still unknown, past studies suggested that an interplay of UBC and LBC might explain the process [Miyoshi *et al*., 2015b]; furthermore, other authors suggested that charge polarization along the boundary of PsA patches [Hosokawa *et al*., 2010] might provide an alternative explanation for the dark area along the trailing edge of patches. To explain the spatial and temporal variations of PsAs, it is essential to consider several factors, such as contributions of multiple waves, and dynamical propagation of the wave source region, and to examine the three-dimensional structure of PsAs and plasma parameters in the ionosphere.

1.8 Purpose of This Thesis

Concerning the relationship among ECH waves, electron precipitation, and PsAs, Fukizawa *et al*. [2018] reported that the ECH wave intensity observed by the Arase satellite showed a correlation with the PsA intensity observed by an all-sky imager near the Arase's ionospheric footprint; they suggested that the PsA, correlated with ECH waves, might be caused by about 3–4-keV electrons using a time-of-flight analysis.

Furthermore, it was theoretically suggested that ECH waves contribute to ∼10–20% of the total electron energy precipitation flux due to ECH, LBC, and UBC waves [Khazanov *et al*., 2015a, Tao *et al*., 2011, Thorne, 2010, Tripathi *et al*., 2013]. Kasahara *et al*. [2019] reported that the strong diffusion of high energy electrons (10–100 keV) by LBC waves commonly occurs using *in situ* observation data obtained using medium-energy particle experiments-electron analyzer [Kasahara *et al*., 2018b] onboard the Arase satellite.

However, there is no observational evidence that ECH waves actually scatter electrons into the loss cone. In addition, the PA scattering efficiencies of low-energy electrons (0.1–10 keV) by each wave have not been investigated via *in situ* observations, due to the measurement difficulty of electron fluxes inside loss cones in the magnetosphere. Although a loss cone is usually too small to be resolved in conventional electron sensor on a magnetospheric satellite, the advent of the Arase satellite enabled direct evaluation of loss cone electron fluxes, with the advantage of the relatively high angular resolution of low energy and energetic electron instruments [Miyoshi *et al*., 2018d].

The purpose of this thesis is to elucidate the generation mechanism of low-energy electron precipitation in PsAs through the Arase satellite, ground-based optical and radar observations, and computed tomography. Instruments and research targets of this thesis are schematically shown in Figure 1.29. In Chapter 2, in order to verify whether ECH waves scatter electrons into a loss cone, we compared ECH wave intensity with electron flux inside the loss cone obtained with low-energy particle experiments-electron analyzer (LEPe) onboard the Arase satellite. In Chapter 3, in order to obtain a statistical view for strong electron scattering by LBC, UBC, and ECH waves, we analyzed the wave and electron data obtained by the Arase satellite

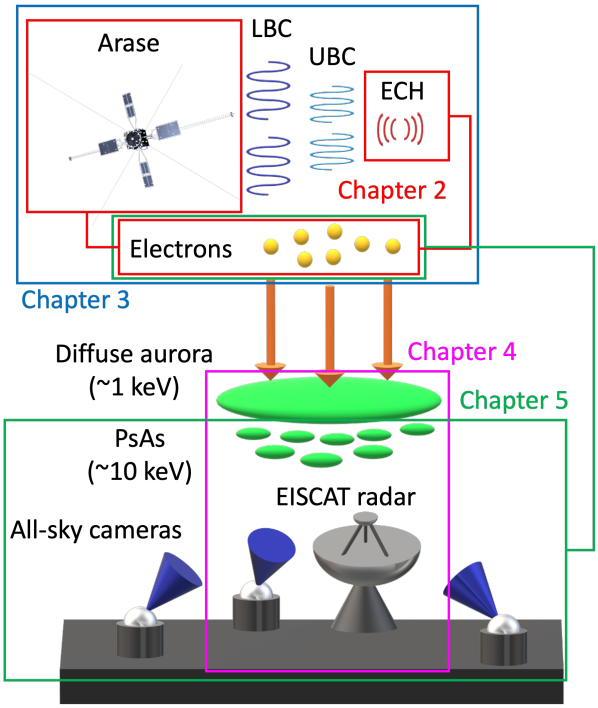

Figure 1.29. Schematic illustration of instruments and research subjects of this thesis: those used in each chapter are enclosed in their respective rectangles.

from March 24, 2017 to August 31, 2020. In Chapter 4, using the data obtained by the European incoherent scatter (EISCAT) radar and all-sky imager at Tromsø, we conducted statistical studies for 14 events to clarify how often F region electron density enhancement caused by low-energy electron precipitation occurs as associated with PsAs. In Chapter 5, we aim to investigate the energy and spatial distribution of precipitating electrons in PsAs with Aurora Computed Tomography (ACT). Finally, results are discussed in Chapter 6, and summarized in Chapter 7.

2 Pitch-Angle Scattering of Low-Energy Electrons by ECH Waves [Fukizawa *et al*., 2020]

In this chapter, we demonstrate that the ECH wave intensity near the magnetic equator is correlated with an electron flux inside a loss cone with energy of about 5 keV using simultaneous wave and particle data obtained by the Arase satellite, which is equipped with a high-PA resolution electron analyzer. Results from computer simulation suggest that this electron flux contributes to the auroral emission at 557.7 nm, and an intensity of about 200 R.

2.1 Background

The typical cyclotron resonance energies of ECH and LBC waves range from a few hundred to a few keV, and from a few keV to a few MeV, respectively [e.g., Gao *et al*., 2016, Horne *et al*., 2003, Kurita *et al*., 2014, Miyoshi *et al*., 2015a, Ni *et al*., 2008]. In order to determine which plasma waves contribute to electrons scattering into the loss cone, it is essential to compare their intensity with the electron flux inside the loss cone through in-situ observations. Kasahara *et al*. [2018a] demonstrated an one-to-one correspondence between the LBC wave intensity and a 24.5 keV electron flux in the loss cone, by using data from the Arase satellite. However, there are no observations regarding ECH waves scattering electrons into the loss cone. In the outer magnetosphere, where the interaction with ECH waves leads to electron precipitation and diffuse auroral emissions, the loss-cone angle near the equatorial plane is too small compared to the inner magnetosphere: therefore, a spacecraft cannot measure the electron flux in the loss cone. In this chapter, we investigate whether ECH waves scatter electrons into the loss cone in the equatorial region of the inner magnetosphere, by comparing electron fluxes in the loss cone with wave amplitudes, and calculating pitch-angle diffusion coefficients.

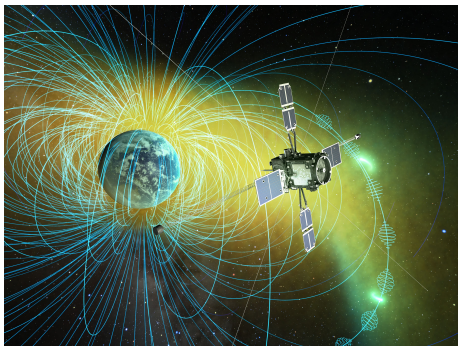

Figure 2.1. Image of ERG satellite observations in the geospace [Miyoshi *et al.*, 2018d].

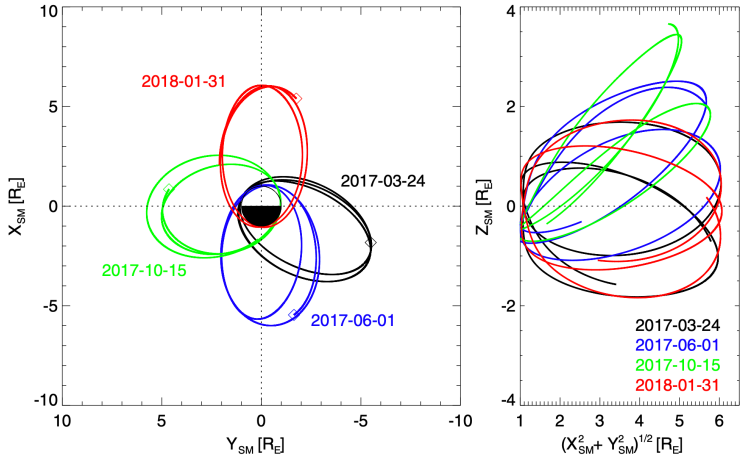

Figure 2.2. Sample orbits of the ERG satellite. Black: March 24, 2017, Blue: June 1, 2017, Green: October 15, 2017, and Red: January 31, 2018 [Miyoshi *et al.*, 2018d].

2.2 Instrumentation

2.2.1 Arase Satellite

The Exploration of energization and Radiation in Geospace (ERG, also called Arase) satellite (Figure 2.1) was successfully launched on December 20, 2016 [Miyoshi *et al.*, 2018d]: it is designed to be Sun-oriented and spin-stabilized, with a rotation rate of 7.5 rpm. The initial apogee and perigee altitudes are $\sim$32000 and $\sim$400 km, respectively, in order to explore the entire region of the radiation belts. The inclination angle of the satellite orbit is $\sim 31^\circ$. Figure 2.2 shows the orbit of the Arase satellite in four different seasons in the equatorial and meridional planes. Since the critical and commissioning phases of operation took three months, regular observations with full operation of all instruments started in late March, 2017. Immediately after that, the Arase satellite observed the inner magnetosphere near the magnetic equator at the heart of the outer radiation belt ($L = 4$–6) on the morning side (black curves in Figure 2.2).

Figure 2.3 shows a schematic illustration of nine instruments installed on the Arase satellite. Figure 2.4 shows the energy and frequency coverages of these instruments. LEPe [Kazama *et al.*, 2017] measures 19 eV–20 keV electrons in the plasma sheet and ring current. The plasma wave experiment (PWE) observes

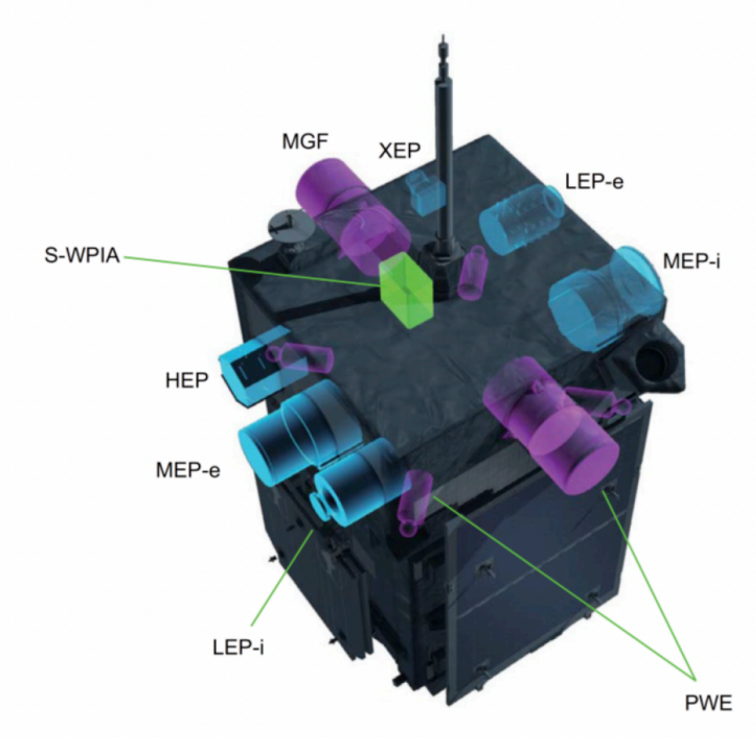

Figure 2.3. Configuration of science instruments onboard the Arase satellite [Miyoshi *et al*., 2018d].

electric fields in the frequency range from DC to 10 MHz, and magnetic fields in the frequency range from a few Hz to 100 kHz [Kasahara *et al*., 2018c]. The frequency range of chorus and ECH waves is covered by OFA [Matsuda *et al*., 2018]. High-frequency analyzer (HFA) [Kumamoto *et al*., 2018] covers the higher frequency range, including upper hybrid resonance (UHR) waves. Magnetic field experiments (MGF) [Matsuoka *et al*., 2018b] observes the ambient magnetic field.

2.2.2 Onboard Frequency Analyzer

The OFA is one of the PWE receivers, onboard the Arase satellite. It is designed to entirely measure extremely low (ELF) and very low frequencies (VLF) plasma waves' activity, and obtain several properties (power spectrum, propagation direction, and polarization) for the wave mode determination. The important targets of the OFA measurement are chorus and magnetosonic waves, which have been suggested to drive the acceleration of relativistic electrons in the radiation belts and electromagnetic ion cyclotron (EMIC) waves, responsible for the scattering of relativistic electrons by anomalous cyclotron resonance. OFA processes signals from several dipole wire-probe antennas (WPT-S) [Kasaba *et al*., 2017] and tri-axis magnetic search coils (MSC) [Ozaki *et al*., 2018]. The geometric configuration of the sensors is shown in Figures 2.5 and 2.6. The OFA analyzes two components of electric (E_{u} and E_{v}) and three of magnetic fields (B_{α}, B_{β}, and B_{γ}); it performs fast Fourier transform (FFT) on the observed waveforms, and produces a single-channel power spectrum (OFA-SPEC), spectral matrices (OFA-MATRIX), and full-channel complex

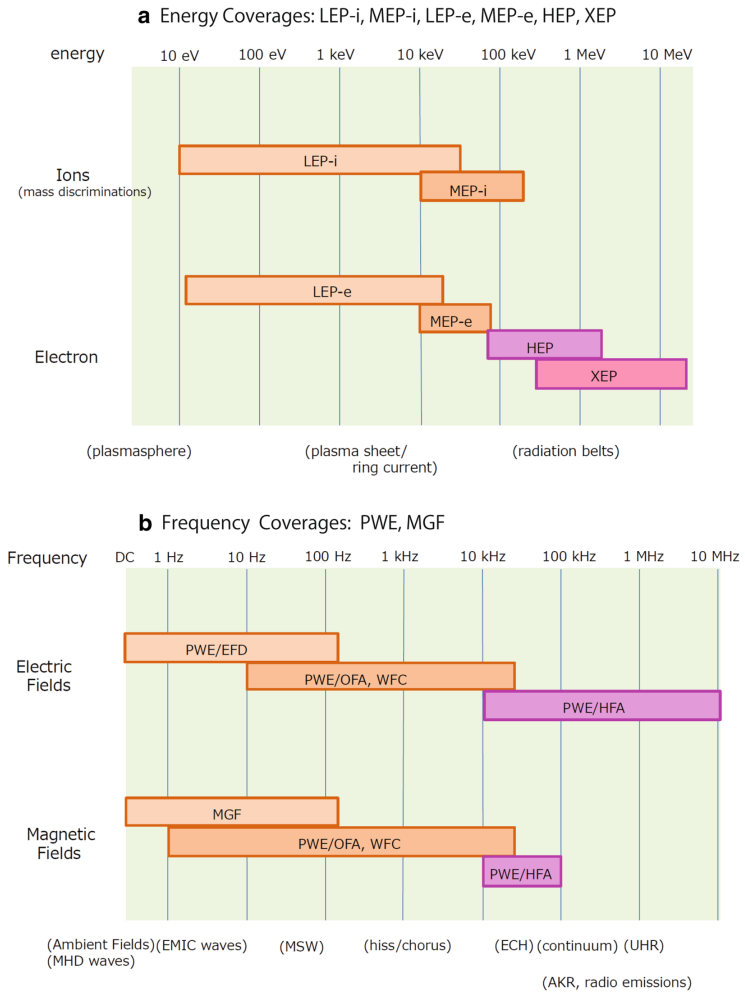

Figure 2.4. (a) Energy coverage of electron measurements from LEPe, MEPe, HEP, and XEP, and ion measurements from LEPi, and MEPi. (b) Frequency coverage of electric and magnetic field measurements from PWE (EFD, OFA/WFC, and HFA) and MGF [Miyoshi *et al*., 2018d].

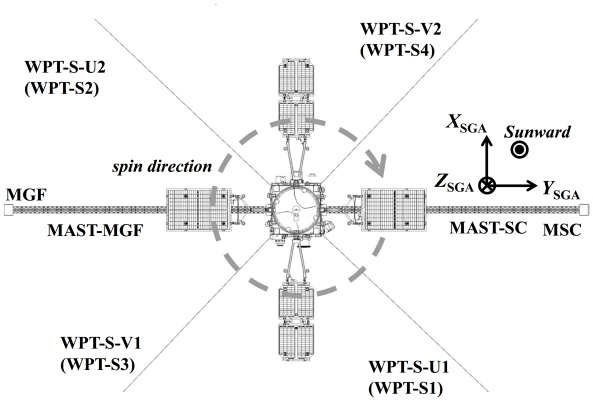

Figure 2.5. Overview of the Arase satellite from the Z_{SGA} direction, where "SGA" stands for "Spinning Satellite Geometry Axis" coordinates, which represent the geometrical positions of the components onboard the satellite [Kasahara *et al*., 2018c].

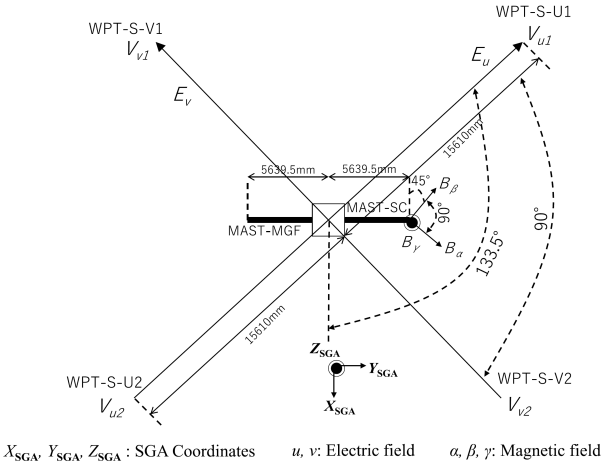

Figure 2.6. Configuration of PWE sensors deployed from the Arase satellite [Kasahara *et al*., 2018c].

spectra for electric and magnetic fields (OFA-COMPLEX). In this study, we used OFA-SPEC data, which are the auto-spectra of a selected channel for electric and magnetic fields produced by onboard processing. The frequency range of electric field spectra is from DC to 20 or 130 kHz, while that of magnetic field spectra is from a few Hz to 7 or 20 kHz. The number of frequency sampling points depends on the OFA operation mode . The time resolution of OFA-SPEC is nominally 1 s, whereas the possible time resolution ranges from 0.5 to 4 s. During the time interval of our interest, the OFA performs FFT on the waveform of 16 ms, with a time cadence of 1 s, and provided 132-point frequency spectra.

2.2.3 Low-Energy Particle Experiment–Electron Analyzer

LEPe measures electrons with energies ranging from ∼20 eV to ∼20 keV [Kazama *et al*., 2017]. In order to obtain the PA distribution, LEPe measures three-dimensional electron fluxes every spin period (∼8 s). There are two different types of channels: coarse, for observing the electron's parallel and perpendicular temperature and PA distributions, with a resolution of 22.5°, and fine channels for loss-cone measurements, with a PA resolution of 3.75° (Figure 2.7). In this study, we use data obtained from the latter.

2.3 Data and Method

We analyzed data obtained by the Arase satellite from 01:10 to 01:15 UT on April 15, 2017, which corresponds to the substorm recovery phase. A southward interplanetary magnetic field with a ∼400-km/s solar wind speed caused the substorm on April 14–15, 2017 (Figure 2.8). The minimum value of the Dst index was -25 nT at 18:30 UT on April 14, 2017, while the maximum value of the AE index was 931 nT at 18:35 UT on April 14, 2017. The Arase satellite is in the postmidnight sector near the magnetic equator ($L_{\rm m} = 6.1$ derived from IGRF, MLT $= 3.2$ h, and magnetic latitude (MLAT) $= 0.0°$–$0.4°$). Figures 2.9a and 2.9b show the wave power-spectral density of the electric and magnetic fields, respectively. Frequency

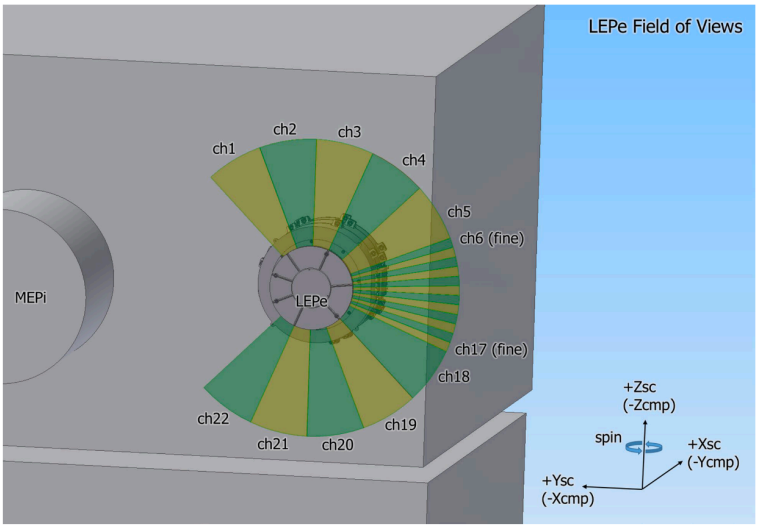

Figure 2.7. Schematic drawing of the accommodation and field of view (FOV) of the LEPe instrument. Here, the suffix 'sc' stands for spacecraft coordinate system, while 'cmp' stands for component (instrument) coordinate system. This is installed on the $-$X panel of the spacecraft; the fan-shaped FOV opens parallel to the panel [Kazama *et al.*, 2017].

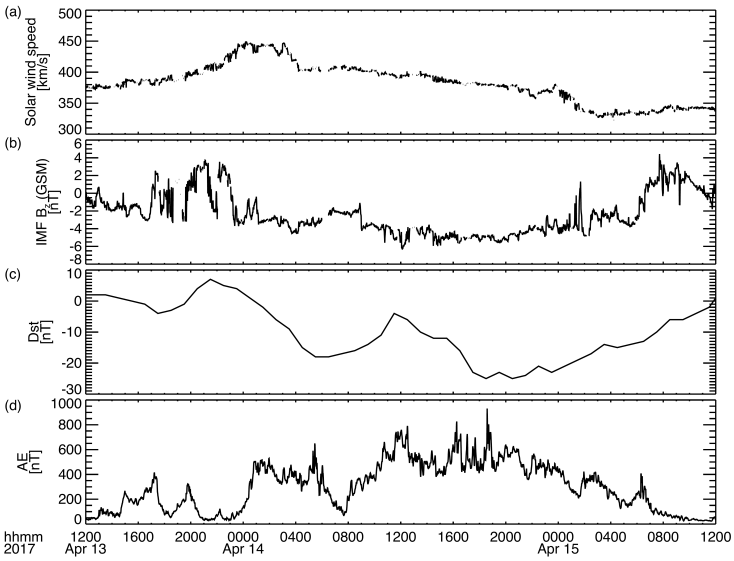

Figure 2.8. (a) Solar wind speed, (b) interplanetary magnetic field in a north–south direction (B_z) in the geocentric solar magnetospheric (GSM) coordinate, (c) Dst index, and (d) AE index from 12:00 UT on April 13, 2017 to 12:00 UT on April 15, 2017.

has been normalized by f_{ce}. We derived f_{ce} from the local ambient magnetic field measured by MGF. Furthermore, quasi-periodic intense ECH emissions were observed in the first harmonic band (f_{ce}–$2f_{ce}$), while the amplitudes of the higher harmonic bands were small (Figure 2.9a). Upper- ($> 0.5f_{ce}$) and lower-band ($< 0.5f_{ce}$) chorus waves were observed throughout this period; upper-band chorus waves appeared rather continuously (Figure 2.9b). Figures 2.9c and 2.9d show the electron energy flux in the field-aligned direction (with a PA range of 0–$3°$) and outside a loss cone (with a PA range of 42–$45°$), respectively. Although the electron flux outside the loss cone was relatively stable, the field-aligned electron flux had quasi-periodic modulations, with a typical period of $\sim$26 s indicated by red dashed lines in Figure 2.9c. To visualize the differences between the electron flux inside and outside the loss cone, we show the ratio of electron fluxes (Figure 2.9e). It is difficult for Arase satellite to continuously and for a long time observe an electron flux of specific energy in the loss cone, since its direction relative to the ambient magnetic field changes. Therefore, the analyzed data was limited to 5 min, as shown in Figure 2.9. To investigate quantitatively the relationship between the waves and the electron flux inside the loss cone, we calculate the cross-correlation coefficients between the temporal modulation of the wave intensity shown in Figures 2.9a and 2.9b and the electron flux ratio shown in Figure 2.9e. The ECH (LBC) wave intensity is derived by integrating the wave power-spectral density of the electric (magnetic) field between f_{ce} and $2f_{ce}$ ($0.3f_{ce}$ and $0.5f_{ce}$) shown in Figure 2.9a (2.9b), and then converting it to mV/m (nT). Before calculating the cross-correlation coefficients, we need to adjust the temporal resolution of the wave data (1 s) to that of the electron data (8 s). We calculated the moving average of the wave data with a 9-s window and subtracted the average. To avoid aliasing in the downsampling, we applied a low-pass filter with a cutoff frequency of 1/16 Hz. We used the Hanning window to perform a FFT before applying the low-pass filter.

2.4 Results

Figures 2.10a and 2.10b show the temporal variability of ECH and LBC wave intensities, respectively. The loss-cone flux ratio of the 4.8-keV electron is indicated by blue lines in Figures 2.10a and 2.10b. The average flux ratio was subtracted, and the Hanning window was applied: the cross-correlation coefficients correspond to 0.48 for ECH and -0.016 for LBC. Although the absolute value of the cross-correlation coefficient is not very high in the case of ECH, it is still large compared to the value considering LBC, and is statistically significant, as indicated by the obtained Student's t-test values. The estimated p value for ECH is $< 3.5 \times 10^{-3}$ which is smaller than the significance level of 5.0×10^{-2}, whereas it is < 1.0 for LBC. One of the causes of the reduction of the cross-correlation coefficient in the ECH case is that the loss-cone angle at the position of the Arase satellite is not always larger than the PA resolution of the fine LEPe channels. If we assume that the magnetic field strength in the ionosphere at the Arase's magnetic footprint is $50,000$ nT estimated with the TS04 model [Tsyganenko and Sitnov, 2005], the loss-cone angle at the Arase satellite is $2.4°$ since the magnetic field strength at the Arase satellite is 88 nT. Figure 2.10c shows

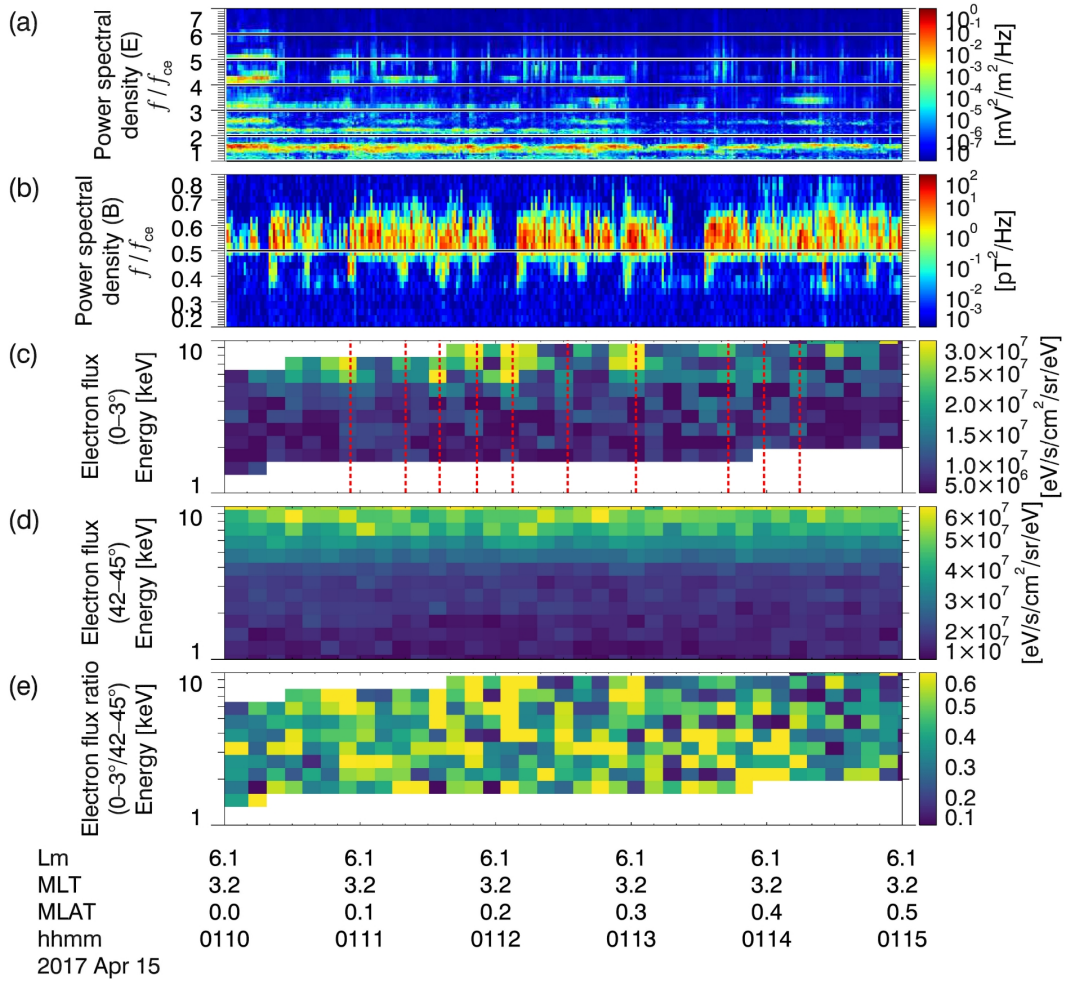

Figure 2.9. The wave power-spectral density of (a) the electric and (b) magnetic fields. Black solid lines indicate integer multiples of f_{ce} in (a) and $0.5f_{ce}$ in (b). Electron energy flux observed by the fine channel of LEP in the PA ranges corresponds to (c) 0–3° and (d) 42–45°. (e) The ratio of (c) to (d) indicates the difference between the inside and outside loss-cone electron flux.

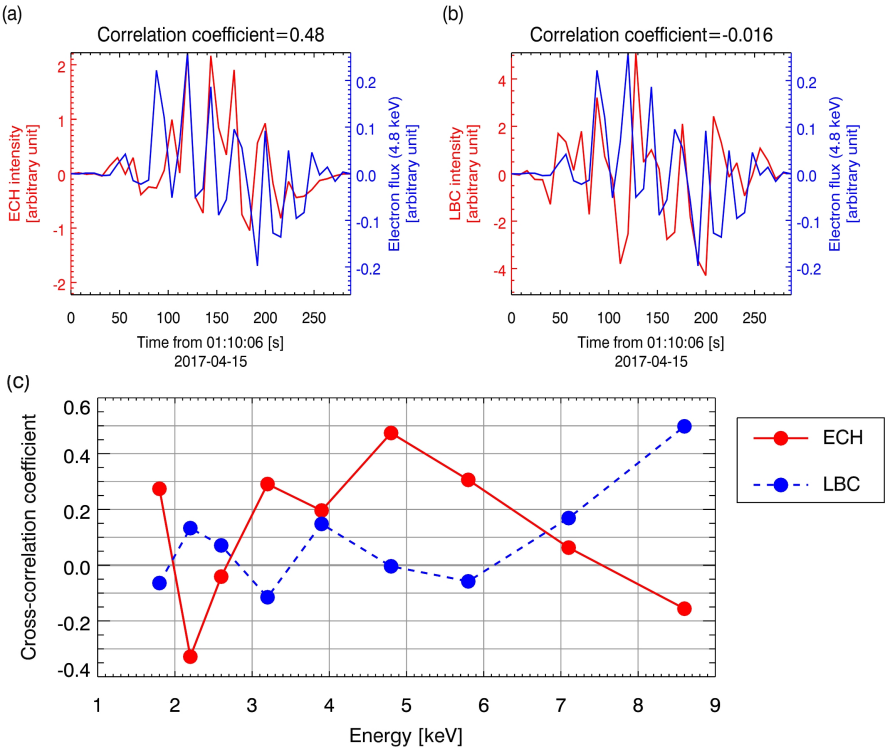

Figure 2.10. Temporal variability, from 01:10:06 UT, of (a) ECH and (b) LBC wave intensities is indicated with a red line, whereas the variability of the loss-cone flux ratio of the 4.8-keV electron is indicated with a blue line. The cross-correlation coefficient between the wave intensity and the electron influx is shown at the top of each panel. (c) Cross-correlation coefficients between the ECH wave intensity and the loss-cone electron flux ratio (shown with red dots and solid line, respectively), and those between the LBC wave intensity and the loss-cone electron flux ratio (shown with blue dots and dashed line, respectively) as a function of electron's energy.

cross-correlation coefficients of different energies against wave intensities (red dots and solid line: ECH; blue dots and dashed line: LBC). The p value of the cross-correlation coefficient between the LBC wave and the loss-cone flux ratio of the 8.6-keV electron is 1.3×10^{-2}, which is smaller than the significance level of 5.0×10^{-2}, whereas that for ECH is 1.5. These results reflect a positive correlation between the ECH wave intensity and the $\sim$5 keV loss-cone energy flux, and between the LBC wave intensity and the $\sim$9 keV loss-cone energy flux, consistently with the general characteristic of the typical resonance energy of LBC being larger than that of ECH.

2.5 Discussion

To quantitatively evaluate whether ECH waves can scatter 5 keV electrons into the loss cone, we calculated the PA diffusion coefficient of ECH waves on the basis of the quasi-linear theory. To calculate the resonance energy of ECH waves, the hot plasma dispersion relation must be solved: however, this cannot be easily done, as in the case of LBC. The PA diffusion coefficient for ECH waves was expressed by Horne

and Thorne [2000] with the following equation

$$
\begin{aligned}
D_{\alpha\alpha} = & \frac{\pi^{1/2}}{2} \frac{e^2}{m_e^2} \frac{|\mathbf{E_w}|^2}{k_{\perp 0}^2 \Delta k_{\parallel}} \frac{1}{v^5 \cos\alpha} \\
& \cdot \sum_{n=-\infty}^{\infty} \left(\frac{n\Omega_e - \omega_k \sin\alpha^2}{\sin\alpha \cos\alpha} \right)^2 \exp(-\lambda) I_n(\lambda) \\
& \cdot \left\{ \exp\left[-\left(\zeta_n^-\right)^2 \right] + \exp\left[-\left(\zeta_n^+\right)^2 \right] \right\},
\end{aligned}
\tag{2.1}
$$

where $\zeta_n^{\pm} = (\omega_{\mathbf{k}} - n\Omega_e) \,/\, \left(\Delta k_{\parallel} v \cos\alpha\right) \pm k_{\parallel 0}/\Delta k_{\parallel}$, $\lambda = k_{\perp 0}^2 / \left(2\Omega_e^2\right)$; $k_{\perp 0}$ and $k_{\parallel 0}$ are the components of the resonant wavenumber vector perpendicular and parallel to the ambient magnetic field $\mathbf{B_0}$, respectively; $\Delta k_{\parallel}$ is the width of the spectrum; $\Omega_e = 2\pi f_{\text{ce}} = |e\mathbf{B_0}/m_e|$ is the angular electron cyclotron frequency; $\omega_{\mathbf{k}}$ is the wave frequency as a function of $\mathbf{k}$; $|\mathbf{E_w}|$ is the wave electric field; α and v are the particle PA and velocity, respectively; e/m_e is the electron charge to mass ratio; and I_n is the modified Bessel function of order n. The bounce-averaged diffusion coefficient can be approximated as [Horne and Thorne, 2000]

$$
\langle D_{\alpha\alpha} \rangle \approx \frac{D_{\alpha\alpha}}{T_{\text{b}}} \int_{-\lambda_{\text{int}}}^{\lambda_{\text{int}}} \frac{2}{v \cos\alpha_{\text{eq}}} ds \quad = T_{\text{frac}} D_{\alpha\alpha},
\tag{2.2}
$$

where $T_{\text{frac}} = 4LR_{\text{e}}\lambda_{\text{int}}/v\cos\alpha_{\text{eq}}T_{\text{b}}$ is the fraction of time when the particle interacts with the wave during one bounce period, T_{b} is the particle bounce period, α_{eq} is the PA at the magnetic equator, λ_{int} is the upper limit of integration in MLAT, and R_{e} is Earth's radius. We set $T_{\text{frac}} = 1$ for electrons with a mirror point smaller than λ_{int}.

The input parameters were determined to be $|\mathbf{E_w}| = 1.0$ mV/m, $\omega_{\mathbf{k}} = 1.6\Omega_e$, and $f_{\text{ce}} = \Omega_e/(2\pi) = 2.5$ kHz based on OFA and MGF observation data, as shown in Figure 2.9a. We set other parameters as $L = 6.1$, $\lambda_{\text{int}} = 3.0°$, and $\alpha = 0$–$3°$. To determine the parameters $k_{\perp 0}$, $k_{\parallel 0}$, and $\Delta k_{\parallel 0} = k_{\perp 0}/\tan(\psi - \Delta\psi) - k_{\parallel 0}$, we need to know k and the wave normal angle ψ, which cannot be obtained from Arase observations, because PWE measures only two components of the electric field. Changing the wave normal angle from 85.0° to 89.5°, Kyoto University Plasma Dispersion Analysis Package (KUPDAP) [Sugiyama *et al*., 2015] was used to obtain k, which corresponds to $\omega_{\mathbf{k}} = 1.6\Omega_e$. The input parameters for KUPDAP, i.e., electron temperature ($T_{\perp}$, $T_{\parallel}$), electron density (n_e), and loss-cone depth (Δ) and width (β), were determined by fitting the phase space density recorded on LEPe with a sum of five subtracted Maxwellian components in agreement with previous studies [Ashour-Abdalla and Kennel, 1978, Horne *et al*., 2003, Liang *et al*., 2010]. The fitting results are shown in Figure 2.11 and estimated parameters are shown in Table 2.1, which are labeled as components 2–6. The input parameters of the coldest component (component 1 in Table 2.1) cannot be obtained from Arase observations since the lower-limit energy of LEPe is about 20 eV. It is difficult to precisely determine the cold electron density from the UHR frequency, since the UHR wave was not detectable during our period of analysis. However, we estimate the cold electron density using the electrostatic $(n+1/2)f_{\text{ce}}$ emissions as a diagnostic tool [Hubbard *et al*., 1979]. Hubbard *et al*. [1979] found that the maximum value of n depends on the combination on the ratios of cold (< 10 eV) to hot plasma

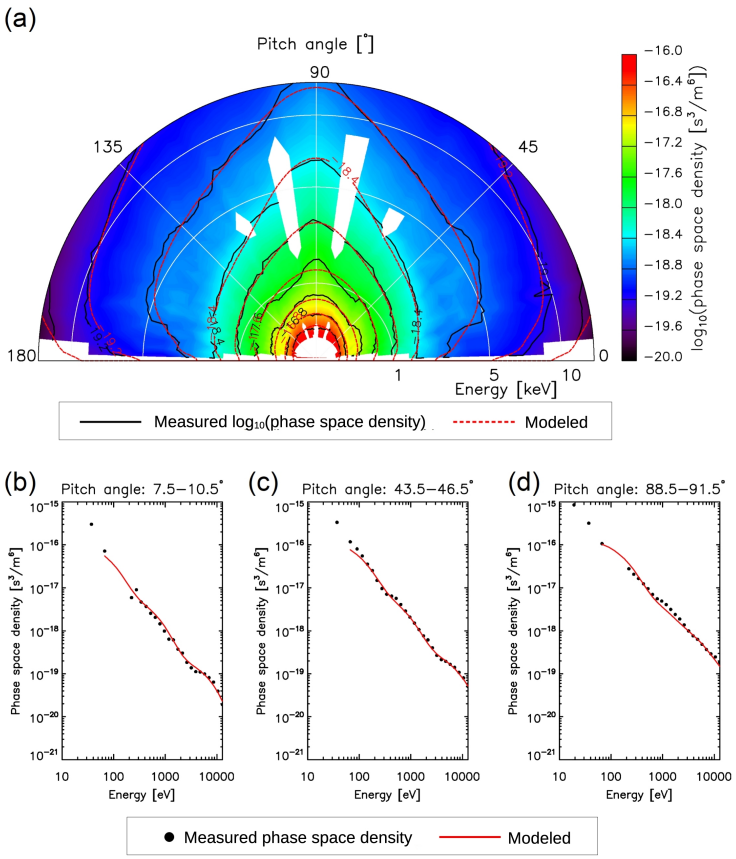

Figure 2.11. (a) Electron PA distribution recorded on the fine LEPe channel (filled contour and black solid lines). The phase space density is averaged over a period of 3 minutes from 01:10–01:13 UT. The contour of the modeled distribution is indicated with dashed red lines. Measured (dots) and modeled (red solid line) electron distribution functions at the PAs of (b) 7.5°–10.5°, (c) 43.5°–46.5°, and (d) 88.5°–91.5° in (a).

density n_c/n_h, and on the plasma frequency to the cyclotron frequency f_p/f_{ce}. During most of the time shown in Figure 2.9a, electrostatic emissions are excited up to $(5+1/2)f_{ce}$. Assuming that the hot electron density is the sum of electron densities of components 2–6 in Table 2.1, we estimated that the cold electron density is 1.9 /cm^3 using equation (2) in Hubbard *et al.* [1979]. Furthermore, we assume that the electron temperature of the coldest component ranges from 1 to 10 eV. To maintain the quasi-neutrality, the proton's distribution function is assumed to be the Maxwellian with the temperature and the density are 1 eV and 2.8 /cm^3, respectively.

Using parameters described above, we calculated bounce-averaged PA diffusion coefficients near the loss cone as a function of electron energy, by modifying normal angle of ECH waves and temperature of coldest component (Figure 2.12a). From Figure 2.10c, it is expected that the PA diffusion coefficient of the ECH wave has a peak at 5 keV. Among the combinations of the electron temperature and the wave normal angle that peak at the PA diffusion coefficient of 5 keV (Figure 2.12b), the linear growth rate of the first harmonic band of the ECH wave calculated using KUPDAP is largest at 8 eV and 88.5° (Figure 2.12c). Under these

Table 2.1. Parameters of multicomponent subtracted Maxwellian in Equation (1) of Liang *et al*. [2010]. The parameters of coldest component 1 are not the result of fitting but assumptions.

Component	$T_\perp$ [eV]	$T_\parallel$ [eV]	n [cm^{-3}]	Δ	β
1	1–10	1–10	1.9	1.0	0.0
2	130	57	0.18	0.90	0.015
3	630	440	0.16	0.82	0.019
4	3.1×10^3	350	0.12	0.73	0.010
5	3.7×10^3	4.2×10^3	0.072	0.63	2.0×10^{-3}
6	1.8×10^4	5.0×10^3	0.33	0.20	0.016

conditions, it is reasonable that the ECH wave contributes to scattering of electrons for 5 keV.

The calculated parallel cyclotron resonance energy of LBC at this time is 4 keV under the first-order cyclotron resonance condition in Kennel and Engelmann [1966]. That near the magnetic equator is smaller than the energy that correlates with the loss-cone flux. However, LBC waves grow, and their resonance energies increase as they propagate to the higher MLAT [Miyoshi *et al*., 2010, 2015a], causing PA scattering of ∼9 keV electrons. More in detail, the resonance energy of LBC reaches 9 keV at the MLAT of -3° during this event. Although ECH and LBC waves were concurrently excited for this event, it must be considered that the difference between their cyclotron resonance energies differentiated their contributions to the PA scattering of inner magnetospheric electrons, as discussed in Fukizawa *et al*. [2018].

Unfortunately, we did not observe auroral emission in this event because the footprint of the Arase satellite was in the sunlit region. The Internal Reference Ionosphere (IRI) and Mass Spectrometer Incoherent Scatter (MSIS) models are used to evaluate ionosphere and thermosphere conditions at the footprint of Arase. To estimate the auroral intensity, the downward electron energy flux, F, at the ionospheric altitudes is estimated as $F \approx (B_\mathrm{i}/B_\mathrm{eq})\, E J_\mathrm{eq} \Delta\Omega \Delta E$ [Kasahara *et al*., 2018a], where B_i and B_eq are the magnetic field strength at the ionosphere and at the equator, respectively; E is the electron's characteristic energy; J_eq is the differential number flux at the magnetic equator; $\Delta\Omega$ is the solid angle of the loss cone; and ΔE is the energy range of precipitation electrons. We adopt $E \approx 5$ keV and $\Delta E \approx 2$ keV from Figure 2.10c, take $B_\mathrm{i} \approx 50,000$ nT from the TS04 model, $B_\mathrm{eq} \approx 88$ nT from the MGF observation, $J_\mathrm{eq} \approx 4.6 \times 10^6$ /s/sr/cm^2/keV from the LEPe observation, and $\Delta\Omega \approx 3.7 \times 10^{-3}$ sr from the angular resolution of LEPe, and adopt a downward electron energy flux of approximately $F \approx 9.7 \times 10^7$ keV/cm^2/s, or 0.15 erg/cm^2/s, which potentially contributes to auroral emissions. The volume emission rate was calculated from the estimated downward electron flux in the altitude range from 80 to 500 km using the electron two-stream model [Ono, 1993]. The column emission intensity of oxygen 557.7-nm aurora was obtained by integrating the volume emission rate. We estimated the column emission intensity to be about 200 R. The estimated column emission intensity and downward energy flux are reasonable values. It is expected that the auroral

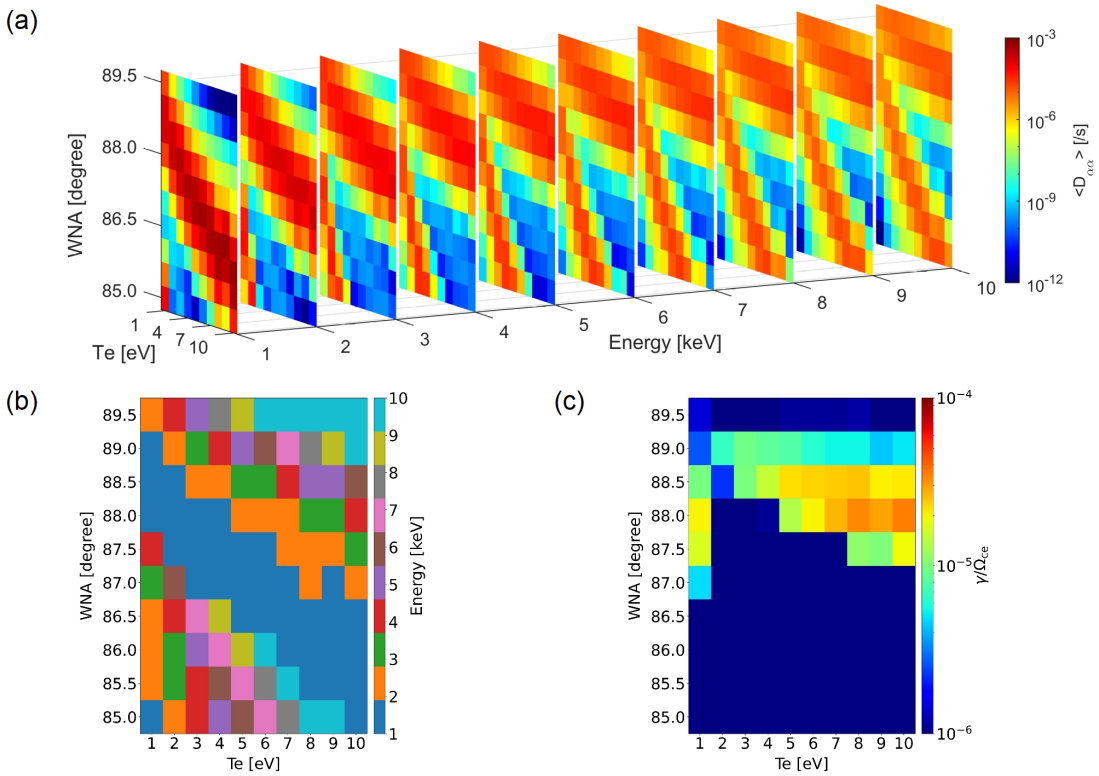

Figure 2.12. (a) Bounce-averaged PA diffusion coefficients near the loss cone as a function of electron energy, by changing wave normal angle of the ECH waves and temperature of coldest component. (b) Energies where (a) have a peak. (c) Linear growth rate of the first harmonic hand of the ECH wave calculated using KUPDAP.

emission has a quasi-periodic modulation, i.e., pulsation, because the electron flux observed by the Arase satellite had a quasi-periodic modulation of 26 s.

Although we suggested that ECH waves caused the PsA emission at 557.7 nm basing on our case study, we cannot exclude the contribution of ECH waves to the auroral emission in the F region. The cyclotron resonance energy of ECH waves has the broad range from a few hundred eV to a few keV; therefore, ECH waves would scatter electrons with energies lower than 1 keV, and thus contribute to cause the auroral emission in the F region. It should be noted that the electron flux inside the loss cone in the energy range lower than $\sim$1 keV was not observed by LEPe considering the present study. We examined the energy range in which ECH waves had high-PA scattering efficiency by a statistical analysis of wave and electron data obtained with Arase in Chapter 3.

2.6 Brief Summary

In this chapter, we calculated the cross-correlation coefficient between the ECH wave intensity and the electron flux observed by the Arase satellite, and demonstrated for the first time that ECH waves cause the PA scattering of electrons into the loss cone in the inner magnetosphere. We analyzed the event during which the downward electron flux in the loss cone and the ECH wave intensity had a quasi-periodic modulation: we found that the ECH wave intensity is correlated with the $\sim$5-keV electron flux in the loss cone. Moreover, the PA diffusion coefficient was calculated to evaluate whether the observed ECH wave could scatter 5 keV electrons into the loss cone. The PA diffusion coefficient of 5-keV electrons is relatively greater than that for other energy electrons, assuming that the electron temperature is 8 eV and the wave normal angle is 88.5°. The observed electron flux correlated with the ECH wave can cause 557.7-nm auroral emission with brightness of about 200 R. It is expected that the auroral emission has a quasi-periodic modulation, i.e., pulsation, since the electron flux observed by the Arase satellite had a quasi-periodic modulation of 26 s. These results suggest that ECH waves propagating nearly perpendicular to the ambient magnetic field scatter a few keV electrons into a loss cone near the magnetic equator of the inner magnetosphere, and probably produce diffuse or pulsating auroral emission. It should be noted that we cannot exclude the contribution of ECH waves to the auroral emission in the F region. We examined the energy range in which ECH waves had high-PA scattering efficiency by a statistical analysis of wave and electron data obtained with Arase in Chapter 3.

3 Strong Diffusion of Low-Energy Electrons by Chorus and ECH Waves [Fukizawa *et al*., 2022a]

In this chapter, we demonstrate that the loss cone filling, known as strong diffusion, of low-energy electrons (0.1–10 keV) associated with LBC, UBC, and ECH waves has been commonly observed in the magnetospheric equatorial region using electron and wave data obtained from the Arase satellite. More in detail, we found that LBC, UBC, and ECH waves contribute to PA scattering of electrons at different energies. Strong diffusion by LBC, UBC, and ECH waves occurred at energies of ∼2–20 keV, ∼1–10 keV, and ∼0.1–2 keV, respectively. The Occurrence rate of the strong diffusion by high-amplitude LBC (>50 pT), UBC (>20 pT), and ECH (>10 mV/m) waves were ∼70%, 40%, and 30% higher than those without considering wave activity, respectively. The energy range in which the occurrence rate was high agreed with the range where the PA diffusion rate of each wave exceeded the strong diffusion level based on the quasilinear theory.

3.1 Background

Previous studies theoretically suggested that ECH waves could fill a loss cone, known as strong diffusion [e.g., Lyons, 1974], in the energy range of a few hundred eV [Horne and Thorne, 2000, Horne *et al*., 2003, Lyons, 1974, Tripathi *et al*., 2011], and thus they could contribute to ∼10–20% of the total electron energy precipitation flux due to ECH, LBC, and UBC waves [Khazanov *et al*., 2015a, Tao *et al*., 2011, Thorne, 2010, Tripathi *et al*., 2013]. However, PA scattering efficiencies of low-energy electrons (0.1–10 keV) by each wave have not been investigated via *in situ* observations due to the difficulties in measuring electron fluxes within loss cones in the magnetosphere. Although a loss cone is usually too small to be resolved in conventional electron measurements in the magnetosphere, the advent of the Arase satellite [Miyoshi *et al*., 2018d] has enabled a direct evaluation of loss cone electron fluxes, with the advantage of a relatively-high-angular resolution of low-energy and energetic electron instruments. Kasahara *et al*. [2019] reported that a strong diffusion of high-energy electrons (10–100 keV) by LBC waves commonly occurs using *in situ* observation data obtained through medium-energy particle experiments-electron analyzer [Kasahara *et al*., 2018b] onboard the Arase satellite. In this chapter, we demonstrate that the strong diffusion of low-energy

electrons associated with LBC, UBC, and ECH waves has been commonly observed in the magnetospheric equatorial region, by using electron data obtained from LEPe [Kazama *et al*., 2017], wave data from OFA [Kasaba *et al*., 2017, Kasahara *et al*., 2018a, Matsuda *et al*., 2018, Ozaki *et al*., 2018], electron density data from HFA [Kumamoto *et al*., 2018], and magnetic field data from MGF [Matsuoka *et al*., 2018b] onboard the Arase satellite.

3.2 Case Study

In order to clarify the relationship among LBC, UBC, and ECH waves, and the electron flux within a loss cone, we carried out a case study using wave and electron observation data obtained through the Arase satellite. Figure 3.1 shows a typical example of wave and electron observation data obtained from 20:00 UT on March 27, 2017 to 2:00 UT on March 28, 2017: this event has been selected since the electron flux within a loss cone has been observed for a relatively long time. The Roederer's L-parameter L^*, MLT, and the magnetic latitude (MLAT) of the Arase satellite are shown as labels in Figure 3.1. More in detail, the value of L^* has been derived for a 90° PA using the TS04 model [Tsyganenko and Sitnov, 2005]. During this event, which happened in a geomagnetically active period with Kp indexes ranging from 4 to 6+, the Arase satellite crossed the magnetic equator from the southern to the northern hemisphere at 23:43 UT. More in detail, the Dst index showed that this event occurred during the recovery phase of storm (not shown).

Figures 3.1a and 3.1b show the power spectral density of wave electric and magnetic fields, respectively. ECH waves were observed in the frequency bands between integer multiples of the local electron cyclotron frequency, $f_{\mathrm{ce\_loc}}$. The magnetic field observed by MGF was used to calculate $f_{\mathrm{ce\_loc}}$. On the other hand, LBC and UBC waves were detected in the lower and upper band of the electron cyclotron frequency at the magnetic equator, $f_{\mathrm{ce\_eq}}$, since LBC and UBC waves are excited near the magnetic equator and propagated to the off-equator. To calculate $f_{\mathrm{ce\_eq}}$, we used the magnetic field intensity derived by tracing the magnetic field line from the satellite position to the magnetic equator with the TS04 model: when the traced magnetic field was larger than the local observed by MGF, the latter was used to calculate $f_{\mathrm{ce\_eq}}$. Figures 3.1c, 3.1d, and 3.1e depict the amplitudes of ECH, UBC, and LBC waves integrated in the frequency hands of 1.00–2.00$f_{\mathrm{ce_loc}}$, 0.50–0.90$f_{\mathrm{ce_eq}}$, and 0.10–0.45$f_{\mathrm{ce_eq}}$, respectively. During this event, ECH and UBC waves have been observed near the magnetic equator (MLAT from $-1°$ to 3° and MLAT from $-3°$ to 8°). Moreover, LBC waves have been observed from the magnetic to the off-equator (MLAT from $-20°$ to 15°): their amplitude was larger in the latter location, whereas ECH and UBC wave amplitudes were larger near the former.

Figures 3.1f and 3.1g depict electron fluxes in PA ranges of 0°–5° and 175°–180°, respectively, whereas Figures 3.1h and 3.1i show electron fluxes averaged for the PA range of 5°–45° and 135°–175°, respectively. The PA resolution of LEPe is $\sim 3.75°$. The PA distribution of electrons was averaged every $5°$ to improve the signal-to-noise ratio. The loss cone angle near the magnetic equator in the inner magnetosphere is

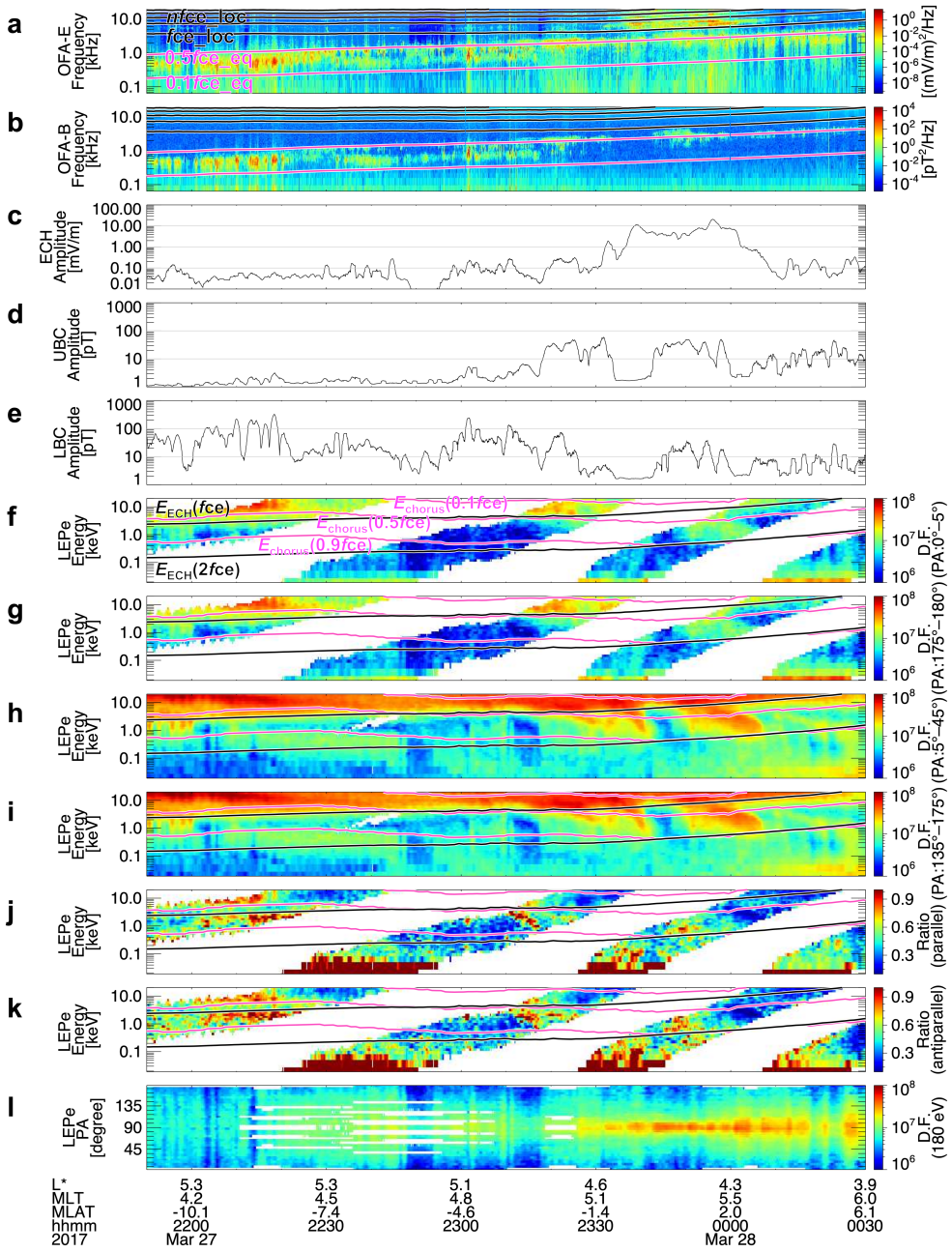

Figure 3.1. Summary plot of wave and particle data obtained with Arase from 20:00 UT on March 27, 2017 to 2:00 UT on March 28, 2017. Frequency-time spectrograms for the (a) wave electric and (b) magnetic fields. Black lines indicate $0.1f_{ce\_eq}$, 0.5 f_{ce_eq}, and nf_{ce_loc} where f_{ce_eq} and f_{ce_loc} are the equatorial and local electron cyclotron frequency, respectively and n is integer. (c, d, and e) ECH, UBC, and LBC wave amplitudes in 1.00–2.00f_{ce_loc}, 0.50–0.90f_{ce_eq}, and 0.10–0.45f_{ce_eq} frequency bands, respectively. Differential fluxes of loss cone electrons ((f) PA ranges of 0° –5° and (g) 175° –180°) and averaged bouncing electrons ((h) PA ranges of 5° –90° and (i) 175° –180°) in the unit of eV/s/cm2/sr/eV. (j and k) Ratios of parallel flux $j(0\text{–}5°)/\langle j(5°\text{–}90°)\rangle$ and antiparallel flux $j(175°\text{–}180°)/\langle j(90°\text{–}175°)\rangle$, respectively. Black solid lines denote cyclotron resonance energies of chorus waves with frequencies of $0.3f_{ce}$, $0.5f_{ce}$, and $0.7f_{ce}$, from top to bottom. Black dashed lines denote cyclotron resonance energies of ECH waves with frequencies of $1.2f_{ce}$ and 1.8 f_{ce}, from bottom to top. (l) PA distribution of 180 eV electrons.

usually smaller than 5°. The loss cone angle calculated using the TS04 model was $\sim 4^\circ$ for this event. Although, the electron fluxes shown in Figures 3.1f and 3.1g include the electron flux outside the loss cone, we assumed that most of them come from the loss cone. Under this assumption, we calculated the loss cone filling ratios for parallel and antiparallel electrons, defined as $j(0^\circ\text{–}5^\circ)/\langle j(5^\circ\text{–}45^\circ)\rangle$ and $j(175^\circ\text{–}180^\circ)/\langle j(135^\circ\text{–}175^\circ)\rangle$, respectively, where j is the energy flux of electrons (Figures 3.1j and 3.1k). The electron flux in PA of $45\text{–}135^\circ$ was not used to exclude the effect of pancake distributions (peaked at PA $\sim 90^\circ$) of electrons [Meredith *et al.*, 2000].

To estimate the driver of the PA scattering, the cyclotron resonance energies of LBC, UBC, and ECH waves were overlaid on the electron flux data in Figures 3.1f–3.1k. The cyclotron resonance energies of chorus waves, E_{chorus}, can be written as follows [Kennel and Petschek, 1966]

$$E_{\text{chorus}} = \frac{B_0^2}{2\mu_0 n_{\text{e}}} \frac{f_{\text{ce}}}{f} \left(1 - \frac{f}{f_{\text{ce}}}\right)^3, \tag{3.1}$$

where B_0 is the ambient magnetic field, f is the wave frequency, f_{ce} is the electron cyclotron frequency, μ_0 is the magnetic permeability in a vacuum, and n_{e} is the electron density derived from the upper hybrid resonance frequency obtained from the *in situ* observation. The lower and upper limits of cyclotron resonance energy for LBC and UBC waves are represented by $E_{\text{chorus}}(f = 0.1f_{\text{ce}}, 0.5f_{\text{ce}}, 0.9f_{\text{ce}})$, which are depicted as magenta lines in Figures 3.1f–3.1k. We used the observed magnetic field for the upper limit of the cyclotron resonance energy for LBC waves $E_{\text{chorus}}(f = 0.1f_{\text{ce}})$ because the LBC waves were observed over the entire range, as shown in Figures 3.1a, 3.1b, and 3.1e. On the other hand, high-amplitude UBC waves were observed in the $|\text{MLAT}| < 3^\circ$ region (Figures 3.1a, 3.1b, and 3.1d). Therefore, the observed magnetic field was used for $|\text{MLAT}| < 3^\circ$, whereas for $|\text{MLAT}| \geq 3^\circ$, the magnetic field at 3° derived using the TS04 model was used to determine the upper and lower limits of the UBC wave cyclotron resonance energy, $E_{\text{chorus}}(f = 0.5f_{\text{ce}})$ and $E_{\text{chorus}}(f = 0.9f_{\text{ce}})$, respectively. The cyclotron resonance energies of ECH waves, E_{ECH}, were calculated using the following equation

$$E_{\text{ECH}} = \frac{1}{2} m_{\text{e}} v_{\text{R}}^2, \tag{3.2}$$

where m_{e} is the electron mass and v_{R} is the velocity that satisfies the cyclotron resonance condition. From the cyclotron resonance condition, we obtain

$$v_{\text{R}} = \frac{2\pi(f - nf_{\text{ce}})}{k_{\parallel}}, \tag{3.3}$$

where $k_{\parallel}$ is the wavenumber parallel to the ambient magnetic field and n is integer. The upper and lower limits of the ECH wave cyclotron resonance energy $E_{\text{ECH}}(f = f_{\text{ce}}, 2f_{\text{ce}})$ are displayed as black lines in Figures 3.1f–3.1k. In the same manner as that for UBC waves, the observed and modeled magnetic field were used to calculate f_{ce} in Eq. 3.3 for $|\text{MLAT}| < 1^\circ$ and $\geq 1^\circ$, respectively. To obtain $k_{\parallel}$ in Eq.

3.3, the dispersion relation was solved using KUPDAP as explained in Section 2.5. Electrons comprised cold and hot components (1 eV and 1 keV, respectively). The cold and hot components were, respectively, Maxwellian and subtracted Maxwellian distributions [e.g., Ashour-Abdalla and Kennel, 1978, Horne, 1989] with loss cone depth and width of $\Delta = 5$ and $\beta = 0.02$ and 89.5° wave normal angle [Horne and Thorne, 2000]. During the time shown in Figure 3.1, the electron density and magnetic field observed by HFA and MGF varied $\sim$4–9 cm^{-3} and $\sim$150–242 nT, respectively (not shown). We used their mean values (7 cm^{-3} and 190 nT) as the total electron density and ambient magnetic field to solve the dispersion relation. The cold electron density is two orders of magnitude larger than the hot one[cf., Kazama *et al*., 2018].

Both parallel and antiparallel loss cone fluxes (Figures 3.1f and 3.1g) and filling ratios in the cyclotron resonance energies of UBC and ECH waves (Figures 3.1j and 3.1k) have been enhanced with high-amplitude ECH and UBC waves near the magnetic equator (MLAT from $-4°$ to 2°) from 23:10 to 00:00 UT. Moreover, those in the cyclotron resonance energies of LBC waves have been enhanced with high-amplitude LBC waves from the magnetic to the off-equator (MLAT = $-10°$ to $-2.5°$) from 22:00 to 23:20 UT: these enhancements provide evidence of PA scattering by each wave.

Between 22:00 and 22:10 UT, an increase in the parallel and antiparallel loss cone flux occurred at energies of several keV (Figures 3.1f and 3.1g), which fall between the resonance energies of $E_{\text{chorus}}(f = 0.5f_{\text{ce}})$ and $E_{\text{chorus}}(f = 0.1f_{\text{ce}})$. This suggests that they are associated with LBC waves. However, the loss cone filling ratios significantly increase at energies corresponding to values lower than $E_{\text{chorus}}(f = 0.5f_{\text{ce}})$ (Figures 3.1j and 3.1k). There is no evidence for UBC or ECH waves in the data at this time (Figures 3.1c and 3.1d); however, it is possible that the diffusion occurred because of UBC and ECH waves being closer to the equator that were not observed at higher latitudes. To summarize this event, for each LBC, UBC, and ECH waves, we found that the loss cone filling ratio in the cyclotron resonance energy range increased with high wave amplitude.

Moreover, the loss cone filling ratios exceeded 1 from 20:00 to 21:50 UT (Figures 3.1j and 3.1k). Figure 3.1l shows the differential flux of 180-eV electrons. Electron beams, which were not caused by PA scattering with plasma waves, have been observed during these excessive enhancements. Therefore, electron data where the loss cone filling ratio exceeds 1 should be excluded in the following statistical analysis because our focus is on the PA scattering by multiple plasma waves.

3.3 Statistical Results

To obtain a statistical view for the strong electron scattering by LBC, UBC, and ECH waves, we analyzed a dataset of waves and electrons obtained with the Arase satellite from March 24, 2017, to August 31, 2020. Figure 3.2g shows the number of data sampling in L^*-MLAT plane. One sample corresponds to one satellite spin ($\sim$8 s). To select typical- to high-amplitude wave events from the dataset, we set the threshold level of amplitude for LBC, UBC, and ECH waves in the 0.10–0.45f_{ce}, 0.50–0.90f_{ce}, and 1.00–2.00f_{ce} frequency

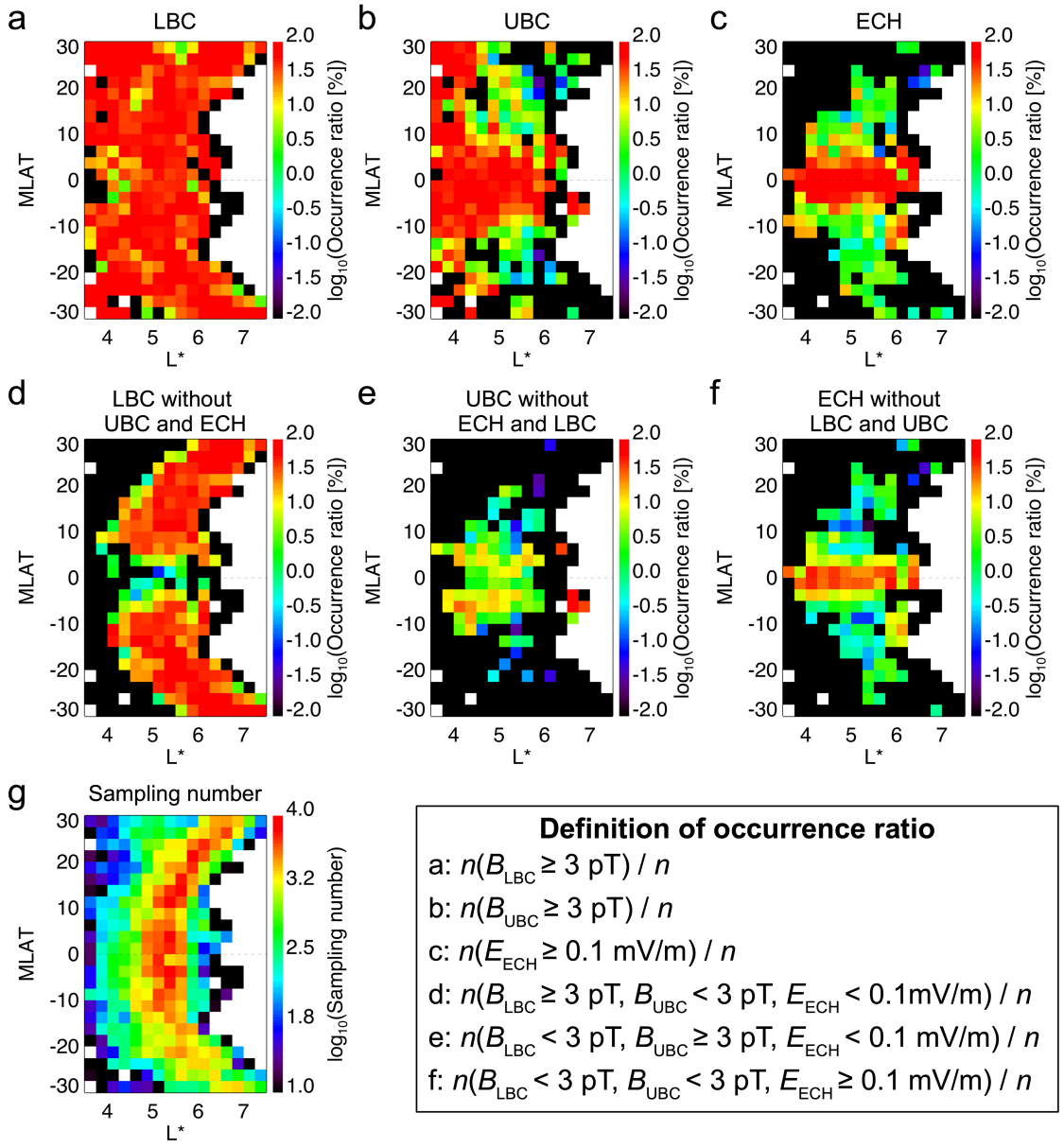

Figure 3.2. Occurrence rates of active (a) LBC, (b) UBC, (c) ECH, (d) LBC waves excluding UBC and ECH, (e) UBC waves excluding LBC and ECH, and (f) ECH waves excluding LBC and UBC in the L^*-MLAT plane. We used a dataset of waves and electrons obtained through the Arase satellite from March 24, 2017, to August 31, 2020. The definition of the occurrence rate is given in the panel, where B_{LBC} and B_{UBC} is the wave magnetic field of LBC and UBC waves, respectively, whereas E_{ECH} is the wave electric field of ECH waves, and n is (g) the sampling number.

bands to 3 pT, 3 pT, and 0.1 mV/m, respectively (c.f., Figures 3.1c–3.1d). Figures 3.2a–3.2c show LBC, UBC, and ECH wave distributions that exceeded each threshold amplitude. A moving average is calculated for each wave amplitude with a 1-min time window. Active LBC waves were frequently observed from the magnetic equator to the off-equator, whereas active UBC and ECH waves have been frequently observed near the magnetic equator. It is not easy to examine the one-to-one correspondence between the loss cone filling ratio and individual wave amplitude, since these waves are often simultaneously observed as seen in Figures 3.1a–3.1e.

We selected the dataset according to when the wave amplitude of interest was higher than the threshold amplitude, and the other two wave amplitudes were smaller than the threshold amplitude. Figures 3.2d–3.2f show the occurrence rates of LBC waves excluding UBC and ECH, UBC waves excluding LBC and ECH, and ECH waves excluding LBC and UBC in the L^*-MLAT plane. The definition of the occurrence rate is shown in Figure 3.2.

The cyclotron resonance energy of LBC waves increased as they propagated to a higher MLAT region from the magnetic equator: the energy reached a few MeV [Miyoshi *et al*., 2015a, 2020], while the upper energy limit of the LEPe instrument was $\sim$20 keV. Moreover, the loss cone filling ratios observed in off-equator regions included the effect of the PA scattering near the magnetic equator: therefore, we used the dataset obtained near the magnetic equator ($|\mathrm{MLAT}| < 5^\circ$). It should be noted that the relationship between LBC waves and the $\sim$10–100-keV electron flux within the loss cone was investigated by Kasahara *et al*. [2019] using medium-energy particle experiments–electron analyzer (MEPe) onboard the Arase satellite. Although 70-keV–1-MeV and 400-keV–20-MeV electrons have been observed by high-energy electron (HEP) and extremely high-energy electron experiment (XEP), respectively, HEP and XEP cannot resolve the electron flux within the loss cone.

To remove the dataset possibly related to plasma sheet phenomena, such as PA scattering due to the magnetic field line curvature [Büchner and Zelenyi, 1989, Young *et al*., 2008], we discarded the dataset if the angle between the background magnetic field and the model dipole field was $>30^\circ$ [cf., Kasahara *et al*., 2019]. Moreover, we used the dataset obtained outside the plasmapause ($L^* > 4$ and $n_\mathrm{e} < 30\ \mathrm{cm}^{-3}$, where n_e is the electron density) to exclude the contribution from plasmaspheric hiss. Visual inspection confirmed that this threshold successfully removed the whistler hiss without the significant omission of chorus activities. Finally, we did not use the wave data 1 min before and after calibration pulses of the PWE instrument [Matsuda *et al*., 2018] and the electron data during commissioning operations.

Extracted data of wave amplitudes and loss cone filling ratios are shown in Figures 3.3–3.5 as scatter plots of LBC, UBC, and ECH wave amplitudes versus the loss cone filling ratios in logarithmic scales. In order to exclude the contribution from electron beams, we excluded the dataset associated with a loss cone filling ratio exceeding 1, and wave amplitudes lower than 3 pT, 3 pT, and 0.1 mV/m for LBC, UBC, and ECH waves, respectively, as explained in Subsection 3.2. Red circles show median values of loss cone

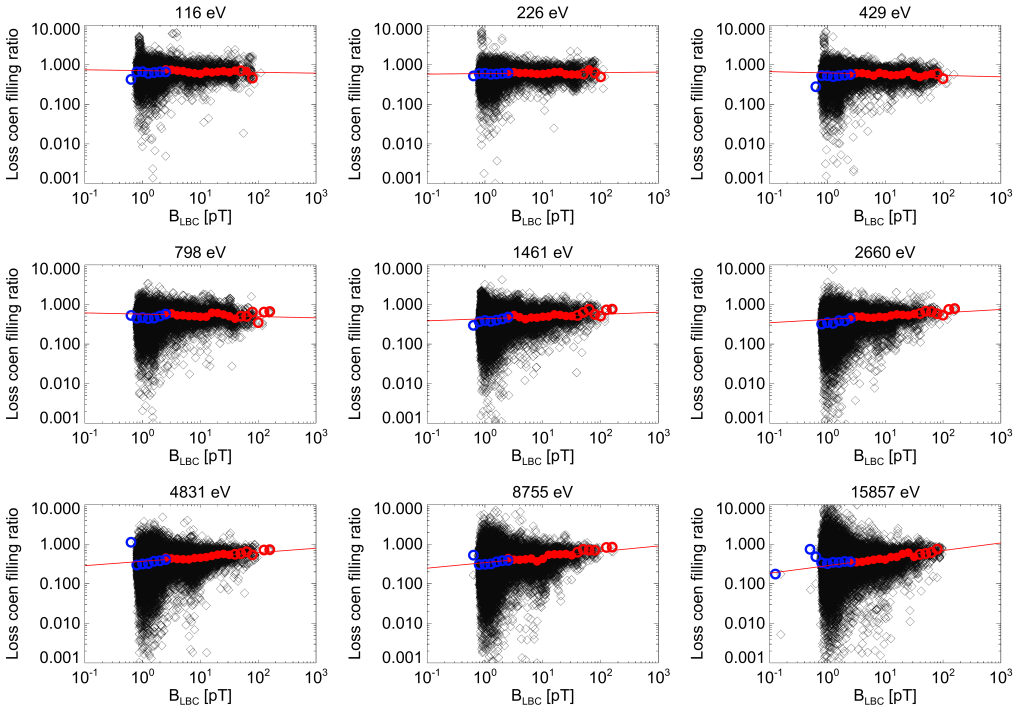

Figure 3.3. Scatter plots of LBC wave amplitudes versus loss cone filling ratios in logarithmic scales (black diamonds). Red circles show median values of loss cone filling ratios obtained with amplitude intervals of the logarithm of 0.1. The median values where the amount of data is $\leq$1% of the amount of data are indicated by red open circles. Blue open circles show the median value lower than the threshold value. Red lines show regression lines determined using the least square method using red filled circles.

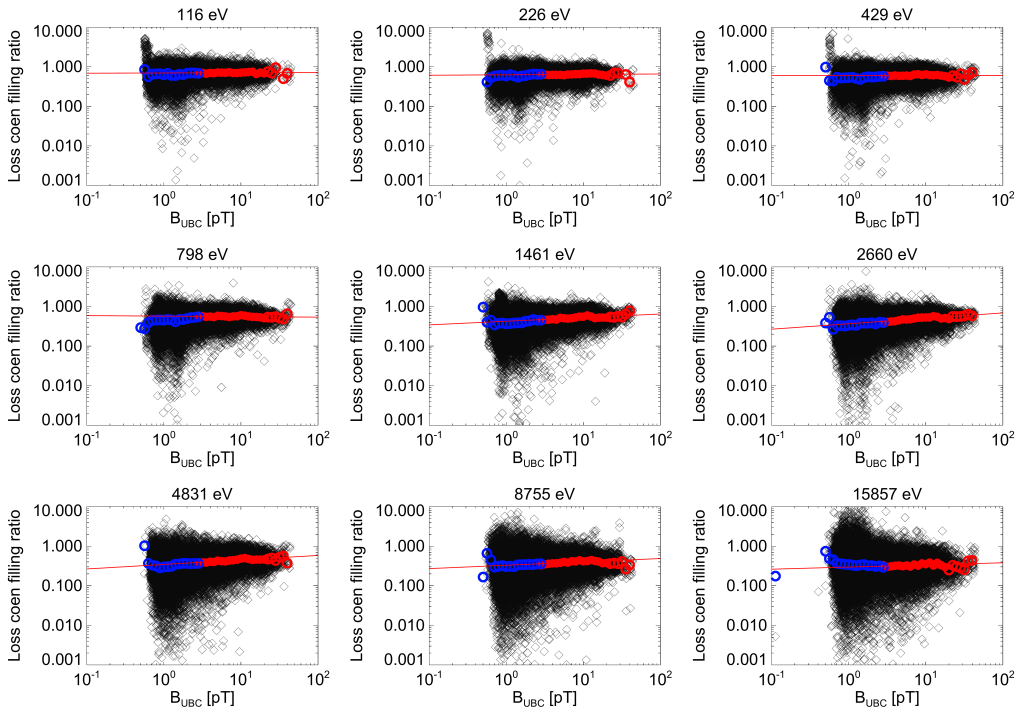

Figure 3.4. Scatter plots of UBC wave amplitudes versus loss cone filling ratios in the same format as Figure 3.3. Red filled and open circles show median values of loss cone filling ratios obtained with amplitude intervals of the logarithm of 0.05.

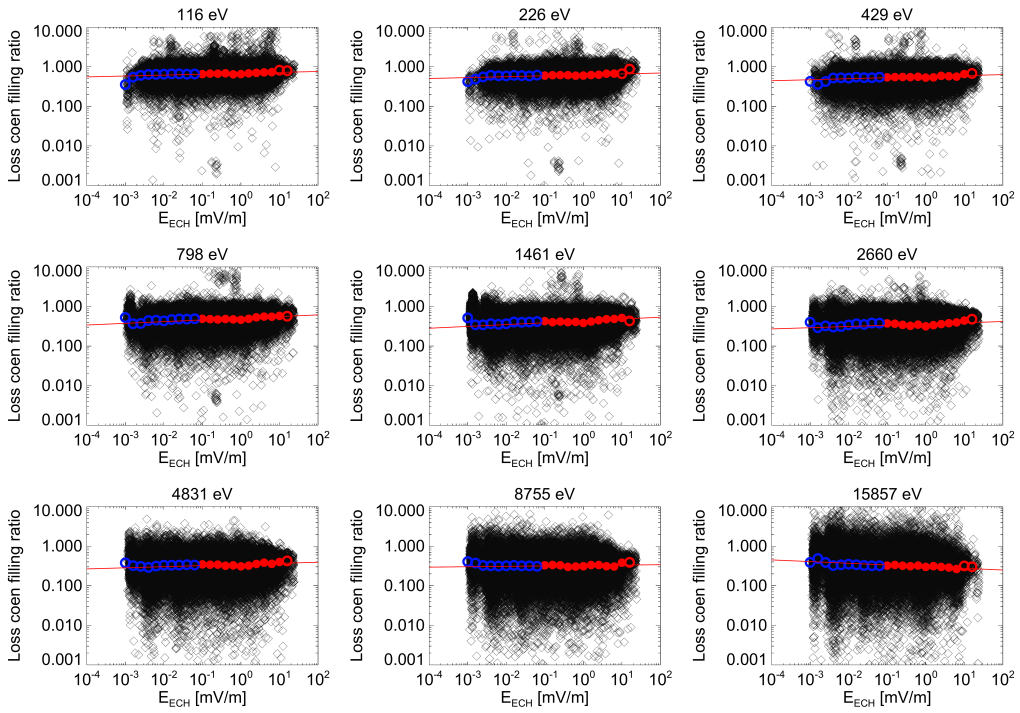

Figure 3.5. Scatter plots of ECH wave amplitudes versus loss cone filling ratios in the same format as Figure S1. Red filled and open circles show median values of loss cone filling ratios obtained with amplitude intervals of the logarithm of 0.2.

filling ratios obtained with amplitude intervals of logarithms of 0.1, 0.05, and 0.2 for LBC, UBC, and ECH waves, respectively. The median values where the amount of data used to calculate the median value is $\leq$1% of the total amount of data are indicated by red open circles. To quantify the contribution of the PA scattering by each wave, we estimated the slope of the regression line determined by the least square fitting to the loss cone filling ratios indicated by red filled circles. Moreover, to confirm the accuracy of the contribution estimation, we calculated Kendall's rank correlation coefficients and the two-sided significance of its deviation from zero using the loss cone filling ratios indicated by the red filled circles.

Figure 3.6 shows the estimated slopes, their 2σ uncertainties, and correlation coefficients for all energies. When we consider the problem of fitting a set of N data points (x_i, y_i) to a straight-line model $y = ax + b$, the uncertainty σ was calculated as

$$\sigma = \sqrt{\frac{1}{N}\left(1 + \frac{\left(\sum_{i=1}^{N} x_i\right)^2}{N\sum_{i=1}^{N} t_i^2}\right)\frac{\chi^2}{N-2}}, \tag{3.4}$$

where

$$\chi^2 = \sum_{i=1}^{N} (y_i - a - bx_i)^2, \tag{3.5}$$

and

$$t_i = x_i - \frac{\sum_{i=1}^{N} x_i}{N}. \tag{3.6}$$

Details of the σ derivation are explained in Section 15.2 on Press *et al*. [1992]. The LBC wave has a positive slope with a statistically significant correlation coefficient at energies greater than $\sim$2 keV, whereas the ECH wave has a smaller positive slope at energies lower than $\sim$2 keV, accordingly with the typical cyclotron resonance energy range of each wave mode. On the other hand, the UBC wave has a positive slope with a statistically significant correlation coefficient in the energy range of $\sim$1–10 keV.

Furthermore, to examine how often the strong diffusion or approaching strong diffusion occurs by LBC, UBC, and ECH waves, we calculated occurrence rates using the same extracted dataset. Figure 3.7a shows the occurrence rates of strong diffusion with typical-amplitude LBC, UBC, and ECH waves, and without wave activities. The occurrence rate of strong diffusion with LBC, UBC, and ECH waves were calculated as $n(r > 0.5)/n$ for the samples under the condition of 10 pT $\leq B_{\mathrm{LBC}} <$ 50 pT, $B_{\mathrm{UBC}} <$ 3 pT, and $E_{\mathrm{ECH}} <$ 0.1 mV/m; $B_{\mathrm{LBC}} <$ 3 pT, 10 pT $\leq B_{\mathrm{UBC}} <$ 20 pT, and $E_{\mathrm{ECH}} <$ 0.1 mV/m; and $B_{\mathrm{LBC}} <$ 3 pT, $B_{\mathrm{UBC}} <$ 3 pT, and 1 mV/m $\leq E_{\mathrm{ECH}} <$ 10 mV/m, respectively, where n is the number of data points, and r is the loss cone filling ratio. The occurrence rate of strong diffusion without wave activity is defined to be $n(r > 0.5)/n$ under the condition of $B_{\mathrm{LBC}} <$ 3 pT, $B_{\mathrm{UBC}} <$ 3 pT, and $E_{\mathrm{ECH}} <$ 0.1 mV/m and is labeled as "No wave" in Figures 3.7a and 3.7b. Although strong diffusion is defined as occurring when the loss

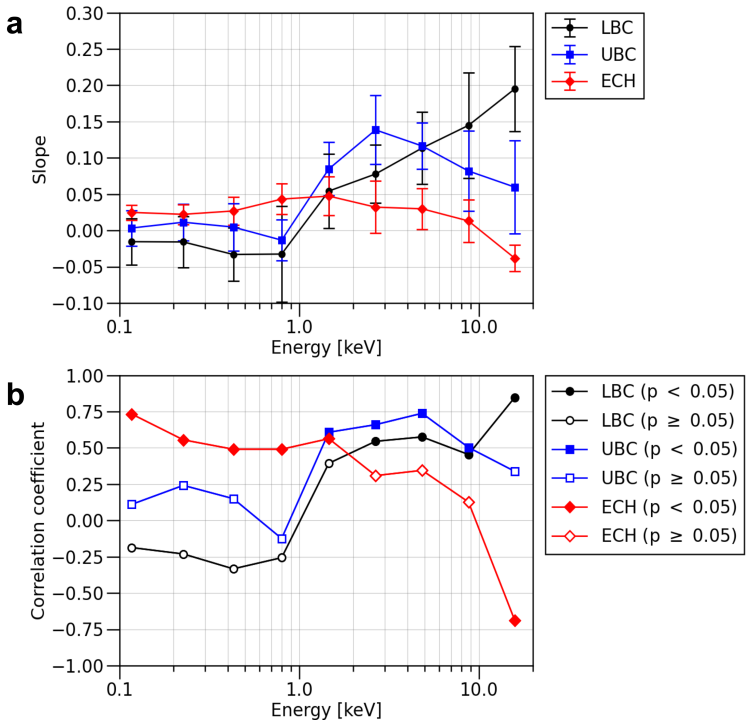

Figure 3.6. Energy dependence of (a) regression line slopes and (b) Kendall's rank correlation coefficients between loss cone filling ratios and LBC (black circles), UBC (blue squares), and ECH (red diamonds) wave amplitudes. Error bars in Figure 3.6a indicate the 2σ level. Filled and open symbols in Figure 3.6b indicate $p < 0.05$ and $p \geq 0.05$, respectively.

cone is filled (i.e., $r = 1$), a large number of data had values of <1 even when each wave exhibited a large amplitude was large (Figures 3.3–3.5). This is consistent with Figure 3 in Reidy *et al.* [2021], which shows that the PA distribution is not quite flat, even when the bounce averaged pitch angle diffusion coefficient of chorus waves reached the strong diffusion limit. Moreover, note that LEPe instrument does not completely observe the electron flux in the loss cone. Furthermore, short bursts of chorus waves reduce the average flux in the loss cone because the precipitation takes a certain time. Thus, we set a threshold value of 0.5 for the loss cone filling ratio to define strong diffusion.

If a simultaneous wave activity is not observed, the loss cone is not empty, in particular at lower energies ($< \sim$1 keV), attributable to the effect of PA scattering at different MLATs on the same magnetic field line or to backscattered electrons. Therefore, the contribution for the strong diffusion by wave activity can be observed by comparing the occurrence rate with each wave activity and that without considering wave activities. At $\sim$10 keV, the occurrence rate of strong diffusion by LBC waves was the highest of the three waves and $\sim$30% higher than those without wave activity. Meanwhile, in the energy range lower than a few keV, the occurrence rate of strong diffusion by UBC waves was highest and $\sim$10%–40% higher than those without wave activity.

Figure 3.7b shows the occurrence rate of strong diffusion by higher-amplitude waves. The occurrence rate was calculated under the condition of $B_{\mathrm{LBC}} \geq 50$ pT, $B_{\mathrm{UBC}} \geq 20$ pT, and $E_{\mathrm{ECH}} \geq 10$ mV/m. In an

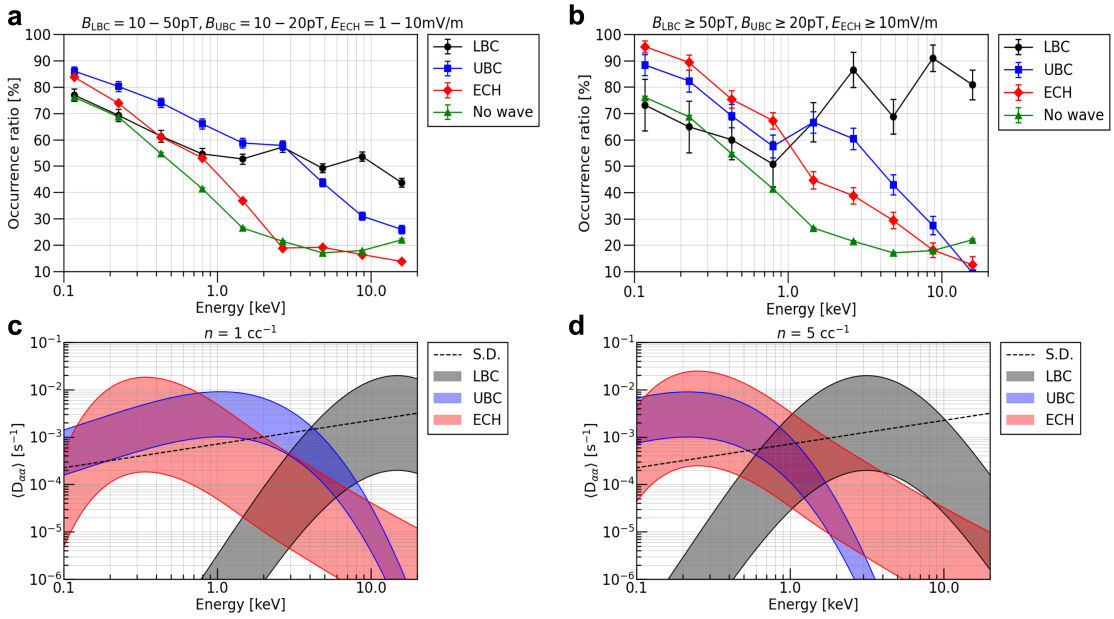

Figure 3.7. Energy dependence of occurrence rates of strong diffusion by (a) typical- and (b) high-amplitude LBC (black circles), UBC (blue squares), and ECH (red diamonds) waves. Amplitude ranges are shown at the top of each panel. Green triangle shows occurrence rates of strong diffusion without simultaneous wave activity. Bounce-averaged PA diffusion coefficients ($\langle D_{\alpha\alpha} \rangle$) of LBC (black), UBC (blue), and ECH waves (red) as a function of the electron energy for electron densities of (c) 1 and (d) 5 cm^{-3}. The upper and lower ends of the bands represent $\langle D_{\alpha\alpha} \rangle$ for 10 and 100 pT (LBC), 10 and 30 pT (UBC), and 1 and 10 mV/m (ECH), respectively. The dashed line indicates the strong diffusion level.

energy range greater than 2 keV, the occurrence rate by higher-amplitude LBC waves (Figure 3.7b) was higher than that by lower-amplitude LBC waves (Figure 3.7a) and ∼50%–70% higher than that without considering simultaneous wave activities. In an energy range lower than 1 keV, the occurrence rate by ECH waves was the highest of the three waves and ∼20%–30% higher than that without simultaneous wave activities. These results show that the contribution of ECH waves to the strong diffusion is dominant among three waves when the wave amplitude is high (≥10 mV/m).

To examine the energy range where each wave can fill the loss cone, we calculated the bounce-averaged PA diffusion coefficient $\langle D\alpha\alpha \rangle$ (see Section 1.6) at PA = 2.5° and $L = 6$ as a function of energy, and compared with the strong diffusion level [Horne and Thorne, 2000]. The bounce-averaged first-order cyclotron resonance diffusion coefficient was calculated by the method given in Shprits *et al*. [2006] for parallel propagating LBC and UBC waves. Additionally, the bounce-averaged first- to tenth-order cyclotron resonance and Landau resonance diffusion coefficients were calculated using the method in Horne and Thorne [2000] for ECH waves. The contribution from the first- and second- order cyclotron resonance was dominant for ECH waves (not shown). The power spectral density was assumed to be Gaussian centered at $f_m = 0.35 f_{\rm ce}$ and $f_m = 0.65 f_{\rm ce}$ for LBC and UBC waves, respectively, with a standard deviation (bandwidth) $\delta f = 0.15 f_{\rm ce}/\sqrt{2}$ and bounded by upper ($f_m + 2\sqrt{2}\delta f$) and lower ($f_m - 2\sqrt{2}\delta f$) cutoffs, resembling typical LBC and UBC in the same manner as Shprits *et al*. [2006]. Both LBC and UBC wave amplitudes were assumed to be spatially uniform at |MLAT|≤ 10° and set to 0 at |MLAT|> 10°. In our observations, there was a large ambiguity in electron density outside the plasmapause, since the UHR frequency cannot be identified by the HFA observation. Therefore, we made calculations considering two density values (n_0 = 1 and 5 cm^{-3}) [cf., Sheeley *et al*., 2001]. The peak frequency of the wave spectrum for ECH waves was assumed to be $1.5 f_{\rm ce}$, while the peak wavenumber was obtained by solving the dispersion relation with KUPDAP. The electron distributions explained in Subsection 3.2 have been used; only the total electron density was changed to $n_0 = 1$ and 5 cm^{-3}. We assumed the wave growth was centered at a propagation angle of $\psi = 89.5°$ and an angular width of $\Delta\psi = 0.5°$ [Horne and Thorne, 2000]. The ECH wave amplitude was assumed to be spatially uniform at |MLAT| ≤ 3° and was set to 0 at |MLAT| > 3° [Gough *et al*., 1979, Meredith *et al*., 2009, Ni *et al*., 2017].

Figures 3.7c and 3.7d show calculated $\langle D_{\alpha\alpha} \rangle$ for $n_0 = 1$ and 5 cm^{-3}, respectively. Energy ranges where the calculated $\langle D_{\alpha\alpha} \rangle$ exceeded the strong diffusion level were almost consistent with those where the occurrence rates of strong diffusion are high for each wave. Note that there was the energy range where the occurrence rate of strong diffusion was ∼10% larger than those without simultaneous wave activity even when the diffusion coefficient did not exceed the strong diffusion limit. This discrepancy would be attributed to the threshold value of $r = 0.5$ to define the occurrence rate of strong diffusion since each wave can fill the loss cone to some extent even if the diffusion coefficient is smaller than the strong diffusion limit. The PA scattering by other waves at different MLAT would increase the occurrence rate in these

energy ranges.

Moreover, the occurrence rate of strong diffusion with UBC waves is higher than that without simultaneous wave activity at energies greater than a few keV (Figures 3.7a and 3.7b), but the PA diffusion coefficient did not exceed the strong diffusion limit in these energies (Figures 3.7c and 3.7d). If we change the threshold value of wave amplitude to exclude ECH waves stricter from 0.1 to 0.01 mV/m, the occurrence rate with UBC waves in these energies becomes smaller than that without simultaneous wave activity (not shown), implying that the strong diffusion at energies greater than a few keV is not due to UBC waves.

3.4 Brief Summary and Discussion

In this chapter, we revealed the energy ranges where LBC, UBC, and ECH waves contribute to scattering electrons in loss cones, by using *in situ* observation data obtained by LEPe and OFA on the Arase satellite. From the case study, we reported that the loss cone filling ratios were enhanced in the cyclotron resonance energy ranges of LBC, UBC, and ECH waves with corresponding wave enhancements. Statistical results showed that the regression line slopes for wave amplitudes versus loss cone filling ratios were positive, and correlation coefficients between them were statistically significant at energies greater than $\sim$2 keV for LBC waves, from $\sim$1 to $\sim$10 keV for UBC waves, and lower than $\sim$2 keV for ECH waves. The strong PA scattering commonly occurred in almost the same energy range for each wave, accordingly with the energy ranges that PA diffusion coefficients exceeded the strong diffusion level on the basis of the quasi-linear theory.

Landau resonance between chorus waves and electrons could cause electron flux enhancement parallel to the magnetic field, generating a large ratio between the parallel and perpendicular fluxes [e.g., Ma *et al*., 2017]. However, waves with large magnetic field amplitudes typically have relatively small wave normal angles, whose cyclotron scattering may be more efficient than Landau acceleration. The contribution of Landau resonance to PA scattering should be examined using statistical analysis that incorporates the wave normal angle.

Previously, studies demonstrated that the contribution of ECH waves to strong diffusion is relatively small, compared to LBC and UBC waves [Khazanov *et al*., 2015a, Tao *et al*., 2011, Thorne, 2010, Tripathi *et al*., 2013]. Recently, Kazama *et al*. [2021] identified via Arase observations that both LBC and UBC waves contribute to the electron PA scattering near the equator. On the other hand, PA scattering of keV electrons in a loss cone by ECH waves was reported using ground-based all-sky imager and Arase satellite observations [Fukizawa *et al*., 2018, 2020]. Although these previous studies are based on case studies, our study is based of statistical analyses of data obtained with a relatively high-angular-resolution electron instrument onboard the Arase satellite. More in detail, our statistical analysis demonstrated that LBC waves commonly scattered electrons of energies greater than a few keV in loss cones near the inner magnetospheric magnetic equator ($L^* = 4$–6 and $|\mathrm{MLAT}| < 5^\circ$) and made strong diffusion of electrons. On the other hand,

we showed that ECH waves scattered electrons in the loss cone in an energy range lower than $\sim$1 keV, and made strong diffusion of electrons at an energy of $\sim$0.1 keV with an occurrence rate of $\sim$95%. Therefore, PA scattering by ECH waves contributes to loss of plasma sheet electrons and emissions of diffuse aurora in the inner magnetosphere.

4 Electron Density Enhancement in the *F* Region Associated with PsA [Fukizawa *et al.*, 2021]

As described in Section 1.7, previous studies showed that PsAs are generally caused by high-energy electron precipitation with a typical energy greater than a few keV. Additionally, soft electron precipitation ($<$ a few keV) has often been observed as associated with PsAs, and may enhance the electron density in the ionospheric *F* region. However, to date, the relationship between PsAs and soft electron precipitation has not been fully understood. In this chapter, we concern two PsA events on the relationship between the electron density height profile and the aurora type, by using data taken by the EISCAT radar and the auroral all-sky imager at Tromsø. Additionally, we conducted statistical studies for 14 events to elucidate how often *F* region electron density enhancement occurs associated with a PsA. We consequently found that 76% of electron density height profiles showed a local peak in the *F* region with electron temperature enhancements. Furthermore, it was found that 89% of the *F* region peak altitudes were above the peak altitude of the ionization rate produced by electrons with a characteristic energy lower than 100 eV. The occurrence rate of these profiles exceeded 80% in the 22–3 MLT ranges. We suggest that the electron density enhancement in the *F* region could be caused by ECH waves in the magnetosphere.

4.1 Background

In addition to the energetic ($>$ a few keV), the soft electron precipitation associated with PsAs in an energy range smaller than a few keV has often been observed by sounding rockets and low-altitude satellites [e.g., McEwen *et al.*, 1981, Miyoshi *et al.*, 2015a, Tesema *et al.*, 2020a]. The generation process of electron precipitation of energies from 100 eV to a few keV in the PsAs region is considered to be the pitch angle scattering by UBC and ECH waves near the magnetic equator [e.g., Fukizawa *et al.*, 2018, 2020, Khazanov *et al.*, 2015a, Miyoshi *et al.*, 2015b, Su *et al.*, 2009, 2010, Tao *et al.*, 2011, Thorne *et al.*, 2013]. On the other hand, electron precipitation in an energy range greater than 100 eV generated by LBC, UBC, and ECH waves causes a cascading toward thermal energies and the production of secondary electrons ($<$ 100 eV) via impact ionization of the neutral atmosphere: these electrons can escape to the magnetosphere, and precipitate into the conjugate ionosphere. This process can occur multiple times, and enhances the

low-energy electron spectra in diffuse or pulsating auroras [Khazanov *et al*., 2014, 2015a,b].

Soft electron precipitation is of crucial importance since it contributes to the background diffuse auroral emission and the ionization in the ionospheric *F* region, as well as to high-energy electron precipitation [Saito *et al*., 1992, Sandahl *et al*., 1980, Smith *et al*., 1980, Whalen *et al*., 1971]. The electron temperature in the ionospheric *F* region is enhanced by soft electron precipitation in PsAs [Liang *et al*., 2017, 2018]. Oyama *et al*. [2014] reported double-peak structures of the ionospheric electron density in *E* and *F* regions at the beginning of the substorm recovery phase basing on the data taken by the EISCAT radar: more in detail, they attributed the enhancement of the *F* region electron density to lower energy electron precipitation and long-lived plasma that drifted horizontally from the dayside. Furthermore, ionospheric electron heating associated with PsAs has been observed by the Swarm satellite: soft electron precipitation may have had some effects on it [Liang *et al*., 2018]. By contrast, Samara *et al*. [2015] reported that soft electron precipitation was reduced during strongly temporally varying PsAs, due to the field-aligned current with parallel potential drops up to 1 kV. Although soft electron precipitation associated with PsA has been reported in past studies, its detailed characteristics and generation mechanism are not entirely understood.

In this chapter, we aim to elucidate the characteristics of soft electron precipitation in PsAs using ionospheric electron density altitude profiles obtained through the EISCAT radar, while PsAs have been observed by the all-sky imager. We focus on two events to investigate in detail the relationship between the electron density height profile and the type of aurora. Additionally, we performed a statistical analysis of 14 events to examine the characteristics of the *F* region ionization in PsAs.

4.2 Instrumentation

4.2.1 All-Sky Imagers

We used two Watec Monochromatic Imagers (WMIs) at Tromsø, Norway (69.58°N, 19.23°E, 66.40° MLAT), which consist of a highly-sensitive camera with a charge-coupled device made by Watec Co. Ltd, a fish-eye lens by Fujinon Co. Ltd., and a band-pass filter. The central wavelengths of the band-pass filters were 560 and 632 nm, with the full width at half maximum of 10 nm [Ogawa *et al*., 2020]. More in detail, WMI with a 560-nm filter has been used to detect PsAs: PsA emissions are dominated by the atomic oxygen green line at 558 nm of which the typical altitude is in the *E* region. Thus, the auroral green line emission was used as an indicator of relatively high-energy electron precipitation. Moreover, the temporal resolution of 558-nm data was 1 s: this was sufficient to observe the main modulation of the PsAs, whose typical quasi-periodicity ranged from a few to tens of seconds. On the other hand, WMI with a 632-nm filter has been used to detect the atomic oxygen red line at 630 nm in the *F* region, caused by soft electron precipitation: the temporal resolution was 4 s. Hereafter, we call these two WMIs WMI-558 and WMI-630, respectively.

4.2.2 EISCAT UHF Radar

We used the data obtained by the EISCAT UHF radar at Tromsø with the CP1 mode [Folkestad *et al.*, 1983] to estimate the electron density and temperature in the altitude range of 76–282 or 76–647 km along the local geomagnetic field direction. The altitude resolution was in the range of 3–33 km, while the temporal resolution was 1 min.

4.3 Case Studies

4.3.1 Case 1: 0–4 UT on February 18, 2018

Figures 4.1a and 4.1b show the keograms obtained from the cross-section of successive all-sky images with WMI-558 and WMI-630. We selected the cross-section along the geographic north–south meridian direction to involve a pixel of the EISCAT radar observation point. After the auroral breakup at 00:10 UT, the following three types of auroras were observed: (A) amorphous PsAs from 00:11 to 00:20 UT, (B) auroral streamers from 00:31 to 00:34 UT, and (C) patchy PsAs from 00:46 to 03:00 UT. The former is an irregularly shaped and rapidly varying PsA, while the latter comprises stable emission structures with pulsations over a large fraction of their spatial extent [Grono and Donovan, 2018]. Figures 4.1c–4.1f show the 558 and 630 nm emission intensities, electron density, and temperature at the EISCAT observation point. The electron density had a peak at an altitude of $\sim$100 km when a discrete aurora appeared (Figure 4.1e), while that at $\sim$130 km altitude was enhanced with the auroral streamer (Figure 4.1e). When the 558 nm auroral emission started quasi-periodic modulations (Figures 4.1a and 4.1c), the electron density at $\sim$200 km altitude decreased, and a weak peak at $\sim$250 km altitude emerged (Figure 4.1e), consistently with that reported by Oyama *et al.* [2014]. Median height profiles of the electron density and temperature for the periods of A, B, and C are shown in Figures 4.2a and 4.2b, respectively. In C, median profiles were derived for data where the median electron temperature in the 240–270 km altitude range was larger than its median value from 00:00–03:53 UT. The median height profile of electron temperature from 00:00–03:53 UT is shown in Figure 4.2b. These electron density enhancements in the *E* region have probably been caused by electron precipitation, since they were followed by electron temperature enhancements relative to the background temperature (green dotted line in Figure 4.2b).

To examine the relationship between the electron density enhancement in the *F* region and the characteristic energy of precipitating electrons, we compared auroral images at 558 nm with those at 630 nm. Figure 4.3 shows a series of auroral images with an interval of 12 s at 558 and 630 nm from 00:53:02 to 00:53:38 UT at the beginning of C, when the ON–OFF modulation of the auroral emission was observed. The 558-nm PsA's patch brightened at the EISCAT radar observation point, as indicated by a white plus mark in Figures 4.3a, 4.3b, and 4.3d. On the other hand, the 630-nm PsA's patch, whose shape was similar to the former, also brightened, as shown in Figures 4.3f and 4.3h. Regarding the WMI-630 data, this type

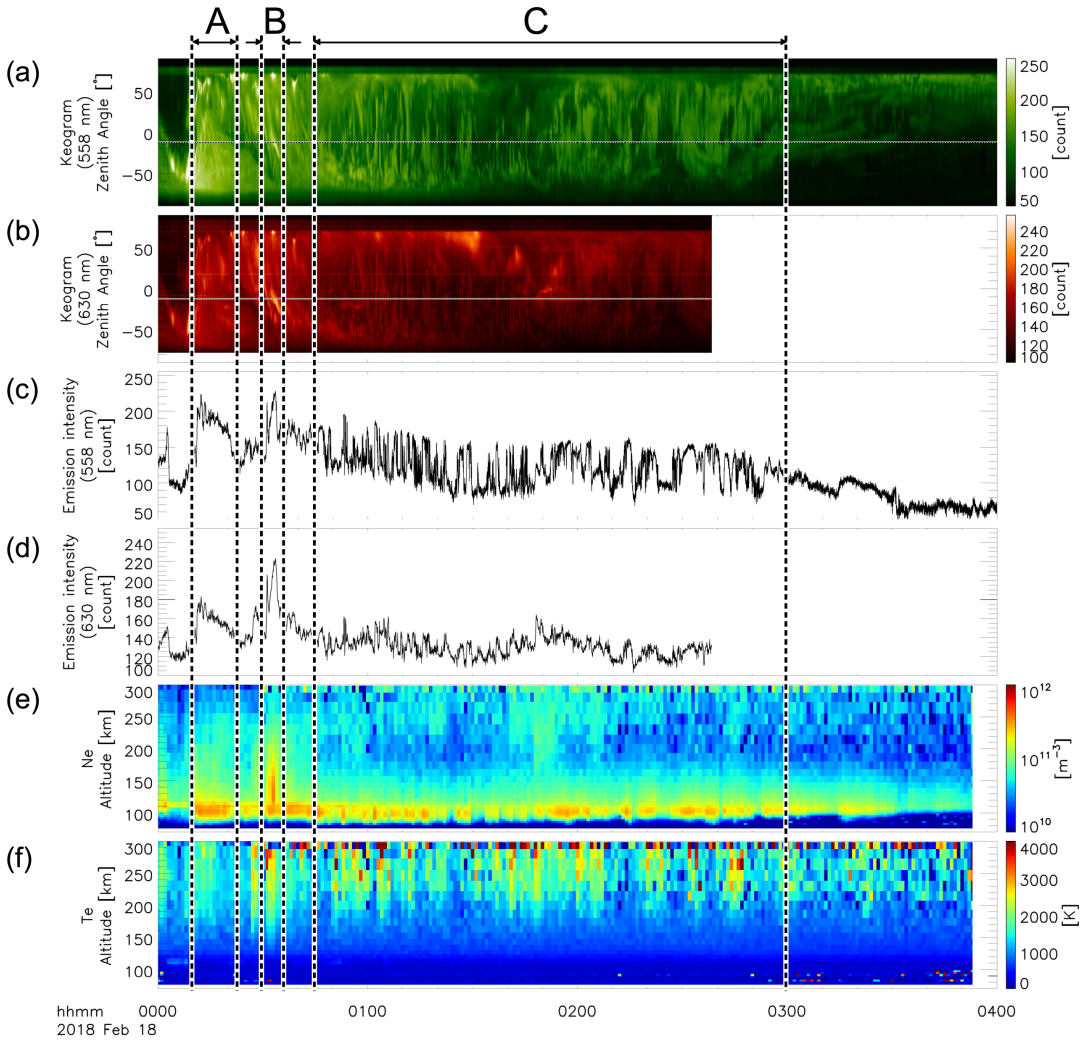

Figure 4.1. Summary plot of Case 1 obtained on February 18, 2018. Keograms for (a) WMI-558 and (b) WMI-630. Horizontal dashed lines in (a) and (b) represent the pixel that corresponds to the EISCAT radar observation point. The emission intensities at the horizontal lines for (c) WMI-558 and (d) WMI-630. (e) electron density and (f) temperature obtained with the EISCAT UHF radar. Three types of aurora (amorphous PsA, auroral streamer, and patchy PsA) were mainly observed in the timespans labeled as A, B, and C.

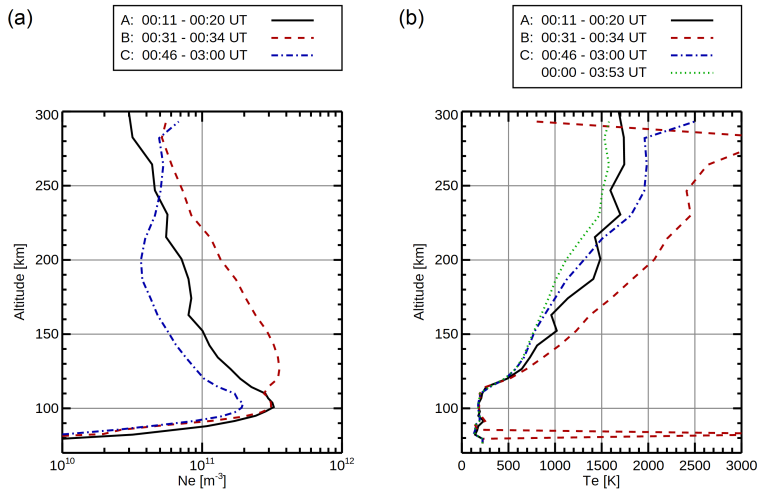

Figure 4.2. Height profiles of (a) electron density and (b) temperature averaged in the timespan shown in Figure 4.1 as A, B, and C.

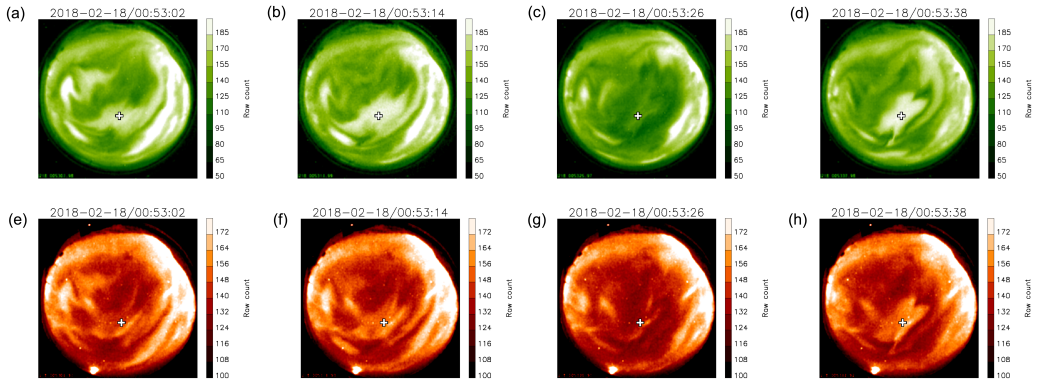

Figure 4.3. A series of auroral images spaced 12-seconds apart obtained by WMI-558 (a–d) and by WMI-630 (e–h) from 00:53:02 to 00:53:38 UT on February 18, 2018.

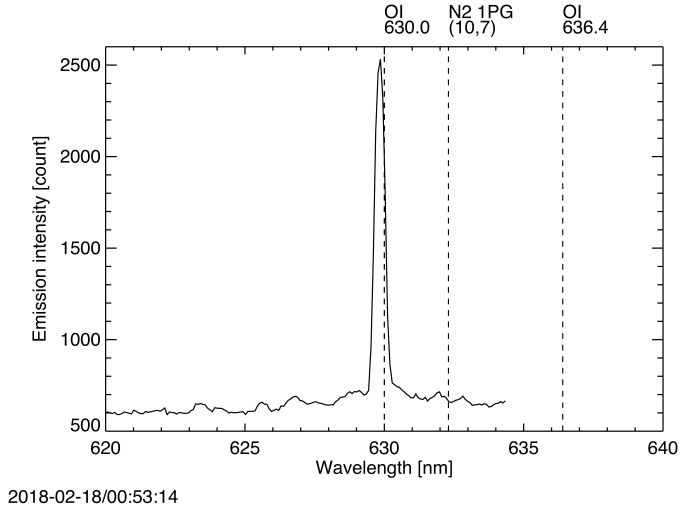

Figure 4.4. Auroral spectrum obtained with the compact optical spectrograph at 00:53:14 UT on February 18, 2018. It should be noted that the exposure time was 29.0 seconds, the wavelength range was 545–635 nm, the resolution was ∼0.4 nm, and the interval was ∼0.1 nm.

of ON–OFF modulation (or main pulsation) might be mainly dominated by N_2 1PG (10,7) (not by OI 630 nm) as suggested by Tsuda *et al*. [2020]. The auroral image data obtained by WMI-630 would not indicate soft electron precipitation in case the WMI-630 data were contaminated by the N_2 1PG (10.7), since the N_2 1PG emission occurs in the *E* region caused by energetic electron precipitation. To evaluate this contamination, we examined the auroral spectrum data simultaneously obtained by a compact optical spectrograph at Tromsø [cf. Oyama *et al*., 2018, Tsuda *et al*., 2020]. The field-of-view was 0.03° in elevation, and 2° in azimuth at the local magnetic zenith. Figure 4.4 indicates the auroral spectrum obtained by the compact optical spectrograph at 00:53:14 UT, when the PsA occurred as shown in Figure 4.3. We confirmed that the 630 nm emission was detected, while the N_2 1PG emission was not seen in the spectrum, thus suggesting the existence of soft electron precipitation (at least as a stable or background component) during the appearance of a PsA. From Figures 4.1d and 4.3e–4.3h, we observe the pulsation of 630 nm aurora: this is controversial since its emission lifetime is 110 s. This OI 630 nm pulsation might be caused at lower altitudes of *F* region as suggested by Liang *et al*. [2016]. Future study is necessary to identify the periodicity of OI 630 nm emission by excluding the N2 1PG (10,7) emission.

4.3.2 Case 2: 23–24 UT on October 27, 2019

Figure 4.5 shows observation data obtained on October 27, 2019, given in the same format as that in Figure 4.1. The EISCAT radar observation was conducted from 23 UT on this day. PsA patches were detected by WMI-558 from 23:00 to 23:40 UT (Figures 4.5a and 4.5c). In the 558 nm all-sky image data from 23:13 to 23:18 UT (D in Figure 4.5), PsA patches were detected at the EISCAT radar observation point,

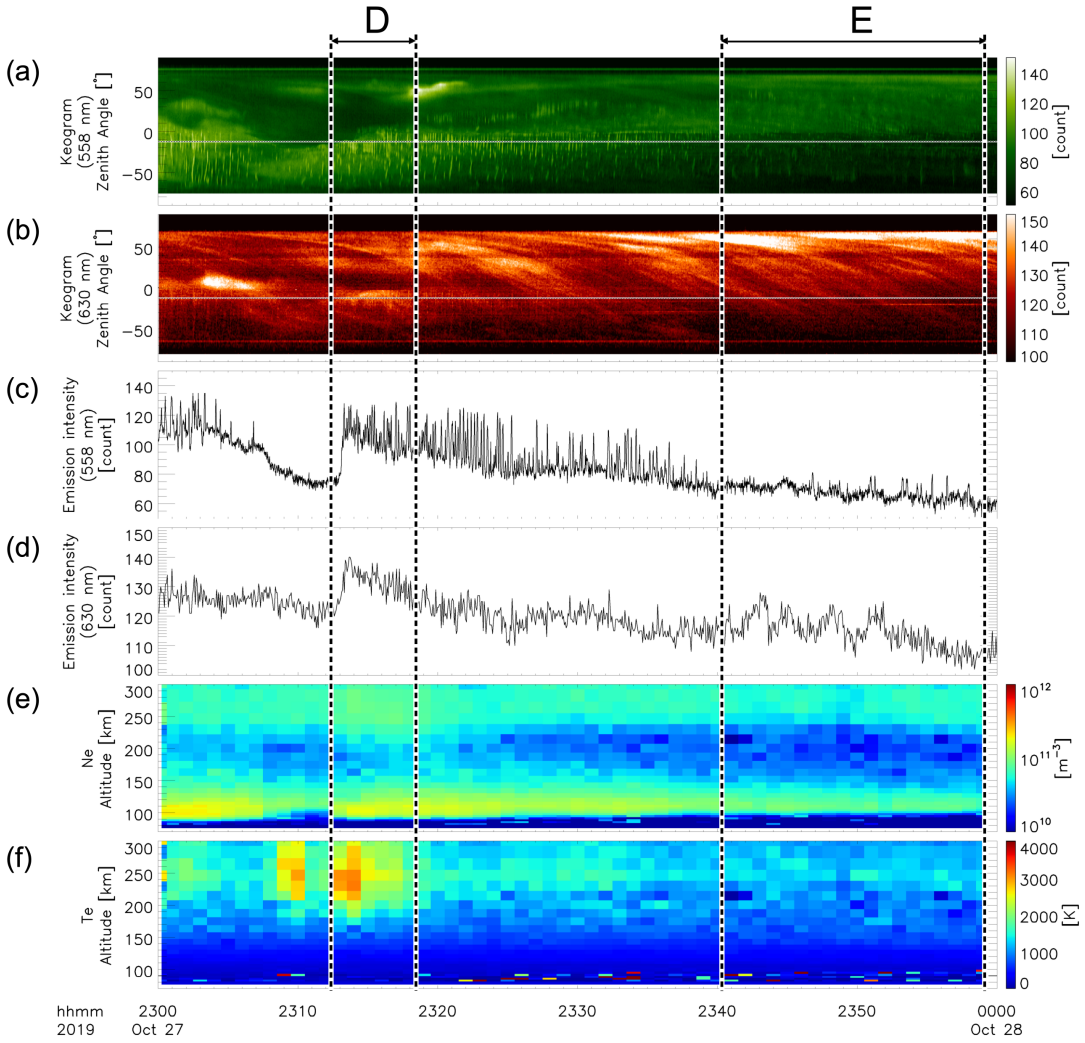

Figure 4.5. Summary plot of Case 2 obtained on October 27, 2019. Keograms for (a) WMI-558 and (b) WMI-630. Emission intensities at the horizontal lines in (a) and (b) for (c) WMI-558 and (d) WMI-630. (e) Electron density and (f) temperature obtained with the EISCAT UHF radar. The electron density had a local peak in the *F* region with PsAs in the timespans labeled as D, and without PsAs in the timespan labeled as E.

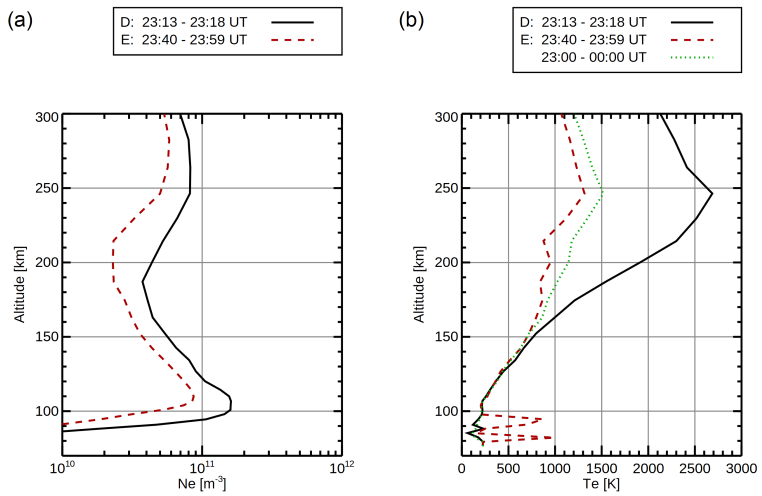

Figure 4.6. Height profiles of (a) electron density and (b) temperature averaged in the timespan shown in Figure 4.5 as D and E.

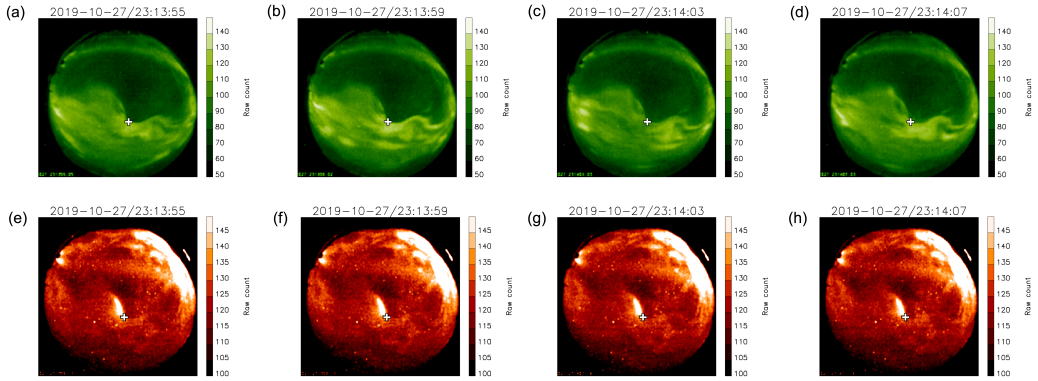

Figure 4.7. A series of auroral images spaced 4-seconds obtained by WMI-558 (a–d) and WMI-630 (e–h) from 23:13:55 to 23:14:07 UT on October 27, 2019.

and, simultaneously, the electron density in the *F* region was slightly enhanced (see Figure 4.5e). Height profiles of the electron density and temperature averaged for the period of D are shown as solid black lines in Figures 4.6a and 4.6b. The electron density enhancement in the *F* region might have been caused by soft electron precipitation, since it was accompanied by both a 630 nm aurora, and an electron temperature enhancement (Figures 4.5b, 4.5d, 4.5f, and 4.6b). Note that the auroral emission was partially covered by clouds, moving from north to south (Figures 4.5a, and 4.5b). Figure 4.7 shows successive auroral images with a time interval of 4 s from 23:13:55 to 23:14:07 UT. The auroral omega band or the torch-like structure can be seen in the auroral images obtained by WMI-558. Regarding the EISCAT observation point, which is indicated by a white plus mark, the 558 nm emission brightened, as shown in Figures 4.7b and 4.7d, whereas the 630 nm emission was somewhat stable. In particular, the latter was enhanced in the eastern part of the omega band or the western part of the torch. We confirmed through the simultaneous spectrograph data that the OI-630.0 nm emission was dominated in the WMI-630 data as shown in Figure 4.8. From

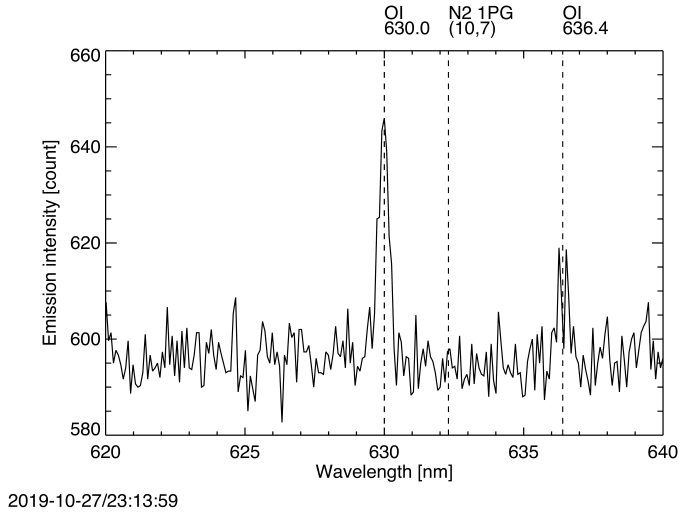

Figure 4.8. Auroral spectrum obtained with the compact optical spectrograph at 23:13:59 UT on October 27, 2019. It should be noted that the exposure time was 0.7 seconds, the wavelength range was 615–705 nm, the resolution was $\sim$0.4 nm, and the interval was $\sim$0.1 nm.

23:40 to 23:59 UT (E in Figure 4.5), the electron density had a peak in the *F* region (Figure 4.5e), whereas PsA patches were not detected at the EISCAT radar observation point (Figures 4.5a and 4.5c). Median height profiles of the electron density and temperature during the period of E are shown as red dashed lines in Figures 4.6a and 4.6b: this *F* region electron density peak might be caused by polar patches, since it was not accompanied by an electron temperature enhancement relative to the background temperature (green dotted line in Figure 4.6b).

4.4 Statistical Results

To understand the quantitative characteristics of the *F* region electron density enhancement associated with PsAs, we carried out statistical analysis using the simultaneous EISCAT UHF radar data and all-sky imager data for 14 nights from September 2016 to December 2019, when PsA patches were seen in WMI-558. The 26-hour data were selected by visual inspection using the quick-look viewer (http://pc115.seg20.nipr.ac.jp/www/AQVN/evs1.html). We examined the electron density data obtained by the EISCAT radar in the following analysis method: first, an all-sky image was smoothed by a moving bin with 5×5 pixels to gain a signal-to-noise ratio. Figure 4.9 shows an example of events used for the statistical analysis. Figure 4.9a shows the keogram created from the smoothed all-sky images on February 18, 2018. The horizontal dashed line in Figure 4.9a represents the EISCAT radar observation point. The 558 nm emission intensity is shown in Figure 4.9b. We conducted a wavelet transform with a time window of 1 min; the calculated power spectrum is given in Figure 4.9c. We excluded the data in the timings shaded in gray in Figure 4.9

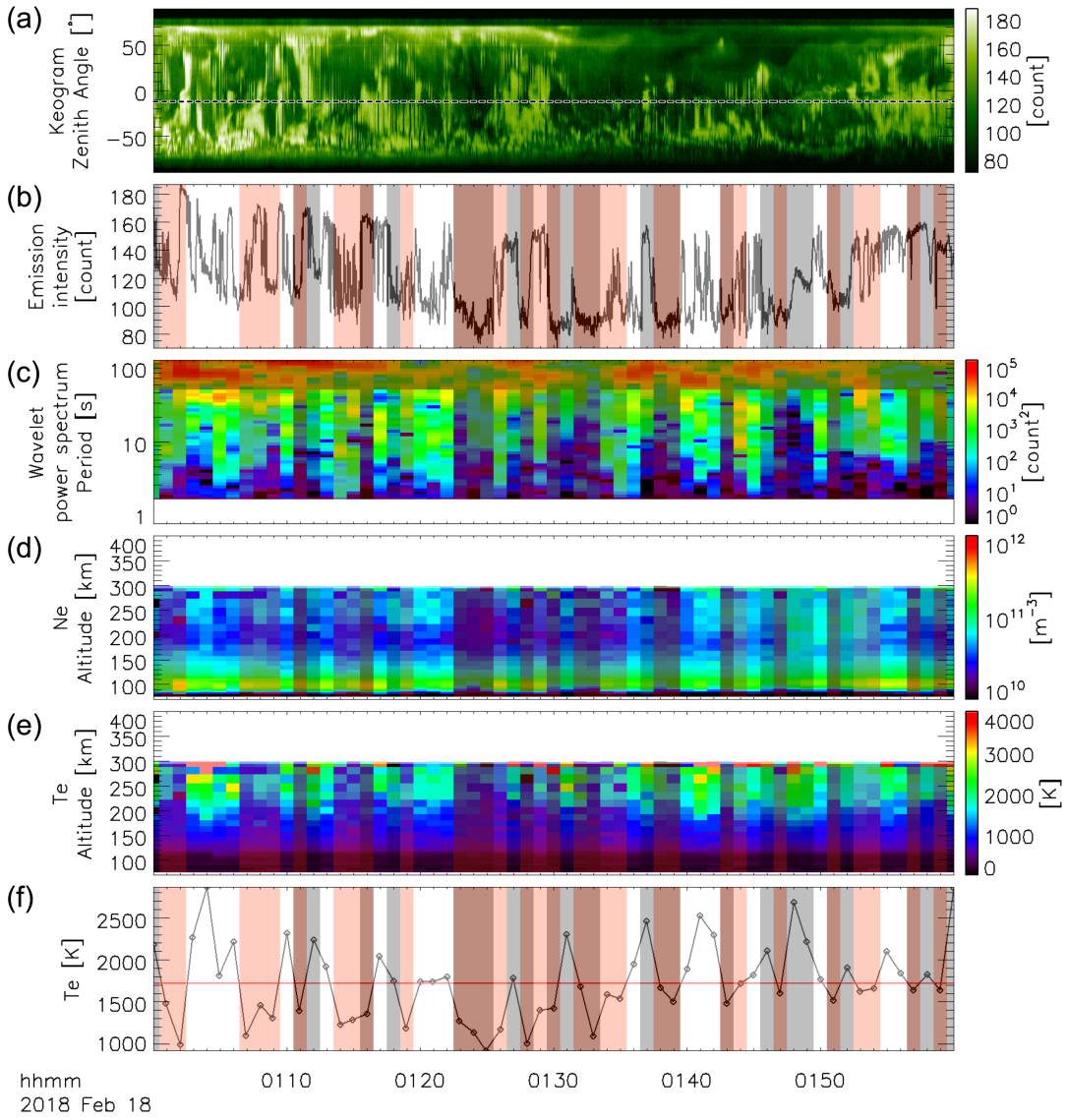

Figure 4.9. An example showing the procedure to extract electron density data during PsAs with electron temperature enhancement. (a) Keogram for WMI-558. (b) Emission intensity at the EISCAT radar observation point (horizontal dashed line in (a)). (c) The wavelet power spectrum of (b). (d) Electron density and (e) temperature. (f) Median electron temperature at 240–270 km altitude (black diamond and line) and its median value during an hour (red line). Gray and red shades are explained in the text.

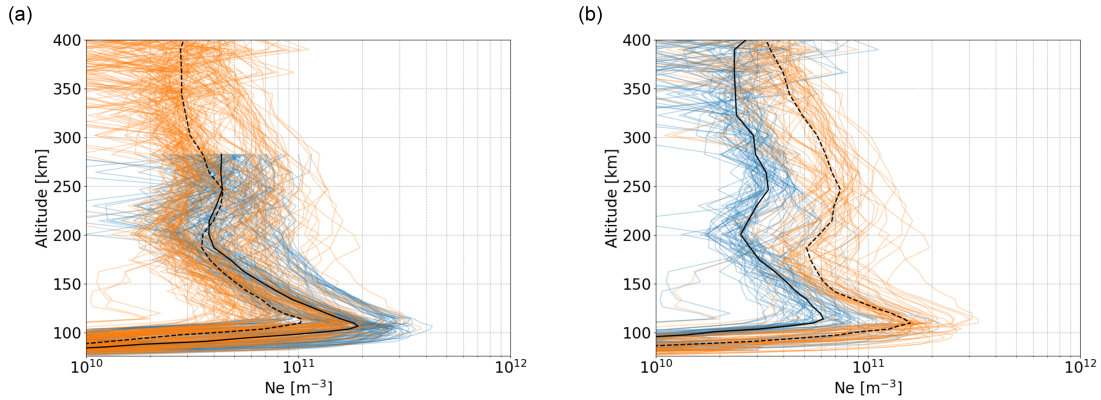

Figure 4.10. (a) Electron density height profiles extracted through the procedure explained in Figure 4.9 for two observation modes of the EISCAT radar: one covered the altitude range from 76 to 282 km (blue lines), the other a higher altitude range, from 76 to 647 km (orange lines). Each median profile is shown by a solid black or dashed line. (b) Electron density height profiles which had two peaks in the *E* and *F* regions: they are divided into a weak ($\leq 5 \times 10^{10}$ m^{-3}) ionization one (blue lines) and a strong ($> 5 \times 10^{10}$ m^{-3}) ionization one (orange lines) at an altitude of 247 km. Each median profile is shown by a solid black or dashed line.

when the wavelet power in the period range from 2 to 40 s was smaller than that of the red-noise level, with a confidence interval of 95% [Torrence and Compo, 1998], since this period range corresponds to a typical PsA period. The red noise was defined to be $x(t) = rx(t-1) + \sigma\varepsilon(t)$, where $x(t)$ is the value of variable x at time t, r is the lag 1 autocorrelation coefficient, σ is the standard deviation, and $\varepsilon(t)$ is the white noise function with the variance 1. Furthermore, we excluded data in the timings shaded in red, when the median electron temperature in the 240–270 km altitude range (black diamond and line in Figure 4.9f) was lower than its median value for an hour (red line in Figure 4.9f) to remove the influence of the electron density enhancement by polar patches. Additionally, we excluded data when the local shadow height had an altitude of less than 400 km, in order to remove the influence of the electron density enhancement by sunlight. Hence, we carefully selected the periods when PsA was observed by the EISCAT radar and all-sky imagers without the effects of polar patches and sunlit conditions, as indicated by the unshaded timings in Figure 4.9d. Figure 4.10 shows 272 electron density profiles extracted from the EISCAT data for 26 hours, with a temporal resolution of 1 min, using the procedure explained above. There were two observation modes of the EISCAT radar during this period: one covered the altitude range from 76 to 282 km (short mode), and is related to 124 profiles, as indicated by blue lines; the other covered a higher altitude range, from 76 to 647 km (long mode), and is related to 148 profiles, as indicated by orange lines. The median profile for each mode is shown by a solid black or dashed line. Focusing on the *F* region electron density obtained with the long mode, the median profile showed local maximums at two altitudes: 1.06×10^{11} m^{-3} at 114 km and 4.42×10^{10} m^{-3} at 247 km. Furthermore, we observe the local minimum with 3.51×10^{10} m^{-3} at 187 km. Moreover, the electron density estimated from the EISCAT data covering 76–282 km

tended to increase as well in the *F* region, although it seems difficult to identify the maximum of the electron density because of the data coverage obtained with the short mode. Noteworthily, the electron height profile exhibited a double-peak structure, and, therefore, we identified the profiles with double peaks with a local minimum between them: we found that 112 (76%) out of the 148 profiles covering 76–647 km had such double peaks, thus suggesting that a PsA is accompanied by soft electron precipitation in most cases. We divided the 112 profiles with double peaks into two: one with a weak ($\leq 5 \times 10^{10}$ m^{-3}) ionization (blue lines in Figure 4.10b), the other with a strong ($> 5 \times 10^{10}$ m^{-3}) ionization (orange lines in Figure 4.10b) at an altitude of 247 km. The median profile for each case is shown by a solid black or dashed line. The numbers of profiles that had weak and strong *F* region ionization were 59 and 53, respectively. When the ionization in the *F* region was strong, the ionization in the *E* region was also strong. Figure 4.11a shows the MLT distribution of the electron density profiles generated by sorting all 272 profiles in MLT. Figure 4.11b shows their hourly median distribution produced by allocating 1 h time slots, as in Figure 4.11a. Figure 4.11c shows the occurrence rate of double peaks (red dots and line) and the number of samples (blue dots and line) in 1 h time slots. We note that the occurrence of double peaks exceeded 80% in the 22–3 MLT range. The peak of electron densities in the *F* region was not clear after 3 MLT.

4.5 Brief Summary and Discussion

We showed case studies for two events and statistical analysis for 14 events using data simultaneously obtained with the EISCAT UHF radar and auroral imagers at 558 and 630 nm, in order to elucidate how often a PsA is accompanied by soft electron precipitation. We explained that the electron density in the ionospheric *F* region was enhanced associated with PsAs: this is expected to be caused by the soft electron precipitation, since the electron temperature was also enhanced. From the statistical analysis, we found that 76% of electron density profiles had a double-peak structure with local enhancements in the ionospheric *E* ($\sim$110 km) and *F* ($\sim$250 km) regions.

Here, using the global airglow (GLOW) model [Solomon *et al*., 1988], we estimated height profiles of the ionization rate produced by the isotropic Maxwellian electrons, with a total energy flux of 1 erg cm^{-2} s^{-1}, and characteristic energies in the range from 100 eV to 10 keV (Figure 4.12). The selected location and time is Tromsø and 1 UT on February 18, 2018, respectively. The GLOW model is available at http://download.hao.ucar.edu/pub/stans/glow. It is clear from Figure 4.12 that the local enhancements at $\sim$110 and $\sim$250 km altitude could be caused by the electron precipitation with energies of 10 keV and $<$100 eV, respectively, supposing that the electron density enhancement has been caused by the electron precipitation. It is reasonable that the upper atmospheric dynamics, such as ambipolar diffusion, have not been considered in this study, since the target was limited in the *E* and lower-*F* regions. From the electron height profile data for the 112 events when the double peak was observed, combined with the relationship between the precipitating electron energy and the ionization peak height, we estimated the electron energy

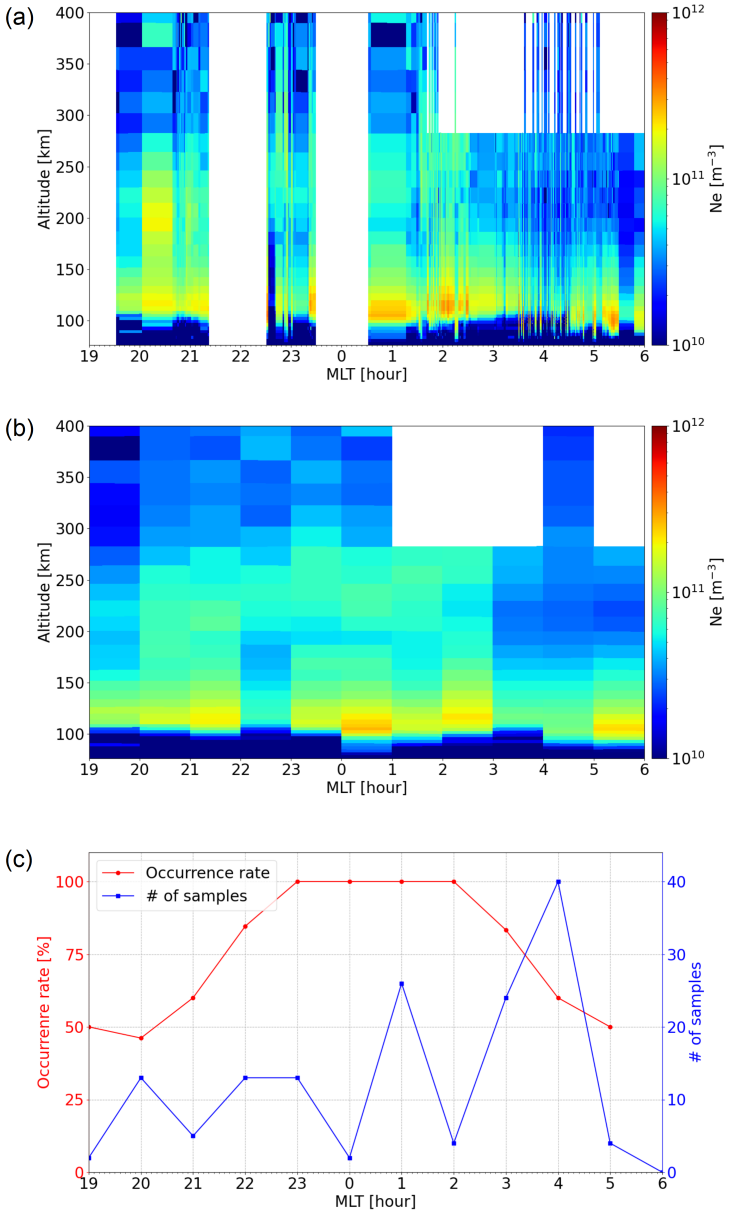

Figure 4.11. (a) MLT distribution of the extracted 272 electron density height profiles. (b) Their median distribution during an hour. (c) The occurrence rate that the profile at each MLT had two peaks in the *E* and *F* region (red dot and line) and number of samples (blue dot and line).

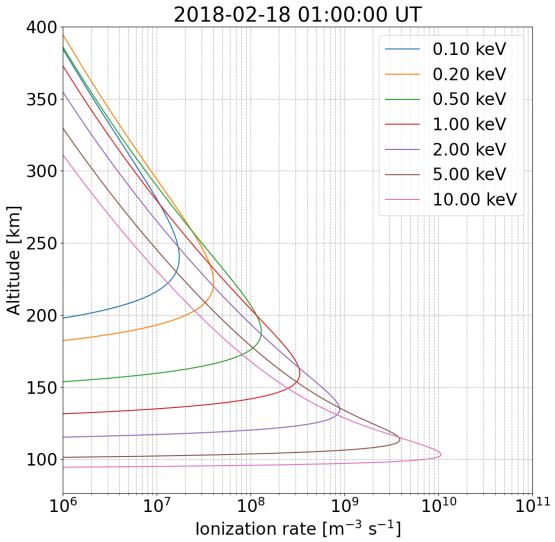

Figure 4.12. Ionization rate produced by isotropic Maxwellian electrons of total energy flux of 1 erg cm^{-2} s^{-1} and characteristic energies from 100 eV to 10 keV, using the GLOW model.

for each peak altitude: we sorted these electron energy values into seven energy bins of 0.1, 0.2, 0.5, 1, 2, 5, and 10 keV. Figure 4.13 shows the occurrence rate histogram of precipitating electron energies estimated for the *E* (blue bars) and the *F* region peaks (orange bars). From these results, we suggest that 86% of the *E* region peaks were caused by precipitating electrons in the energy range from 500 eV to 5 keV, whereas 89% of the *F* region peaks were caused by precipitating electrons in the energy range below 100 eV. This is consistent with Tesema *et al*. [2020a], who showed that precipitating electrons had a low-energy peak at approximately 0.03–1 keV, besides a high-energy peak at ∼10 keV.

The electron density enhancement in the *E* region in PsAs is caused by precipitating electrons in the energy range from a few to tens of keV. Previous studies showed that this relatively high-energy electron precipitation is generated by the pitch angle scattering with LBC waves near the magnetic equator [Kasahara *et al*., 2018c]: these cannot produce the enhancement of electron density peaked in the *F* region. We suggest that this enhancement with electron temperature increase would be caused by precipitating electrons with energies lower than 1 keV: these electrons are generated by UBC and/or ECH waves and the backscattered primary and secondary electrons in the opposite hemisphere [Evans *et al*., 1987, Fukizawa *et al*., 2018, 2020, Inan *et al*., 1992, Khazanov *et al*., 2014, 2015a, Miyoshi *et al*., 2015b]. Figure 4.10b indicates that the electron density enhancements in the *E* and *F* regions have a positive correlation: this may imply a positive correlation between each source mechanism or the positive correlation of the UBC, ECH wave amplitude, and secondary electron flux with the LBC wave amplitude.

The hourly-averaged occurrence rate of the *F* region electron density peak exceeded 80% in the 22–3 MLT range (Figure 4.11c). Ni *et al*. [2017] reported that strong (>1.0 mV m^{-1}) ECH waves are frequently excited at the magnetic equator ($|\mathrm{MLAT}| < 3°$) in approximately the same MLT range. By contrast, the

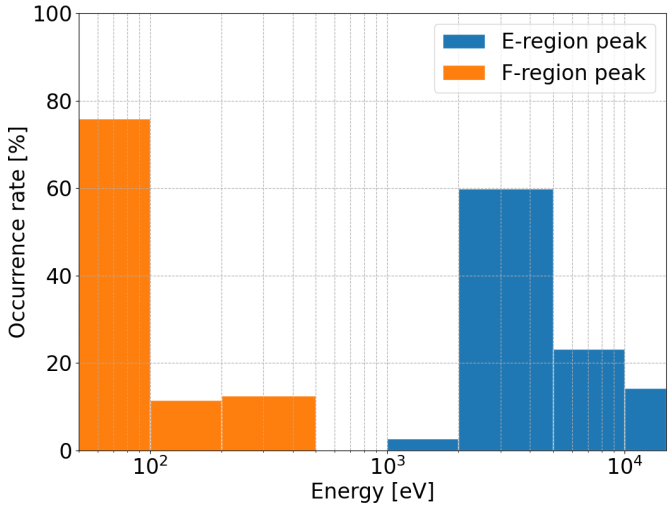

Figure 4.13. Occurrence rate of the E (blue bars) and the F region peaks (orange bars) at the peak altitude of the ionization rate produced by electrons of characteristic energy, shown as the horizontal axis.

UBC wave intensity is strong in a wider range from 20 to 11 MLT [Meredith *et al.*, 2012]. Thus, the appearance of an UBC is not consistent with the result of the occurrence of a F region electron density peak event, showing the decrease of occurrence in the morning sectors after 3 MLT (see Figure 4.11c). Also note that the MLT range where the F region electron density peak occurred is approximately consistent with that of the polar patches observed in Ny-Ålesund, Norway (78.9°N, 12°E; 76°MLAT) [Moen *et al.*, 2007]. Although we set the threshold of electron temperature to remove the influence of electron density enhancement by polar patches in the statistical analysis, we have probably not been able to completely remove it. The identification of the generation process of the F region electron density enhancement associated with PsAs will be conducted by coordinated ground-satellite observations in the future.

Statistical results showed that 24% of PsA events was not accompanied by the electron density enhancement in the F region. Samara *et al.* [2015] suggested that the low-energy electron precipitation ($<$ 1 keV) was prevented by upward field-aligned currents caused by parallel potential drops of up to 1 kV associated with strongly and temporally varying PsAs. However, potential drops would not be sufficient to account for the reduction of the low-energy electrons if the field-aligned currents occur at the edges of PsA patches as suggested by [Fujii *et al.*, 1985]. Another possible mechanism to explain PsA events without the F region electron density enhancement is that ECH and UBC waves are not excited in the magnetosphere. These mechanisms are valuable subjects to study in the future.

Recently, it has been reported that precipitating electron energy changes depending on the different types of PsAs [Grono and Donovan, 2018, Tesema *et al.*, 2020b, Yang *et al.*, 2019]. However, we could not distinguish electron density height profiles of different types of PsAs since the temporal resolution of the EISCAT radar was longer than the typical modulation period of PsAs. Three-dimensional ionospheric

observations with higher temporal resolution ($\sim$0.1 s) by EISCAT_3D radar [McCrea *et al*., 2015] are planned in the near future. The difference of electron density profiles during different types of PsAs should be investigated by coordinated EISCAT_3D radar and high-sensitivity camera observations.

One of the unsolved issues for PsAs is what determines their shapes. The low-energy electron precipitation in PsAs, which are suggested in this study, may contribute to a change in the spatial structure of the plasma density or the growth rate of the driver of the PsAs (chorus and ECH waves) in the magnetosphere by the outflowing of the ionospheric plasma into the magnetosphere.

5 Reconstruction of Precipitating Electrons Associated with PsAs [Fukizawa *et al.*, 2022b]

In recent years, auroral observation networks with high-sensitivity cameras have been developed in the high-latitude region: these networks allow us to observe dimmer auroras, such as PsAs, with a high signal-to-noise ratio. In this chapter, we describe the reconstruction of the three-dimensional distribution of the volume emission rate (VER) of the PsA and the horizontal distribution of precipitating electrons using monochromatic PsA images, obtained from three observation points with computed tomography. The characteristic energy of the reconstructed precipitating electron flux ranges from 6 to 23 keV, while the peak altitude of the reconstructed VER ranges from 90 to 104 km. We here evaluate the reconstruction accuracy by comparing results from observed auroral images and from a model aurora. Furthermore, the reconstructed ionospheric electron density is compared with the observed density, which was correctly reconstructed to some extent, even after a decrease in PsA intensity. Basing on the above, we suggest that the horizontal distribution of precipitating electrons associated with PsAs can be effectively reconstructed from ground-based optical observations.

5.1 Background

Energy distribution of precipitating electrons is a key parameter to understand the generation process in the magnetosphere. In general, satellite and rocket observations are required to observe precipitating electrons. On the other hand, the auroral height profile is determined by the energy distribution of precipitating electrons: therefore, the peak altitude and thickness of the auroral emission are useful to estimate the characteristics of precipitating electrons. In past studies, stereoscopic observation through the triangulation method has been applied to investigate the aurora height profile. More in detail, Stenbaek-Nielsen and Hallinan [1979] investigated approximately 300 PsAs using stereoscopic observations, thus finding that altitudes ranged from 83 to 135 km, while the mean altitude is 98.5 km. The mean vertical extent is 0.4 km with $\pm$1.0 RMS km. This thin vertical extent implies that, in this case, PsAs are not caused by collisions between atmosphere and precipitating electrons. Instead, they suggested a new model basing on the fact that the energy is carried by precipitating electrons, but its loss in the atmosphere that causes PsAs is primarily

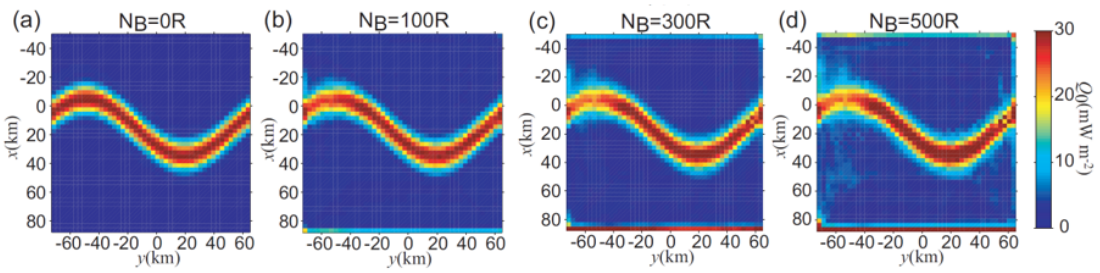

Figure 5.1. The reconstructed total energy flux (Q_0) from five auroral images for noise levels of (a) 0 R, (b) 100 R, (c) 300 R, and (d) 500 R [after Tanaka *et al*., 2011].

through the wave–particle interaction in the ionosphere rather than through direct collisions. However, this mechanism has not been fully elucidated. Jones *et al*. [2009] found that the electron density profile associated with PsAs had a thickness of ∼15–25 km by using the Poker Flat Incoherent Scatter Radar (PFISR) data, suggesting that the thin pulsating patches observed by Stenbaek-Nielsen and Hallinan [1979] are a subset of PsAs.

Computed Tomography (CT) used in clinical medicine has been applied to solar-terrestrial physics since 1990s [e.g., Aso *et al*., 1990, 1993, 1998, Frey *et al*., 1996, Nygrén *et al*., 1997]: this method reconstructs three-dimensional (3-D) structures using a large number of images taken from various directions. On the other hand, the number of ground-based stations is limited for aurora observations. Nevertheless, it has been suggested that an auroral 3-D structure can be sufficiently reconstructed by adding to the CT method relatively weak constraints associated with auroral emission properties [e.g., Aso *et al*., 1998]. Furthermore, Aurora Computed Tomography (ACT) is a technique to retrieve the 3-D luminous structure of aurora from multiple auroral images obtained simultaneously at multipoint stations [e.g., Aso *et al*., 1998]. Additionally, Generalized ACT (G-ACT) has been developed to reconstruct the spatial energy distributions of precipitating electrons from the electron density and cosmic noise absorption (CNA) data, besides monochromatic auroral images taken at multiple stations [Aso *et al*., 2008, Tanaka *et al*., 2011]. The ACT and G-ACT methods have been applied to discrete auroras. Tanaka *et al*. [2011] demonstrated the reconstruction of a discrete aurora through G-ACT using auroral image data obtained by the Auroral Large Imaging System (ALIS), the electron density from the European Incoherent Scatter (EISCAT) radar, and CNA from the Imaging Riometer for Ionospheric Study (IRIS) at Kilpisjärvi. Figure 5.1 shows the reconstructed total energy Q_0 of the precipitating electron flux from five auroral images for various amount of noise levels given in a simulated manner. The reconstruction is accurate regarding low noise (Figures 5.1a and 5.1b). However, underestimation of Q_0 in the western part of the auroral arc and along the northern and southern boundaries of the simulation region occurred as the noise increased (Figures 5.1c and 5.1d). This underestimation has been improved when one of the four southern stations was moved to the north of the aural arc (not shown). Figure 5.2 exhibits the reconstructed differential flux of the incident electrons at the EISCAT

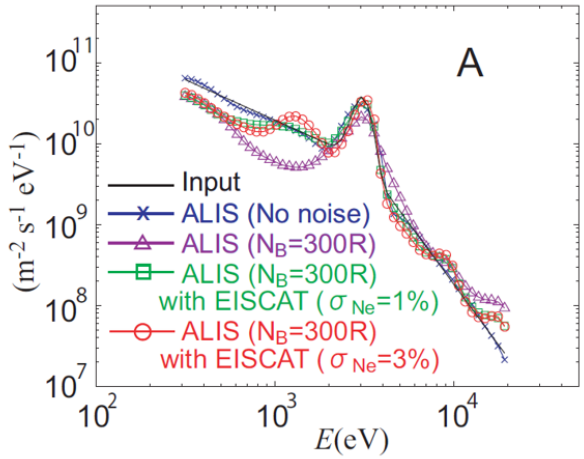

Figure 5.2. The differential flux of the incident electrons reconstructed based only on auroral images with no noise (blue curve) and with a background noise of 300 R (purple curve), and considering both auroral images with a background noise of 300 R and the EISCAT electron density with a Gaussian noise, whose mean value is 0 m^{-3} and standard deviation is 1% (green curve) or 3% (red curve). The black curve represents the differential flux of the original incident electrons [Tanaka *et al*., 2011].

radar observation point. From this figure, the differential flux reconstructed based only on auroral images with a background noise of 300 R (purple curve) is less than the incident flux for energies at and below E_{P}, and greater than the incident flux for energies above E_{P}, where E_{P} is the peak energy. By using the electron density obtained by the EISCAT radar (green and red curves), it is obvious that the underestimation and overestimation of the differential flux have been significantly corrected. The improvement of the reconstruction is limited to energies greater than 700 eV, since the electron density above a 170-km altitude was used for the inversion.

The application of ACT and G-ACT methods to PsAs is rather difficult, and has not been reported since the PsA intensity is dimmer than that of a typical discrete aurora (several hundreds of Rayleigh ' s up to tens of kR at 557.7 nm; a few hundred Rayleigh ' s to ∼10 kR at 427.8 nm) [McEwen *et al*., 1981]. However, remote operation of many high-sensitivity cameras via internet and an archive system capable of storing a huge amount of aurora data make it possible to observe PsA events with high signal-to-noise ratio and simultaneously with high temporal resolution at multiple observation points. The Magnetosphere Ionosphere Radars All-sky Cameras Large Experiment (MIRACLE) network consists of nine all-sky cameras (ASCs), located in Fennoscandian Peninsula. Two ASCs with intensified charge-coupled device (ICCD) have been replaced with a new camera with an electron-multiplying CCD (EMCCD) in 2007: such cameras are more suitable for measuring rather faint auroral structures like PsAs [Sangalli *et al*., 2011]. In addition, as described in Subsection 4.2.1, Ogawa *et al*. [2020] developed a low-cost multiwavelength imaging system for aurora and airglow studies, called WMI, and installed it at several locations in the north and south polar regions. In this study, we attempt to reconstruct for the first time the 3-D VER of PsAs and the horizontal distribution of precipitating electrons using data obtained by these high-sensitivity cameras by applying the

ACT methods.

5.2 Data and Method

5.2.1 Auroral Images

During the substorm recovery phase from 0 to 2 UT on February 18, 2018, PsA patches were observed by MIRACLE ASCs at Kilpisjärvi (KIL, 69.05°N, 20.36°E), Abisko (ABK, 68.36°N, 18.82°E), and WMIs in Skibotn (SKB, 69.35°N, 18.82°E). These ASCs have common field-of-view, as shown in Figure 5.3b. The location of Tromsø (TRO, 69.58°N, 19.23°E), where the EISCAT radar is operative, is shown. Figure 5.3a shows 427.8-nm auroral images obtained by the three ASCs from 00:53:30 to 00:53:42 UT. We se-

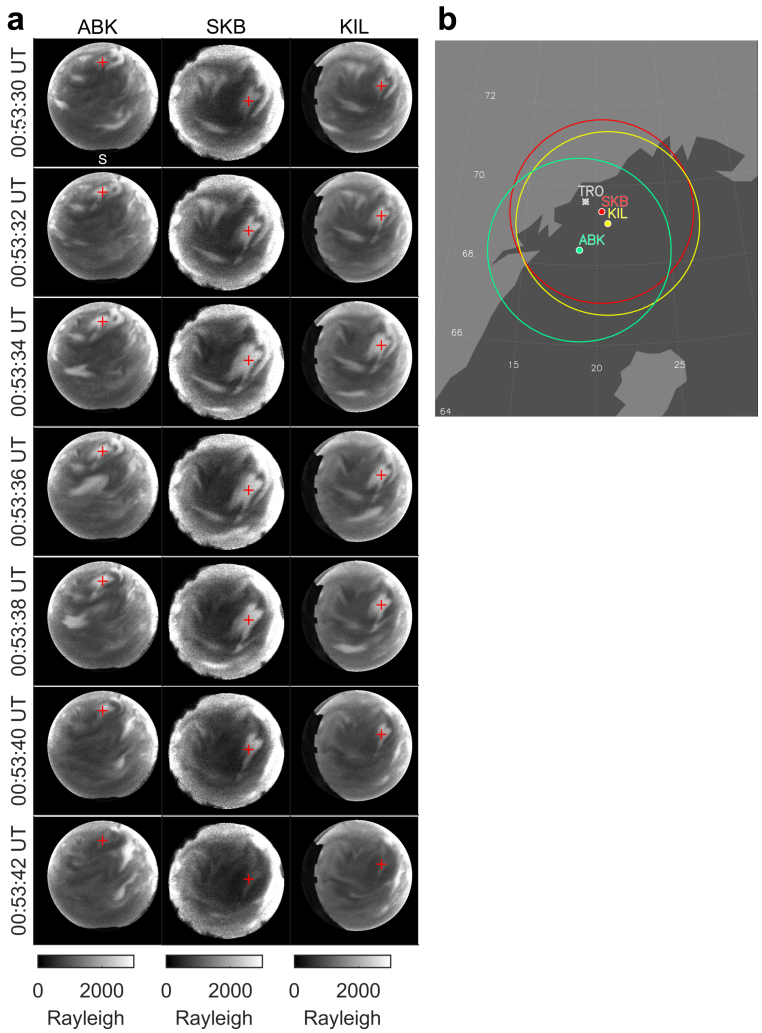

Figure 5.3. (a) Successive auroral images obtained by MIRACLE ASCs at Abisko (ABK), Kilpisjärvi (KIL), and WMIs at Skibotn (SKB) from 00:53:30 UT to 00:53:42 UT on February 18, 2018. (b) Locations and field of views of all-sky cameras at ABK (green), SKB (red), and KIL (blue) at a 100 km altitude. The location of Tromsø (TRO) is shown by a white asterisk.

lected these auroral images since PsA patches have been detected at the EISCAT radar observation point. Comparison between the reconstruction results with the electron density obtained by the EISCAT radar is described in Subsection 5.3.4. The temporal resolution of both MIRACLE ASCs and WMIs was 2 s. The original image has 512×512 and 640×480 pixels for MIRACLE ASCs and WMIs, respectively. A median filter of 3×3 pixels was applied to all auroral images. The signal-to-noise ratio of auroral images obtained with the WMIs is lower than that obtained with the MIRACLE ASCs. To gain the signal-to-noise ratio of the auroral image obtained with the WMIs, we composited auroral images at 427.8 nm simultaneously obtained by four WMIs at SKB. The auroral images taken by four WMIs at SKB had a time ambiguity of $\sim$1–2 s. We determined the timing of auroral images of WMIs by comparing with the temporal changes in the PsA patch observed at ABK and KIL.

5.2.2 Reconstruction Region

We reconstructed the energy and spatial distribution of precipitating electrons and the 3-D distribution of VER of PsA patches, as shown in Figure 5.3a. The ACT method used in this study is based on Tanaka *et al*. [2011]. More in detail, we adopted an oblique coordinate system with the origin (O) at coordinates of (69.4°N, 19.2°E), the x-axis antiparallel to the horizontal component of the geomagnetic field, Y-axis eastward, and the z-axis antiparallel to the geomagnetic field and perpendicular to the y-axis (Figure 5.4). The simulation region was from -75 to 75 km, from -100 to 100 km, and from 80 to 180 km for the x-, y-, and z-axes, respectively. We set the energy (E) range to extend from 300 eV to 100 keV. This region was divided linearly into $n_x \times n_y \times n_z$ voxels along x-, y-, and z-axes, and logarithmically into n_E bins in the energy. We set the parameters (n_x, n_y, n_z, n_E) to (75, 100, 50, 50), corresponding to a spatial mesh size as $2 \times 2 \times 2$ km. These parameters were selected so that each voxel has at least one line-of-sight crossing from the pixels in the auroral images.

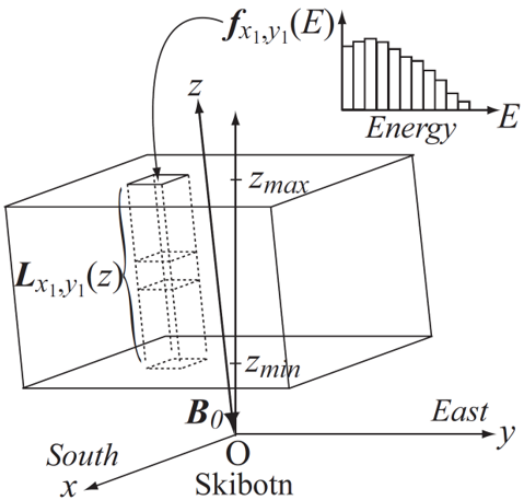

Figure 5.4. Schematic illustration of coordinate systems used in ACT [Tanaka *et al*., 2011]. $\mathbf{B}_0$ is the directional vector of the geomagnetic field.

5.2.3 Forward Problem

Incident electrons at a location (x_1, y_1, z_{max}) cause auroral emission in the voxels below z_{max} along a field line. A vector $\mathbf{f}_{x_1,y_1}(E) = \{f_i | i = 1, 2, ..., n_E\}$ $[\mathrm{m}^{-2}\mathrm{s}^{-1}\mathrm{eV}^{-1}]$ and $\mathbf{L}_{x_1,y_1}(z) = \{L_i | i = 1, 2, ..., n_z\}$ $[\mathrm{m}^{-3}\mathrm{s}^{-1}]$ are defined for the differential flux of the incident electrons at (x_1, y_1, z_{max}), where f_i is the differential flux in energy between E_i and $E_i + \Delta E_i$, and L_i is the 427.8-nm VER at the altitude between z_i and $z_i + \Delta z_i$. The relation between $\mathbf{f}_{x_1,y_1}(E)$ and $\mathbf{L}_{x_1,y_1}(z)$ is given by

$$\mathbf{L}_{x_1,y_1} = \mathbf{m}\mathbf{f}_{x_1,y_1}, \tag{5.1}$$

where $\mathbf{m}$ is a $n_z \times n_E$ matrix for calculating $\mathbf{L}_{x_1,y_1}(z)$ from $\mathbf{f}_{x_1,y_1}(E)$ and is described in detail in the Appendix of Tanaka *et al*. [2011]. If $\mathbf{m}$ is independent of x_1 and y_1, Eq. 5.1 can be expanded in the x- and y-directions as follows:

$$\begin{pmatrix} \mathbf{L}_{1,1} \\ \mathbf{L}_{1,2} \\ \vdots \\ \mathbf{L}_{n_x,n_y} \end{pmatrix} = \begin{pmatrix} \mathbf{m} & 0 & \dots & 0 \\ 0 & \mathbf{m} & \ddots & 0 \\ \vdots & \ddots & \ddots & 0 \\ 0 & \dots & 0 & \mathbf{m} \end{pmatrix} \begin{pmatrix} \mathbf{f}_{1,1} \\ \mathbf{f}_{1,2} \\ \vdots \\ \mathbf{f}_{n_x,n_y} \end{pmatrix}, \tag{5.2}$$

$$\mathbf{L} = \mathbf{M}\mathbf{f}, \tag{5.3}$$

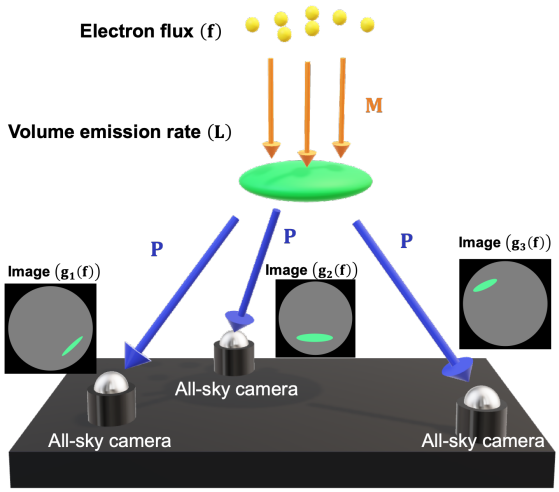

Figure 5.5. Schematic illustration of the forward problem.

where $\mathbf{f}(x, y, E) = \{f_i | i = 1, 2, ..., n\}$ and $\mathbf{L}(x, y, z) = \{L_i | i = 1, 2, ..., m\}$ with $n = n_E \times n_x \times n_y$ and $m = n_z \times n_x \times n_y$. $\mathbf{M}$ is a large sparse matrix defined by

$$\mathbf{M} = \begin{pmatrix} \mathbf{m} & 0 & \dots & 0 \\ 0 & \mathbf{m} & \ddots & 0 \\ \vdots & \ddots & \ddots & 0 \\ 0 & \dots & 0 & \mathbf{m}. \end{pmatrix} \tag{5.4}$$

A gray level g_i $[\mathrm{photons m^{-2} s^{-1} sr^{-1}}]$ at a pixel i in the auroral images is approximated by a linear integration along a line of sight and expressed as follows:

$$g_i = \frac{c_g(\theta, \varphi)}{4\pi} \int L(r, \theta, \varphi) dr, \tag{5.5}$$

where (r, θ, φ) are polar coordinates whose origin is located at the center of the camera lens, and $c_g(\theta, \varphi)$ is a sensitivity and vignetting factor [Aso *et al.*, 1990]. The gray level indicates the brightness of a pixel. Eq. 5.5 is expressed by the matrix operation:

$$\mathbf{g}(\mathbf{f}) = \mathbf{PL} = \mathbf{PMf}, \tag{5.6}$$

where $\mathbf{g} = \{g_i | i = 1, 2, ..., l_g\}$ is a gray-level vector, whose length is l_g, and $\mathbf{P}$ is a $l_g \times m$ matrix used to calculate $\mathbf{g}$ by integrating $\mathbf{L}$ in Eq. 5.3 along the line of sight, and includes the sensitivity and vignetting factors. Schematic illustration of the forward problem is shown in Figure 5.5.

5.2.4 Inverse Problem

The inverse problem is based on the Bayesian model, and is formulated as a problem of maximization of posterior probability. According to Bayes' theorem, the posterior probability $P(\mathbf{f}|\tilde{\mathbf{g}})$, which is the probability that model $\mathbf{f}$ is true given observational data $\tilde{\mathbf{g}}$, is expressed by:

$$P(\mathbf{f}|\tilde{\mathbf{g}}) \quad = \quad \frac{P(\tilde{\mathbf{g}}|\mathbf{f})P(\mathbf{f})}{P(\tilde{\mathbf{g}})} \propto P(\tilde{\mathbf{g}}|\mathbf{f})P(\mathbf{f}), \tag{5.7}$$

where $P(\tilde{\mathbf{g}}|\mathbf{f})$ is the probability of observing data $\tilde{\mathbf{g}}$ given model $\mathbf{f}$, $P(\mathbf{f})$ is the prior probability of model $\mathbf{f}$, $P(\tilde{\mathbf{g}})$ is the marginal probability of $\tilde{\mathbf{g}}$.

For the prior probability of $\mathbf{f}$, a smoothness constraint of $\mathbf{f}$ was adopted and given by:

$$P(\mathbf{f}) \propto \exp\left(-\frac{||\nabla^2\mathbf{f}||^2}{2\sigma^2}\right), \tag{5.8}$$

where σ^2 is the variance of $\nabla^2\mathbf{f}$, and the second-order derivative of $\mathbf{f}$ is taken with respect to x, y, and E. Assuming that data $\tilde{\mathbf{g}}$ has Gaussian errors, the likelihood is expressed by:

$$P(\tilde{\mathbf{g}}|\mathbf{f}) \propto \exp\left\{-\frac{1}{2}\left(\tilde{\mathbf{g}}-\mathbf{g}(\mathbf{f})\right)^T \mathbf{\Sigma}^{-1}\left(\tilde{\mathbf{g}}-\mathbf{g}(\mathbf{f})\right)\right\}, \tag{5.9}$$

where $\mathbf{\Sigma}^{-1}$ is the inverse covariance matrix, and $\mathbf{g}(\mathbf{f})$ is given by Eq. 5.6. We determined Σ^{-1} as the standard deviation calculated from each auroral image. The 32×32 pixel region in which no PsA patch was contained was used to calculate Σ^{-1}.

By substituting Eqs. 5.8 and 5.9 into Eq. 5.7, $P(\mathbf{f}|\tilde{\mathbf{g}})$ is given by

$$P(\mathbf{f}|\tilde{\mathbf{g}}) \propto \exp\left[-\frac{1}{2}\left\{\left(\tilde{\mathbf{g}}-\mathbf{g}(\mathbf{f})\right)^T \mathbf{\Sigma}^{-1}\left(\tilde{\mathbf{g}}-\mathbf{g}(\mathbf{f})\right) + \frac{\left|\left|\nabla^2\mathbf{f}\right|\right|^2}{\sigma^2}\right\}\right]. \tag{5.10}$$

To maximize the posterior probability, it is necessary to minimize the function:

$$\begin{aligned}\varphi(\mathbf{f};\lambda,\lambda_E,c_j) = &\sum_j \left(c_j\tilde{\mathbf{g}}_j-\mathbf{g}_j(\mathbf{f})\right)^T \mathbf{\Sigma}_j^{-1}\left(c_j\tilde{\mathbf{g}}_j-\mathbf{g}_j(\mathbf{f})\right) \\ &+\lambda^2\left|\left|\nabla^2_{x,y}\mathbf{f}+\lambda_E^2\nabla^2_E\mathbf{f}\right|\right|^2,\end{aligned} \tag{5.11}$$

where λ, λ_E , and c_j are the so-called hyperparameters, which are constant corresponding to the weighting factors for the spatial (λ) and energy (λ_E) derivative terms, and the correction factors for the relative sensitivity between cameras (c_j), respectively. The subscript j signifies the three observation points (ABK, KIL, and SKB). The parameter c_{SKB} was fixed at 1. The summation was conducted for the first term in Eq. (2) since c_j and Σ_j^{-1} were different during the three ASCs.

To take advantage of the nonnegative constraint of the differential flux $\mathbf{f}$ (i.e., $\mathbf{f} \geq 0$), a change of variables, $\mathbf{f} = \exp(\mathbf{x})$ was carried out. Then, $\min[\varphi(\mathbf{x};\lambda,\lambda_E,c_j)]$ is a nonlinear least squares problem with respect to $\mathbf{x}$. We solved this problem by the Gauss–Newton algorithm.

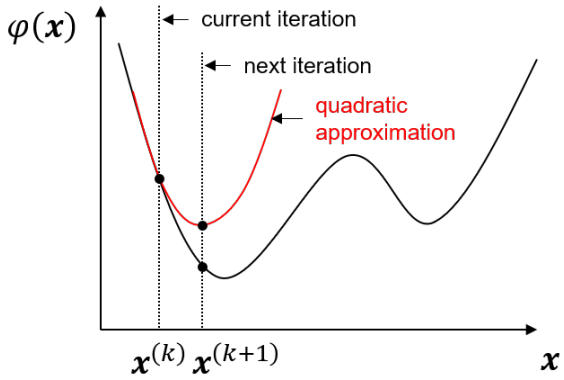

Figure 5.6. Schematic illustration of the Newton method.

The Gauss–Newton algorithm is a modification of Newton's method for finding a minimum of a function. Newton's method attempts to solve the minimization problem $\min[\varphi(\mathbf{x};\lambda,\lambda_E,c_j)]$ by constructing a sequence $\{\mathbf{x}^{(k)}\}$ from an initial guess $\mathbf{x}^{(0)}$ that converses toward a minimizer of φ by using a sequence of second-order Taylor approximations of φ around the iterates. The second-order Taylor expansion of φ around $\mathbf{x}^{(k)}$ is

$$\varphi(\mathbf{x}^{(k)}+\Delta\mathbf{x}) \approx \varphi(\mathbf{x}^{(k)}) + \mathbf{k}(\mathbf{x}^{(k)})\Delta\mathbf{x}^{(k)} + \frac{1}{2}\mathbf{H}(\mathbf{x}^{(k)})(\Delta\mathbf{x}^{(k)})^2, \tag{5.12}$$

where $\mathbf{k}$ is the gradient vector of φ, and $\mathbf{H}$ is the Hessian matrix of φ. The next iteration $\mathbf{x}^{(k+1)}$ is defined to minimize this quadratic approximation in $\Delta\mathbf{x}^{(k)}$ (Figure 5.6) where:

$$\mathbf{x}^{(k+1)} = \mathbf{x}^{(k)} + \Delta\mathbf{x}^{(k)}. \tag{5.13}$$

If the Hessian matrix is positive, the quadratic approximation is a convex function of $\Delta\mathbf{x}^{(k)}$, and its minimum can be found by setting the derivative to zero:

$$\mathbf{k} + \mathbf{H}\Delta\mathbf{x}^{(k)} = 0. \tag{5.14}$$

From Eq. 5.14, the minimum is achieved for

$$\Delta\mathbf{x}^{(k)} = -\mathbf{H}^{-1}\mathbf{k}. \tag{5.15}$$

Since $\varphi = ||\mathbf{r}(\mathbf{x};\lambda,\lambda_E,c_j)||^2 = \sum_j r_j^2$, the gradient is given by

$$k_i = 2\sum_j r_j \frac{\partial r_j}{\partial x_i}. \tag{5.16}$$

Elements of the Hessian matrix are calculated by differentiating the gradient elements g_i with respect to x_k:

$$H_{ik} = 2\sum_j \left(\frac{\partial r_j}{x_i}\frac{\partial r_j}{\partial x_k} + r_j \frac{\partial^2 r_j}{\partial x_i \partial x_k} \right). \tag{5.17}$$

The Gauss–Newton method is obtained by ignoring the second-order derivative terms (the second term in Eq. 5.17). Then, the Hessian matrix is approximated by:

$$H_{ik} \approx 2 \sum_j J_{ji} J_{jk}, \tag{5.18}$$

where $J_{ji} = \partial r_j / \partial x_i$ are entries of the Jacobian matrix $\mathbf{J}$ of $\mathbf{r}(\mathbf{x})$ with respect to $\mathbf{x}$. The gradient and the approximated Hessian can be written in matrix notation as:

$$\mathbf{k} = 2\mathbf{J}^{\mathrm{T}}\mathbf{r}, \tag{5.19}$$

$$\mathbf{H} \approx 2\mathbf{J}^{\mathrm{T}}\mathbf{J}. \tag{5.20}$$

Here, T represents transpose of matrix. By substituting Eqs. 5.19 and 5.20 into Eq. 5.15 we obtained:

$$(\mathbf{J}^{\mathrm{T}}\mathbf{J})\Delta\mathbf{x}^{(k)} = -\mathbf{J}^{\mathrm{T}}\mathbf{r}(\mathbf{x}^{(k)}), \tag{5.21}$$

which is a normal equation with a large sparse matrix. We solved Eq. 5.21 by the Conjugate Gradient Normal Residual (CGNR) method [e.g., Barrett *et al*., 1994, Hestenes and Stiefel, 1952]. Eq. 5.21 can be written as:

$$\mathbf{A}\mathbf{y} = \mathbf{c}, \tag{5.22}$$

where $\mathbf{A} = \mathbf{J}^{\mathrm{T}}\mathbf{J}$,$\mathbf{y} = \Delta\mathbf{x}$, and $\mathbf{c} = -\mathbf{J}^{\mathrm{T}}\mathbf{r}$. The solution x^* of Eq. 5.22 can be expressed as:

$$x^* = \sum_i \alpha_i \mathbf{p}_i, \tag{5.23}$$

where $\mathbf{P} = \{p_1, p_2, ..., p_n\}$ is a set of mutually conjugate vectors with respect to $\mathbf{A}$. The procedure of the CGNR algorithm is explained as follows.

1. Set initial values $\mathbf{t}^{(0)} = \mathbf{c} - \mathbf{A}\mathbf{y}^{(0)}$, $\mathbf{p}_0 = \mathbf{q}_0 = \mathbf{A}^*\mathbf{t}^{(0)}$, and $k = 0$.
2. Calculate $\alpha^{(k)} = ||\mathbf{q}^{(k)}||^2 / ||\mathbf{s}^{(k)}||^2$ where $\mathbf{s}^{(k)} = \mathbf{A}\mathbf{p}^{(k)}$.
3. Calculate the next iteration $\mathbf{y}^{(k+1)} = \mathbf{y}^{(k)} + \alpha^{(k)}\mathbf{p}^{(k)}$.
4. Calculate the next residual $\mathbf{t}^{(k+1)} = \mathbf{t}^{(k)} - \alpha^{(k)}\mathbf{s}^{(k)}$.
5. Calculate $\mathbf{p}^{(k+1)} = \mathbf{q}^{(k+1)} + \beta^{(k)}\mathbf{p}^{(k)}$, where $\mathbf{q}^{(k+1)} = \mathbf{A}^*\mathbf{t}^{(k)}$ and $\beta^{(k)} = ||\mathbf{q}^{(k+1)}||^2 / ||\mathbf{q}^{(k)}||^2$.
6. Repeat Procedures 2–5 for k with an increment of 1 until the residual $\mathbf{t}^{(k+1)}$ in Procedure 4 becomes small enough.

Here, $*$ represents the conjugate transpose of matrix. Then, $\mathbf{y}^{(k)} = \Delta\mathbf{x}^{(k)}$ where the residual $\mathbf{t}^{(k+1)}$ is small enough is the solution of Eq. 5.22, or Eq. 5.21. In procedure 1 of the CGNR algorithm, initial guess $\mathbf{y}^{(0)} = \Delta\mathbf{x}^{(0)} = -(\mathbf{J}^{\mathrm{T}}\mathbf{J})^{-1}\mathbf{J}^{\mathrm{T}}\mathbf{r}(\mathbf{x}^{(0)})$ is required. We set the initial value $\mathbf{x}^{(0)} = \log(\mathbf{f}^{0})$ with $\mathbf{f}^{(0)} = 10^{7}[\mathrm{m}^{-2}\mathrm{s}^{-1}\mathrm{eV}^{-1}]$. The flow chart of the inverse problem is shown in Figure 5.7.

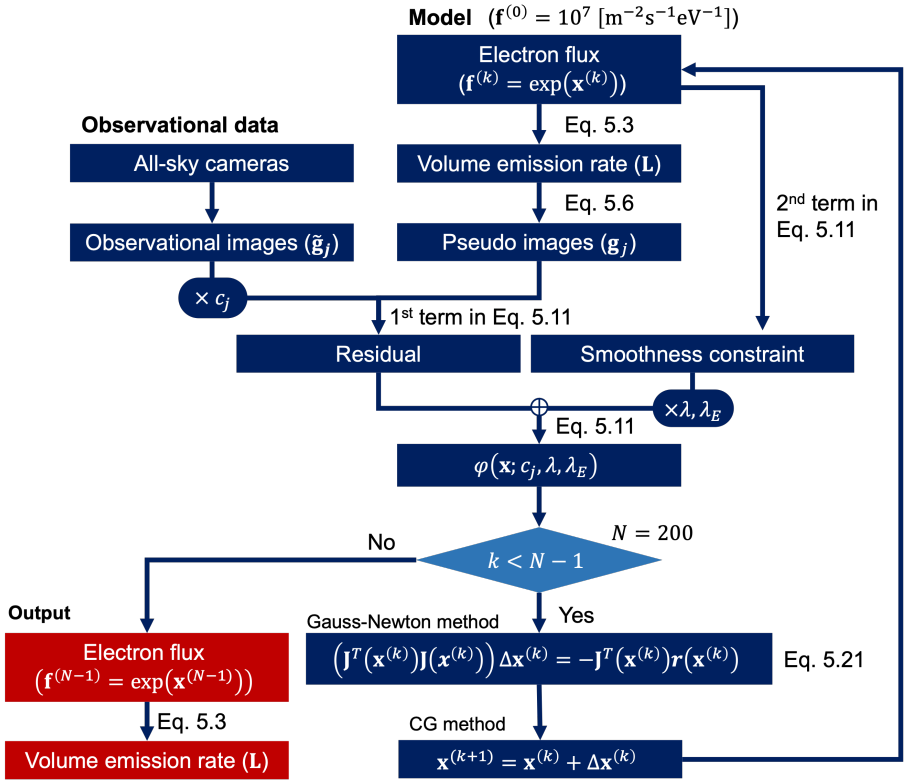

Figure 5.7. Flow chart of the inverse problem.

PsA patches shown in Figure 5.3a are embedded in the background diffuse auroral emission. We found that a horizontally uniform diffuse aurora causes ambiguity in the reconstruction results, since the altitude of the uniform auroral structure cannot be determined from the single-wavelength images. The VER reconstructed from auroral images without background emission subtraction had unexpected large value at the northern and western part of the reconstruction region (Figure 5.8). Thus, we subtracted the background emission from the images prior to the ACT reconstruction. We created the background emission image by assuming the same VER values for all voxels. The value was determined by comparing the auroral intensity profiles crossed the PsA patch with the created background emission (Figure 5.9b). The background VER was taken to be 75 cm^{-3} s^{-1} (Figure 5.9c) and was subtracted from the original image (Figure 5.9d).

5.2.5 Determination of Hyperparameters

The fivefold cross-validation method was used to determine the hyperparameters λ, λ_E, c_{ABK}, and c_{KIL} [Stone, 1974]. Firstly, the full dataset was divided into 5 subsets, where the k-th subset consists of the

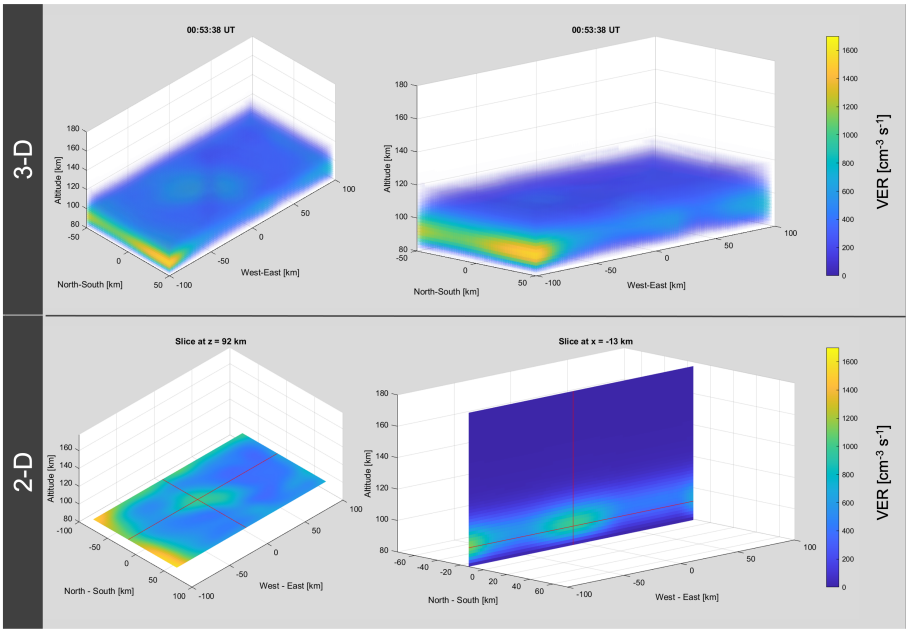

Figure 5.8. Preliminary results of reconstruction from auroral image without background emission subtraction.

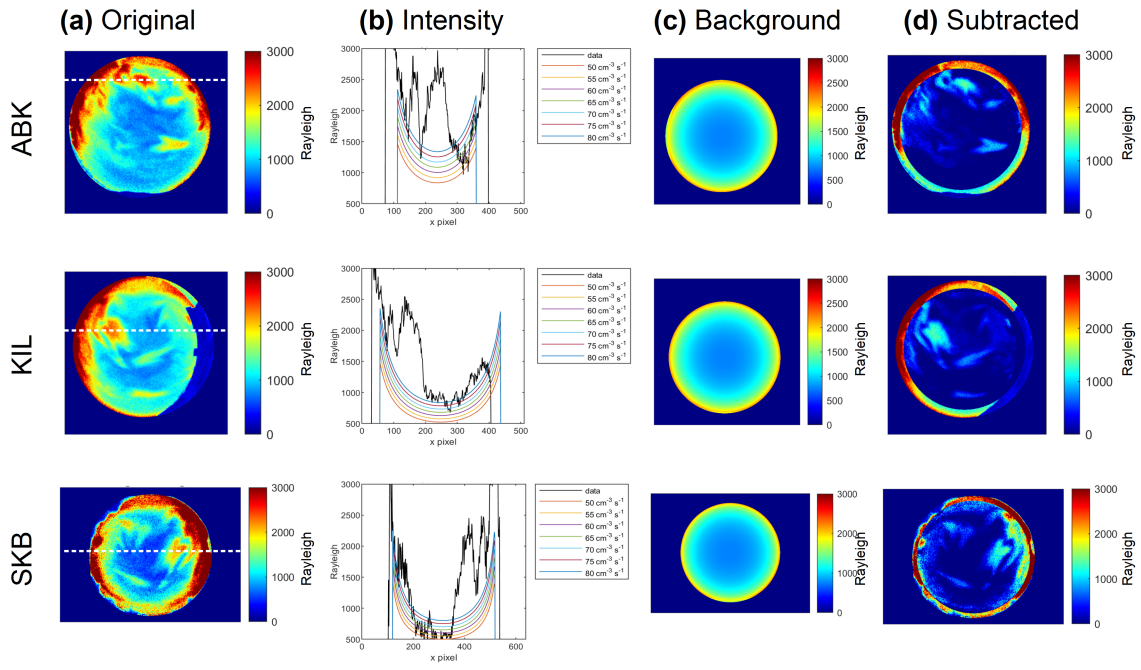

Figure 5.9. Determination of the background emission intensity. (a) Original images. (b) The auroral intensity profiles along white dashed lines in Figure 5.9a. (c) Background emission intensity created by assuming that all voxels have 75 cm^{-3} s^{-1}. (d) Auroral images produced by subtracting the images in Figure 5.9c from those in Figure 5.9a.

k-th, $k+5$-th, $k+10$-th,... elements of the vectors $\tilde{\mathbf{g}}$. Then, the cross-validation score for the assumed hyperparameters $(\lambda, \lambda_E, c_j)$ was calculated as follows.

Out of the 5 subsets, one was selected as a test set ($\tilde{\mathbf{g}}_j^{\mathrm{tes}}$), while the others as a training set ($\tilde{\mathbf{g}}_j^{\mathrm{tra}}$). We found the solution $\hat{\mathbf{x}}$ to minimize $\varphi(\mathbf{x}; \lambda, \lambda_E, c_{\mathrm{ABK}}, c_{\mathrm{KIL}})$ using only the training set $\tilde{\mathbf{g}}_j^{\mathrm{tra}}$ and then predicted the test set $\tilde{\mathbf{g}}_j^{\mathrm{tes}}(\hat{\mathbf{x}})$. The sum of the squares of the residuals between the test and predicted data was calculated as:

$$\delta(\lambda, \lambda_E, c_{\mathrm{ABK}}, c_{\mathrm{KIL}}) = \sum_j \left|\left| c_j \tilde{\mathbf{g}}_j^{\mathrm{tes}} - \mathbf{g}_j^{\mathrm{tes}} \right|\right|^2 . \tag{5.24}$$

The cross-validation score $\bar{\delta}(\lambda, \lambda_E, c_{\mathrm{ABK}}, c_{\mathrm{KIL}})$ was calculated by averaging over 5 $\delta(\lambda, \lambda_E, c_{\mathrm{ABK}}, c_{\mathrm{KIL}})$s, which were obtained by replacing the test set with one of the training sets in turn. The hyperparameters λ, λ_E, c_{ABK}, and c_{KIL} were determined by minimizing $\bar{\delta}(\lambda, \lambda_E, c_{\mathrm{ABK}}, c_{\mathrm{KIL}})$ with a trial-and-error method. In addition, the number of iterations for the Gauss-Newton algorithm was also simultaneously determined to be 200 to minimize $\bar{\delta}$.

5.3 Result and Discussion

5.3.1 Reconstruction of a Model Aurora

We reconstructed a model PsA patch from pseudo auroral images to evaluate the analytical error of ACT before reconstructing the observed PsA patch. To create pseudo auroral images, we prepared horizontal distributions of the total, Q_0, and the characteristic energy, E_{c}. As a next step, we derived the 3-D VER, L, as shown in Figure 5.10a. The total energy was assumed to have a Gaussian shape in horizontal directions with a maximum value of 6 mW m^{-2}, while the energy distribution was assumed to be a Maxwellian distribution with an isotropic characteristic energy of 15 keV. Figure 5.10b shows the pseudo auroral images viewed from three stations, obtained by solving the forward problem with L. We added random noise from the normal distribution, with a mean value of 0 and a standard deviation determined from observed auroral images. Figure 5.10c shows Q_0 and E_{c} of the electron flux reconstructed from the pseudo auroral images, including the noise. Values of Q_0 were calculated as $Q_0 = \sum_i E_i f(E_i)(E_{i+1} - E_i)$. Since we assume the energy distribution to be a Maxwellian distribution, the characteristic energy can be written as $E_{\mathrm{c}} = \frac{1}{2}\langle E \rangle = \frac{1}{2}\frac{Q_0}{\sum_i f(E_i)(E_{i+1}-E_i)}$. We calculated the errors between the model and the result for Q_0, E_{c}, and L (Figure 5.10d). Median errors values were -5% for Q_0, -21% for E_{c}, and -11% for L. The northwestern part of Q_0 was overestimated by at most 23%, the edge part was underestimated by at most 29%, while the central part was more accurately reconstructed with an error of $\sim -8\%$. Similarly, the central part of E_{c} was correctly reconstructed, while the edge part (in particular, the northwestern part) was underestimated by at most 56%. The underestimation of E_{c} was caused by the overestimation of the emission altitude (Figure 5.10d): information on this parameter is easily lost when obtaining the auroral

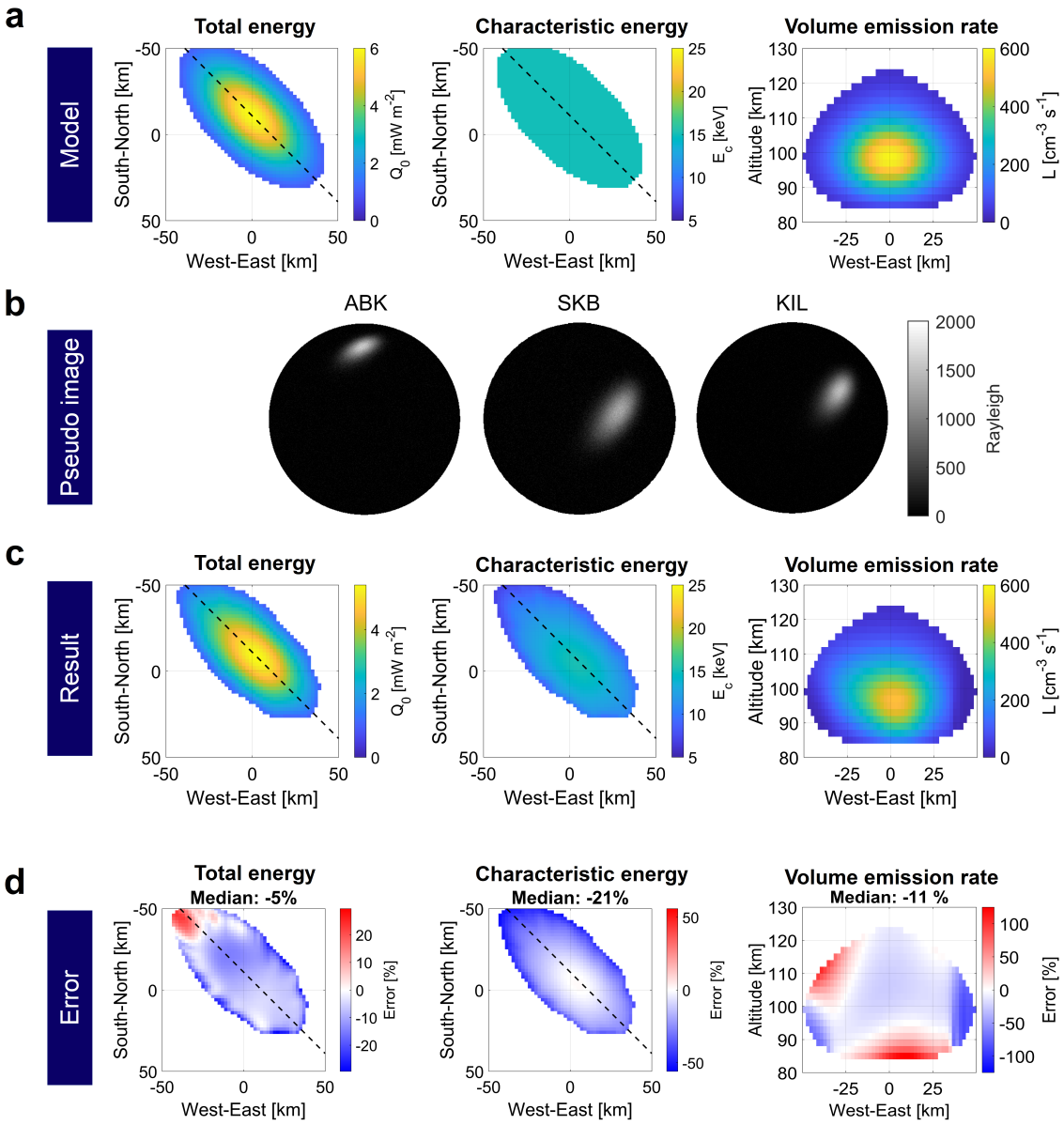

Figure 5.10. (a) Horizontal distribution of the prepared total Q_0 and characteristic energy E_c of precipitating electrons and vertical cross section of the volume emission rate L along the dashed lines are shown in the left and middle panels. We derived L from the prepared Q_0 and E_c values by solving the forward problem. Q_0 and E_c are not shown for Q_0 values less than 1 mW m^{-2}. (b) Pseudo auroral images obtained from model volume emission rates by solving the forward problem. (c) Horizontal distribution of Q_0 and E_c and vertical distribution of L reconstructed by aurora computed tomography from Figure 5.10b. (d) Errors of Q_0, E_c, and L, calculated as $(Error) = [(Result) - (Error))]/(Model) \times 100$ where $Model$ is Figures 5.10a and $Result$ is 5.10c.

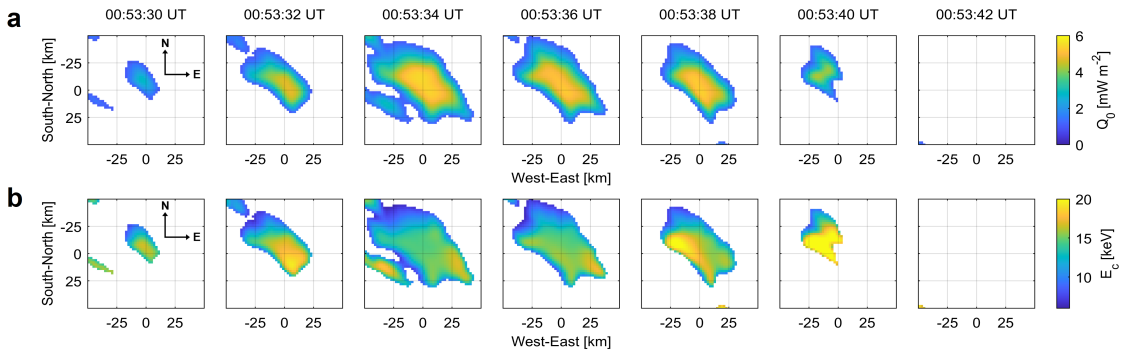

Figure 5.11. (a) Total, Q_0, and (b) characteristic energy, E_c, of precipitating electron flux reconstructed from the auroral images obtained at 00:53:30–00:53:42 UT on February 18, 2018. Results of Q_0 and E_c where Q_0 is less than 1 mW m^{-2} are not shown.

image, since the structure of the PsA patch is vertically thin and horizontally wide. In addition, the signal-to-noise ratio in the edge part is lower than in the central part, since we assumed a Gaussian shape for the horizontal distribution of Q_0, thus tending to reduce the accuracy in the edge part.

It should be noted that results obtained using the hyperparameters determined by the cross-validation method revealed unexpected fine structures: to avoid this, we set the lower limit of λ by a different method, namely by minimizing the residual sum of squares between the model and the reconstructed result of Q_0 and E_c. The lower limit on λ makes it challenging to reconstruct actual fine-scale structures in patches.

To summarize this subsection, we quantitatively evaluated the error of reconstruction results by ACT. Although the error tended to be large in the edge part of a PsA patch, we could reconstruct most part of the PsA patch from pseudo auroral images. Thus, we are able to reconstruct a PsA patch with sufficient accuracy by applying the ACT method to observed PsAs.

5.3.2 Precipitating Electrons

Figure 5.11 shows Q_0 and E_c as reconstructed from auroral images obtained at 00:53:30–00:53:42 UT on February 18, 2018 given in Figure 5.3a. The maximum value of Q_0 was $\sim$6 mW m^{-2}, while the characteristic energy of reconstructed precipitating electrons in the interested PsA patch ranged from 6 to 23 keV, consistently with the results obtained from the past sounding rocket and low-altitude satellite observations [e.g., McEwen *et al.*, 1981, Miyoshi *et al.*, 2015b]. The horizontal distribution of E_c was neither uniform nor stable in the patch during the pulsation. In particular, the southwestern part of E_c was enhanced at 00:53:38 UT. It should be noted that the edge and northwestern parts of E_c are expected to be underestimated, due to analytical errors, as shown in Figure 5.10d. These temporal variations probably indicate changes in the cyclotron resonance energy of whistler-mode chorus waves during the pulsation: these chorus waves scatter electrons into a loss cone near the magnetic equator. More in detail, the cyclotron resonance energy of chorus waves depends on the background magnetic field, electron density, and wave

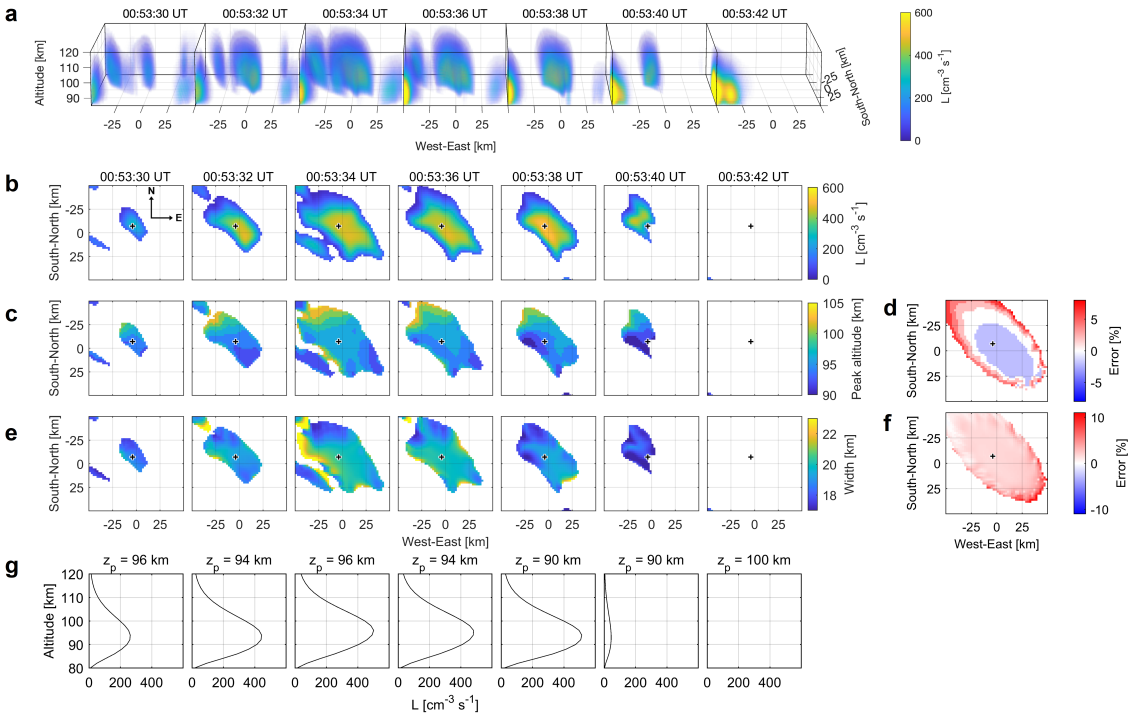

Figure 5.12. (a) Reconstructed 3-D volume emission rates (VERs) L. VERs lower than 1 cm^{-3} s^{-1} are not shown. (b) Cross sections in the horizontal plane at an altitude of 94 km. VERs are not shown for Q_0 values lower than 1 mW m^{-2}. (c) Peak altitudes of the reconstructed L and (d) their associated errors, determined using the model aurora. (e) Altitude widths of the reconstructed L and (f) their associated errors. (g) Altitude profiles of L at the EISCAT radar observation point, as indicated by black plus marks in Figures 5.12b–5.12f.

frequency [e.g., Kennel and Petschek, 1966]. Thus, the observed temporal variations represent changes in the magnetospheric source region's background magnetic or plasma environment during the pulsation. The ACT method is helpful for investigating PsA-associated temporal variations in the horizontal distribution of precipitating electrons using only observation data obtained from the ground.

5.3.3 Volume Emission Rate

Figure 5.12a shows the 3-D VER of a 4278-nm aurora derived from the reconstructed electron flux by solving the forward problem. Cross sections in the horizontal plane at an altitude of 94 km are shown in Figure 5.12b. The peak altitude ranges from 90 to 104 km (Figure 5.12c): its associated error, estimated by the method described in Subsection 5.3.1, is shown in Figure 5.12d. More in detail, the high peak altitude in the northwestern part is expected to be overestimated by at most 8%, due to analytical errors, as shown in Figure 5.12d, which corresponds to the underestimation of the characteristic energy of differential flux (Figure 5.10d). The full width at half maximum of altitude distribution is almost uniform, with a median value of $\sim$20 km (Figure 5.12e). For the most part, altitude width is expected to be overestimated by $\sim$2% (Figure 5.12f) from the error estimation given in Subsection 5.3.1. The reconstructed peak altitude and width are

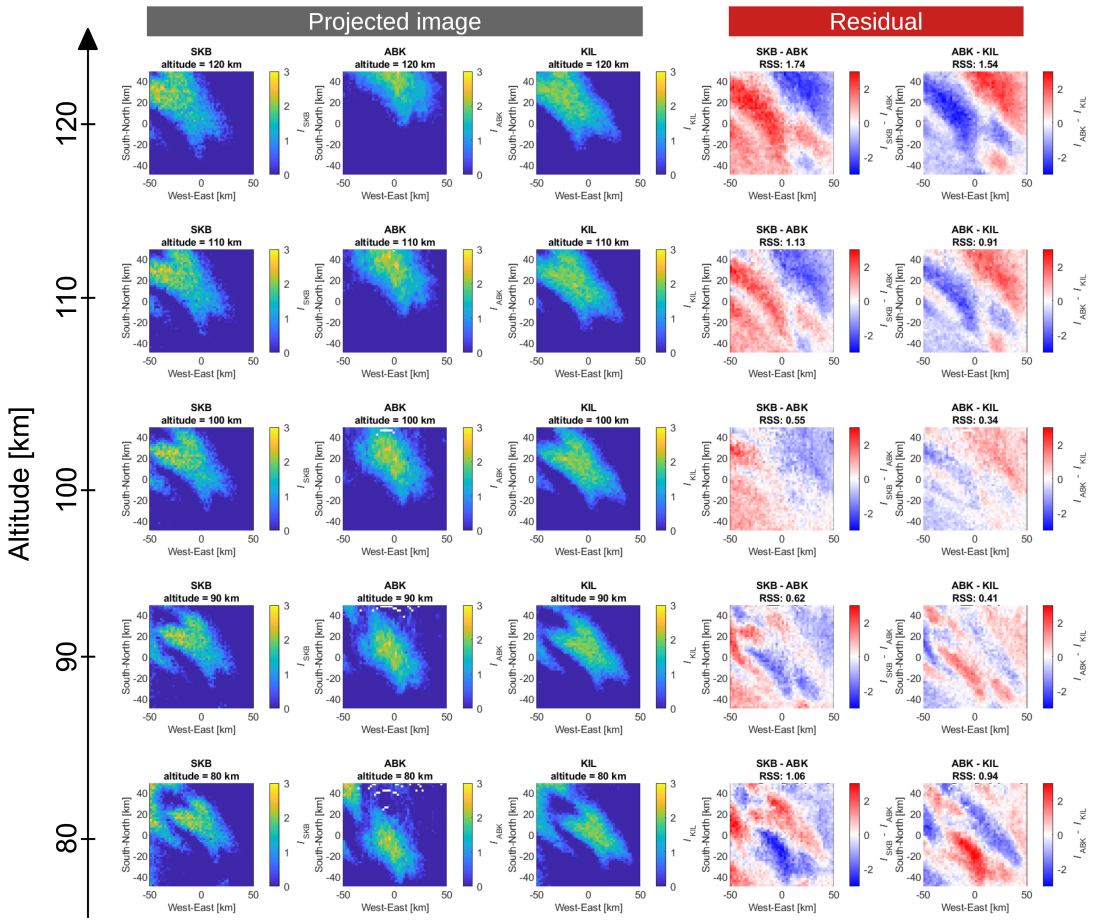

Figure 5.13. Auroral images projected at altitudes from 80 to 120 km, with an interval of 2 km. The images were obtained at Skibotn (SKB), Abisko (ABK), and Kilpisjärvi (KIL) at 00:53:36 UT on February 18, 2018. Residuals between projected images at each pair of stations (SKB and ABK, and ABK and KIL) are shown. The auroral intensity is normalized as follows: $I_j = (I - \bar{I})/\sigma$, where I is the auroral intensity, $\bar{I}$ is the average of I, σ is the standard deviation of I, and j signifies ABK, KIL, or SKB. The residual squared sum (RSS) is shown at the top of each panel: it is calculated as follows: RSS $= \Sigma \frac{(I_j - I_{j+1})^2}{N}$, where N is the number of datapoints.

consistent with those estimated in most past studies by stereoscopic observations or by an incoherent scatter radar [Brown *et al.*, 1976, Jones *et al.*, 2009, Kataoka *et al.*, 2016]. Nevertheless, our results do not support the thin (<1 km vertical extent) PsA patches reported in Stenbaek-Nielsen and Hallinan [1979]. Figure 5.12g shows the altitude profile of the VERs at the EISCAT radar observation point, represented by black plus symbols in Figures 5.12b–f: these VERs are converted to the ionospheric electron density in the next Subsection to compare the electron density obtained by reconstruction with that by the EISCAT radar.

Here, we compare the emission altitudes estimated with ACT and by Kondo [2016], who estimated the peak altitude of a PsA patch with a different method, and check the consistency between the two methods. We project the observed auroral images at altitudes from 80 to 120 km, with an interval of 2 km (Figure 5.13). Kondo [2016] determined the emission altitude to be the altitude where the residual squared sum between two projected images reach a minimum value (Figure 5.14) by changing the projection altitude of

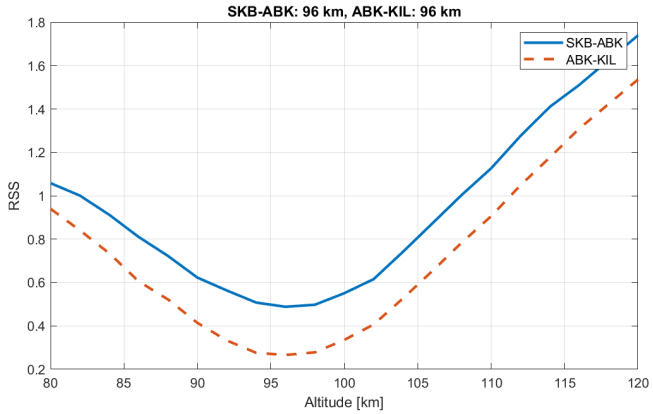

Figure 5.14. Residual squared sum (RSS) between the projected images at two stations (SKB and ABK, and ABK and KIL) at each altitude at 00:53:36 UT on February 18, 2018. The altitude at which the RSS reached a minimum value is shown in the panel title.

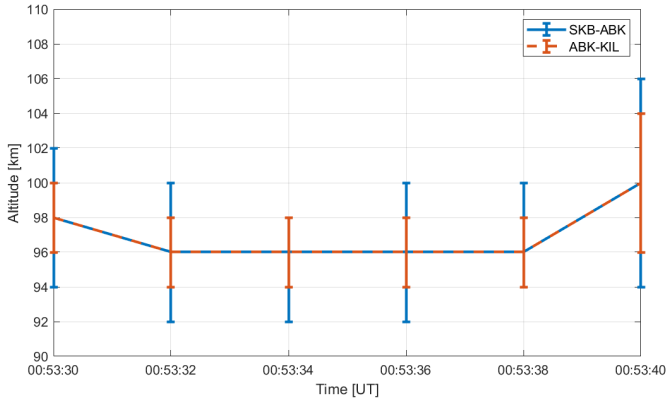

Figure 5.15. The altitude at which the residual squared sum (RSS) reached a minimum value for each of 6 timepoints from 00:53:30 UT to 00:53:40 UT on February 18, 2018. Error bars indicate the altitude range over which the RSS was less than 1.2 times each RSS minimum.

the observed auroral images from 80 to 120 km, with an interval of 2 km. The estimated peak altitude range was 92–106 km from 00:53:30 UT to 00:53:40 UT (Figure 5.15), closely matching with those determined by ACT.

5.3.4 Electron Density

Altitude profiles of the VER of a 427.8 nm aurora at the EISCAT radar observation point, shown in Figure 5.12g, have been converted to the ionospheric electron density, and compared with that obtained from the EISCAT radar data at 00:53:30–00:53:42 UT on February 18, 2018. The continuity equation for the electron density can be written as [e.g., Hosokawa *et al.*, 2010]:

$$\frac{\partial n_e}{\partial t} = kL - \alpha_{\mathrm{eff}} n_e^2, \tag{5.25}$$

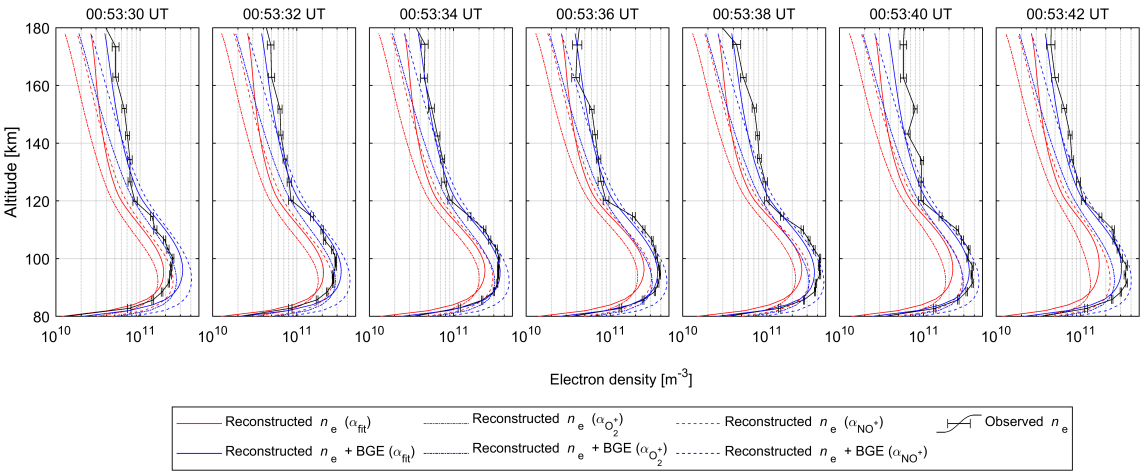

Figure 5.16. Electron density altitude profiles converted from the reconstructed volume emission rates with the subtraction of background emission (red lines), without the background emission (blue lines), and observed by the EISCAT radar (black lines). Details of effective recombination coefficients $\alpha_{\rm fit}$, $\alpha_{\rm O_2^+}$, and $\alpha_{\rm NO^+}$ are explained in the text. The measurement uncertainties are represented by error bars.

where n_e [m^{-3}] is the electron density, L [m^{-3} s^{-1}] is the VER of a 427.8 nm aurora, k is a positive constant for converting VER to the ionization rate (see Appendix), and $\alpha_{\rm eff}$ is the effective recombination rate. We derived the electron density from the VER by solving the continuity equation (Eq. 5.25) by applying the Runge–Kutta method. The initial value was derived from the continuity equation under steady state conditions (i.e., $\partial n_e/\partial t = 0$) using reconstructed L at 00:53:36 UT. VERs have been interpolated linearly to use the Runge–Kutta method. The altitude profile of $\alpha_{\rm eff}$ has been investigated by several studies using rocket- and ground-based measurements. Vickrey *et al.* [1982] summarized many of these results and proposed the following best fit parameterization:

$$\alpha_{\rm fit} = 2.5 \times 10^{-12} \exp\left(-z/51.2\right) \qquad [\mathrm{m^3 s^{-1}}], \tag{5.26}$$

where z is the altitude in km. Semeter and Kamalabadi [2005] used effective recombination coefficients $\alpha_{\rm NO^+}$ and $\alpha_{\rm O_2^+}$ for NO^+ and O_2^+, respectively [Walls and Dunn, 1974], as upper and lower bounds on $\alpha_{\rm eff}$:

$$\alpha_{\rm NO^+} = 4.2 \times 10^{-13} (300/T_n)^{0.85} \qquad [\mathrm{m^3 s^{-1}}], \tag{5.27}$$

$$\alpha_{\rm O_2^+} = 1.95 \times 10^{-13} (300/T_n)^{0.7} \qquad [\mathrm{m^3 s^{-1}}]. \tag{5.28}$$

Here T_n is the neutral temperature. The red lines in Figure 5.16 show the derived electron densities using these three recombination coefficients. We note that these values are underestimated compared to the electron densities observed by the EISCAT radar (black lines in Figure 5.16): this is probably related to background emission subtraction from the auroral images prior to ACT and from the ambiguity in the effective recombination coefficient. Electron densities reconstructed from auroral images without background emission subtraction are shown as blue lines for reference in Figure 5.16. Reconstruction results

from images, including background emission, approached the electron density profile observed with the EISCAT radar, although there still remains some ambiguity due to the uniform emission. More in detail, we noted that the electron density was reconstructed correctly to some extent after auroral emission intensity decreased at 00:53:40 UT: this is due to the incorporation of the time derivative term in the continuity equation. The electron density would seem to have rapidly decreased after 00:53:40 UT, if the time derivative term were not considered, thus suggesting that the time derivative term should be considered when we use the continuity equation (Eq. 5.25) to derive electron densities associated with PsAs.

It should be noted that the electron density is still underestimated at higher altitudes ($>\sim$140 km): this would be improved by reconstructing low-energy electron flux from auroral images in the F region, such as atomic oxygen emission at 844.6 nm.

5.4 Brief Summary

We successfully reconstructed for the first time PsA patches and the horizontal distribution of precipitating electrons through the ACT method with 427.8-nm auroral images obtained at three observation points. We improved the previously proposed ACT method by adding the following processes: subtraction of the background diffuse aurora from the auroral images prior to ACT, estimation of the relative sensitivity between ASCs, and determination of the hyperparameters of the regularization term. Characteristic energies of the reconstructed electron fluxes (6 to 23 keV) and peak altitudes of the reconstructed VERs (90 to 104 km) were consistent with those reported in previous studies (Figure 5.17). We determined that the horizontal distribution of the characteristic energy was neither uniform nor stable in the patch during the pulsation. For the investigation of the spatial and temporal variations of PsAs, the capability of ACT provides complementary opportunities to *in situ* data obtained by rockets and satellites. The error in the ACT method was evaluated using a model auroral patch. We confirmed that the central part of the characteristic energy was correctly reconstructed with an error of $\sim$0.1%. The energy of electron flux was underestimated at the patch edge by at most 56%, while the peak altitude was overestimated by at most 8%. The reconstructed electron flux will be improved in future works by incorporating auroral images at various wavelengths.

As described in Section 5.1, Tanaka *et al*. [2011] extended ACT to G-ACT: they demonstrated that the incorporation of the ionospheric electron density from the EISCAT radar improved the accuracy of the reconstructed electron flux for discrete auroras. By combining G-ACT with 3-D ionospheric observation data obtained by EISCAT_3D (Figure 5.18, http://www.eiscat3d.se.) scheduled to begin its operation in 2023, which would allow us to improve the VER reconstruction accuracy and electron density.

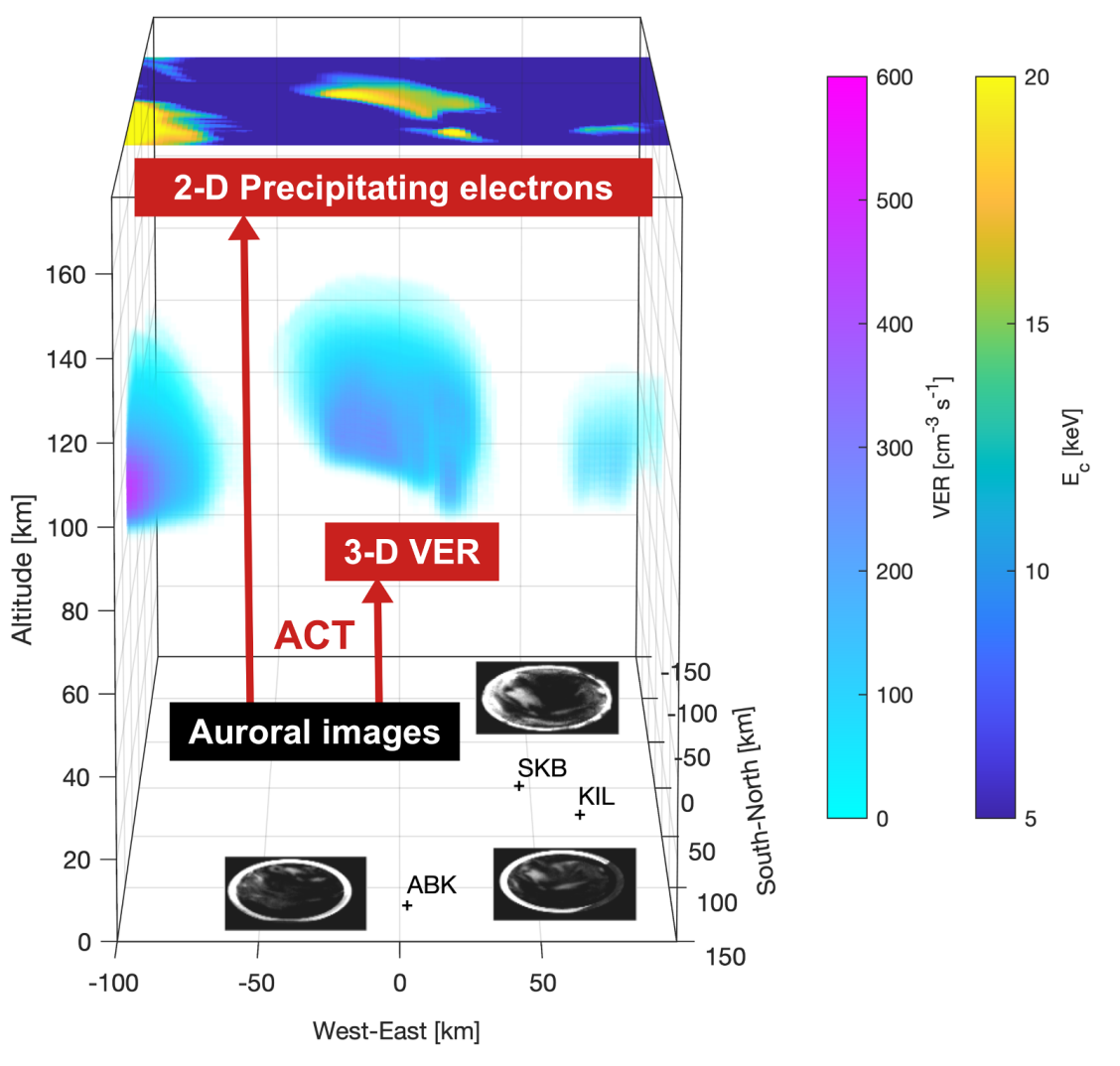

Figure 5.17. Summary of the reconstruction of the characteristic energy of precipitating electrons and 3-D volume emission rate from 427.8-nm images.

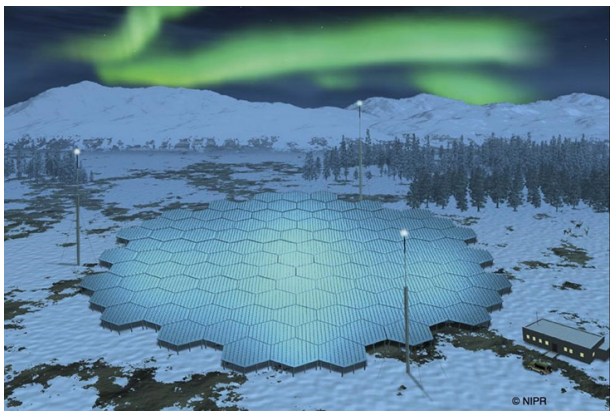

Figure 5.18. Schematic illustration of the EISCAT_3D radar.

6 Discussion and Future Prospects

The PA scattering by ECH waves has been considered to be one of the generation mechanisms of PsAs since 1970s. Lyons [1974] theoretically suggested that ECH waves cause the pitch angle scattering of electrons in energies from a few hundred eV to a few keV. On the other hand, my Master's degree study [Fukizawa *et al*., 2018] found that the ECH wave intensity has a correlation with the PsA emission intensity. Furthermore, the energy of precipitating electrons was estimated to be $\sim$3–4 keV from the time lag when the cross-correlation coefficient between the ECH wave intensity and the PsA emission intensity had the maximum value. However, there was no observation of the PA scattering by ECH waves in the inner magnetosphere.

In this study, we focus on the PA scattering by ECH waves. The relationships among LBC, UBC, ECH waves, electron precipitation, ionospheric density, and PsAs are schematically shown in Figure 6.1. In Chapter 2, we clarify that ECH waves scattered $\sim$5-keV electrons into a loss cone using *in situ* observation data obtained by the Arase satellite. Indeed, a computer simulation showed that the electron flux correlated with the ECH wave intensity caused a 557.7-nm auroral emission with a brightness of 200 R: we suggest that this had a quasi-periodic modulation, since the electron flux had a modulation with a periodicity of $\sim$26 s. These results indicate that ECH waves contribute to cause the PsA emission in the E region. On the other hand, in Chapter 3, the energy range of electrons that have been effectively scattered by ECH waves have been quantitatively estimated from Arase satellite data. We found that the PA scattering is the most efficient for electrons in an energy range smaller than 1 keV, while it is not efficient for a few keV electrons, consistently with the quasi-linear theory [e.g., Horne and Thorne, 2000]. Moreover, statistical results suggest that PsA emissions in the E region are mainly caused by LBC waves, rarely by ECH waves. In Chapter 4, we show that the electron density enhancement in the F region associated with PsAs has been frequently observed. Here we suggest that low-energy ($<$1 keV) electron precipitation by ECH and UBC waves contribute to auroral emissions and ionizations in the F region. It should be noted that we do not completely decline the possibility of the PA scattering of a few keV electrons by ECH waves. The cyclotron resonance energy of ECH waves could reach a few keV, depending on the background magnetic and plasma environment, as reported in Chapter 2.

One of the remarkable findings of this study is that PsAs are frequently accompanied by low-energy electron precipitation: this is crucial since it would cause ion upflow, as described in Section 1.7 [Liang *et al*., 2018]. A further statistical analysis to investigate the relationship between ion upflow and low-energy electron precipitation associated with PsA should be conducted in future studies.

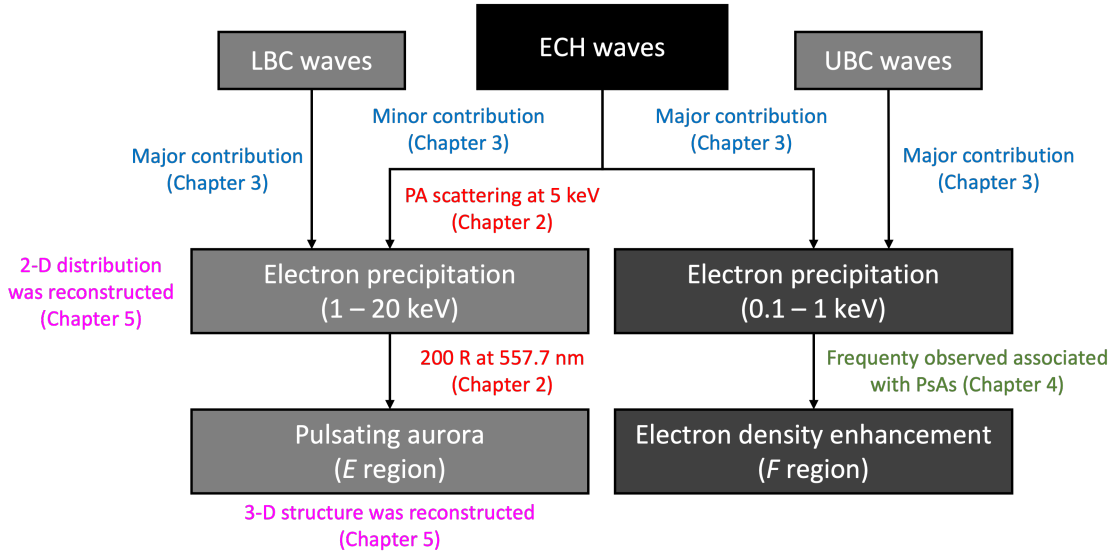

Figure 6.1. Block diagram summarizing the results of this study.

Another important finding of this study is that low-energy electrons are scattered into loss cones by UBC and ECH waves in the inner magnetosphere: this would also cause a background low-energy electron density variation in the magnetosphere by outflows from the ionosphere. Thus, there might be a causal relationship between ECH, UBC, and LBC waves. Nevertheless, the source mechanism which causes chorus wave modulation in the inner magnetosphere is not understood. Nishimura *et al.* [2015] defined the effect of background low-energy electron density variation in the magnetosphere on the modulation of chorus waves as described in Section 1.7. The large cold plasma density is favorable for the excitation of chorus waves as described in Section 1.4. We expect that the relationship between ECH, UBC, and LBC waves will contribute to understand the generation mechanism of chorus wave modulation in the inner magnetosphere. This is beyond the scope of this study, and should be attributed in future studies. For example, the ion velocity along the geomagnetic field observed by the EISCAT radar during PsA events should be statistically analyzed.

In Chapter 5, we succeeded to reconstruct the horizontal distribution of precipitating electrons in the energy range from 30 eV to 100 keV, by using the image data of PsA emission at 427.8 nm obtained at three ground stations. The F-region auroral structure is crucial to estimate the low-energy electron precipitation associated with PsAs. Here we carried out the reconstruction of the E-region aurora using the 427.8 nm emission data: therefore, the reconstruction of the F-region aurora is a future issue. One method to reconstruct low-energy electrons is applying F-region auroral emissions to ACT, such as OI 844.6 nm: this improvement is challenging because an 844.6 nm emission is dimmer than a 427.8 nm, thus precise validation of noise is necessary. Another method is to apply G-ACT in which the ionospheric electron density obtained from the EISCAT or EISCAT_3D radar are included. Here, we propose a principle of considering the time change of the ionospheric electron density with G-ACT. The continuity equation of

electron density, N_{e}, can be written as

$$\frac{\partial N_{\mathrm{e}}}{\partial t} + \nabla \cdot (N_e \mathbf{v}) = q - \alpha_{\mathrm{eff}} N_{\mathrm{e}}^2, \tag{6.1}$$

where t is time, $\mathbf{v}$ is the velocity, q is the ionization rate, and α_{eff} is the effective recombination coefficient. Using backward-difference approximation, Eq. 6.1 can be written as

$$N_{\mathrm{e}}^2 + \frac{N_{\mathrm{e,\,t}} - N_{\mathrm{e,\,t\text{-}1}}}{\alpha_{\mathrm{eff}} \Delta t} + \frac{nabla \cdot (N_e \mathbf{v})}{\alpha_{\mathrm{eff}}} - \frac{q}{\alpha_{\mathrm{eff}}} \approx 0. \tag{6.2}$$

By adding the problem to minimize RSS of the left side of Eq. 6.2 into Eq. 5.11, the precipitating electron flux can be reconstructed by taking the time change of N_{e} into account. In this way, precipitating electrons, including low-energy, would be reconstructed, since the electron density data obtained from incoherent scatter radars contain the information about F-region ionization caused by low-energy electron precipitation. As a result, we will be able to obtain a more accurate characteristic electron energy than that estimated with the GLOW model described in Chapter 4.

7 Conclusion

In the present research, we investigate the generation mechanism of electron precipitation associated with pulsating auroras (PsAs), mainly focusing on the pitch angle scattering of electrons by electrostatic electron cyclotron harmonic (ECH) waves. More in detail, we show for the first time evidences that ECH waves actually scattered electrons into the loss cone. Furthermore, we reveal that lower (LBC) and upper band choruses (UBC), and ECH waves effectively contribute to scatter electrons in different energies. Ionospheric F-region electron density enhancements associated with PsAs have been quantitatively examined using the ground-based optical and radar data. In addition, we reconstruct the three-dimensional (3-D) structure of PsA patches from ground-based auroral images with sufficient accuracy. Detailed results are summarized as follows.

In Chapter 2, we verify that ECH waves scattered electrons into a loss cone by comparing the ECH wave intensity with the electron flux inside the loss cone. The ECH wave intensity and the electron flux have been obtained through onboard frequency analyzer (OFA) and low-energy particle experiments–electron analyzer (LEPe) on the Arase satellite, respectively. The cross-correlation coefficient between the ECH wave intensity and the loss cone electron flux at the energy of $\sim$5 keV is statistically significant, while that with the LBC wave intensity at the same energy is small. As a next step, we calculate the pitch angle (PA) diffusion coefficients of ECH waves, assuming that the wave normal angle is 87.0° , and that the electron temperature is 1 eV. As a result, the diffusion coefficient of 5-keV electrons is 10 times greater than that of other energies where cross-correlation coefficients were small. The linear growth rate of ECH waves is also large when the wave normal angle and electron temperature satisfy this condition. The downward electron flux correlated with ECH waves would cause the 557.7-nm auroral emission with a column emission rate of about 200 R, according to the model calculation.

In Chapter 3, we carry out a statistical analysis on the strong electron scattering caused by LBC, UBC, and ECH waves through wave and electron data obtained by the Arase satellite from March 24, 2017 to August 31, 2020. More in detail, we examine the relationship between loss cone filing ratios for different energies and LBC, UBC, and ECH waves, thus revealing energy ranges where these waves contribute to scatter electrons into the loss cone. The slopes of regression lines for wave amplitudes versus loss cone filling ratios are positive, while correlation coefficients between them are statistically significant in electron energies greater than $\sim$2 keV for LBC waves, at $\sim$0.4 keV for UBC waves, and smaller than $\sim$2 keV for ECH waves. In these energies, the occurrence rate of the strong PA scattering is also high considering each wave. Energy ranges are consistent with those predicted by the quasi-linear theory in the case that PA

diffusion coefficients exceed the strong diffusion level. Here we clarify, basing on the statistical analysis of the Arase data, that a few keV electron precipitation scattered by ECH waves is not common, while electrons with energy less than 1 keV are scattered by ECH waves. This statistical result is not necessarily inconsistent with the results of Chapter 2, since the cyclotron resonance energy of ECH waves could reach a few keV depending on the magnetospheric conditions.

In Chapter 4, we conduct two case studies to investigate in detail the relationship between the electron density height profile and auroral type by using the data obtained by the European incoherent scatter (EISCAT) radar and the auroral all-sky imager at Tromsø on February 18, 2018 and October 27, 2019. In addition, we conduct statistical studies for 14 events, in order to clarify how often F-region electron density enhancement accompanied with PsA occurs. As a consequence, we find that 76% of electron density height profiles show a local peak in the F region with an electron temperature enhancement. Compared with the model profile ionized by electron precipitation, we suggest that 76% of these local peaks have been caused by precipitating electrons in an energy range lower than 100 eV. The hourly averaged occurrence rate of these local peaks exceeds 80% in the 22–3 magnetic local times. We thus suggest that the electron density enhancement in the F region would be caused by ECH waves in the magnetosphere or secondary electrons. Another candidate is polar patches traveling from the dayside ionosphere.

In Chapter 5, we examine the horizontal distribution of precipitating electrons of a PsA patch by the reconstruction method called Aurora Computed Tomography (ACT). The 3-D volume emission rate (VER) and the horizontal distribution of precipitating electrons were calculated from 428-nm auroral images obtained at three stations. To apply the ACT method to a diffuse and dimmer PsA auroral patch, we improved the previous ACT used for discrete auroras in the following three points: (1) the subtraction of background diffuse aurora from the auroral images before conducting ACT, (2) the estimation of the relative sensitivity between all-sky cameras, and (3) the determination of the hyperparameters of the regularization term. As a result, we succeeded to reconstruct for the first time 3-D VER of the PsA patch and the horizontal distribution of precipitating electrons. The characteristic energy of the reconstructed precipitating electron flux ranges from 6 to 23 keV, while the peak altitude of the reconstructed VER ranges from 90 to 104 km, consistently with previous studies. Furthermore, the horizontal distribution of precipitating electron's characteristic energy is neither uniform nor stable in the PsA patch during the pulsation: these spatial and temporal variations indicate changes in the cyclotron resonance energy of LBC waves during the pulsation. Therefore, the observed spatiotemporal variations of PsAs are important to understand the background magnetic and plasma conditions in the magnetospheric source region. Our results of reconstruction of precipitating electrons and VER are a great advantage of multiple ground-based data, since such 3-D distributions cannot be obtained by rockets and satellites. We quantitatively evaluated the reconstructed results using a model PsA patch by adding artificial noises and compared with the ionospheric electron density observed by the EISCAT radar. By considering the time derivative term of the continuity equation, the electron density was

reconstructed with sufficient accuracy even when the PsA intensity decreased.

Appendix

Derivation of *k*

In the Appendix, we describe how to obtain the positive constant $k(z)$ in Section 5.3.4. The N_2^+ (427.8 nm) emission is due to the transition from $N_2^+(B^2\Sigma_u^+)_{v=0}$ to $N_2^+(X^2\Sigma_g^+)_{v=1}$. According to Sergienko and Ivanov [1993], the volume emission rate $L(z)$ [m^{-3} s^{-1}] is approximated by

$$L(z) = \frac{A_{0-1}q_{0-0}}{\Sigma_v A_{0-v}} w(z) = \frac{A_{0-1}q_{0-0}}{\Sigma_v A_{0-v}} \frac{p(z)\varepsilon(z)}{\Delta\varepsilon}, \tag{A.1}$$

where z is the altitude, A_{0-1} is the Einstein coefficient for the transition from $N_2^+(B^2\Sigma_u^+)_{v=0}$ to $N_2^+(X^2\Sigma_g^+)_{v=1}$, $w(z)$ [m^{-3} s^{-1}] is the production rate of $N_2^+(B^2\Sigma_u^+)$, q_{0-0} is the Franck–Condon factor for the electronic transition from $N_2^+(X^1\Sigma_g^+)_{v=0}$ to $N_2^+(B^2\Sigma_u^+)_{v=0}$, $p(z)$ is the probability that $\varepsilon(z)$ excites N_2, $\varepsilon(z)$ [eV m^{-3} s^{-1}] is the energy deposition rate, and $\Delta\varepsilon$ [eV] is the excitation energy cost of $N_2^+(B^2\Sigma_u^+)$. The ionization rate due to the precipitating electrons $q_{\text{ion}}(z)$ [m^{-3} s^{-1}] is given by

$$q_{\text{ion}}(z) = \frac{\varepsilon(z)}{\Delta\varepsilon_{\text{ion}}}. \tag{A.2}$$

where $\Delta\varepsilon_{\text{ion}}$ is the energy used to produce an ion–electron pair. Substituting Eq. A.1 into Eq. A.2 gives

$$q_{\text{ion}}(z) = \frac{\Sigma_v A_{0-v)}}{A_{0-1}q_{0-0}} \frac{\Delta\varepsilon}{\Delta\varepsilon_{\text{ion}}} \frac{1}{p(z)} L(z). \tag{A.3}$$

Therefore, the positive constant $k(z)$ for converting volume emission rate to the ionization rate is

$$k(z) = \frac{\Sigma_v A_{0-v)}}{A_{0-1}q_{0-0}} \frac{\Delta\varepsilon}{\Delta\varepsilon_{\text{ion}}} \frac{1}{p(z)}. \tag{A.4}$$

The parameters used for the calculation are summarized in Table A.1.

Table A.1. Simulation parameters used in Eq. A.4

Parameter	Value	References
$\frac{A_{0-1}q_{0-0}}{\Sigma_v A_{0-v}}$	0.197	Jones [1974]
$\Delta\varepsilon$	350 eV	Sergienko and Ivanov [1993]
$\Delta\varepsilon_{\text{ion}}$	35.5 eV	Semeter and Kamalabadi [2005]
$p(z)$	Calculated from MSISE-00 model	Picone *et al*. [2002]

References

Agapitov, O., Krasnoselskikh, V., Khotyaintsev, Y. V., and Rolland, G. (2012). Correction to "A statistical study of the propagation characteristics of whistler waves observed by Cluster". *Geophysical Research Letters*, 39(24):29–31. doi: 10.1029/2012gl054320.

Akasofu, S. I. (1964). The development of the auroral substorm. *Planetary and Space Science*, 12(4): 273–282. doi: 10.1016/0032-0633(64)90151-5.

Akasofu, S.-I. Development of Magnetospheric Physics. In Kan, J., Potemra, T., Kokubun, S., and Iijima, T., editors, *Magnetospheric Substorms*, pages 3–9. American Geophysical Union, 1991. doi: 10.1029/gm064p0003.

Angelopoulos, V., Cruce, P., Drozdov, A., Grimes, E. W., Hatzigeorgiu, N., King, D. A., Larson, D., Lewis, J. W., McTiernan, J. M., Roberts, D. A., Russell, C. L., Hori, T., Kasahara, Y., Kumamoto, A., Matsuoka, A., Miyashita, Y., Miyoshi, Y., Shinohara, I., Teramoto, M., Faden, J. B., Halford, A. J., McCarthy, M., Millan, R. M., Sample, J. G., Smith, D. M., Woodger, L. A., Masson, A., Narock, A. A., Asamura, K., Chang, T. F., Chiang, C. Y., Kazama, Y., Keika, K., Matsuda, S., Segawa, T., Seki, K., Shoji, M., Tam, S. W., Umemura, N., Wang, B. J., Wang, S. Y., Redmon, R., Rodriguez, J. V., Singer, H. J., Vandegriff, J., Abe, S., Nose, M., Shinbori, A., Tanaka, Y. M., UeNo, S., Andersson, L., Dunn, P., Fowler, C., Halekas, J. S., Hara, T., Harada, Y., Lee, C. O., Lillis, R., Mitchell, D. L., Argall, M. R., Bromund, K., Burch, J. L., Cohen, I. J., Galloy, M., Giles, B., Jaynes, A. N., Le Contel, O., Oka, M., Phan, T. D., Walsh, B. M., Westlake, J., Wilder, F. D., Bale, S. D., Livi, R., Pulupa, M., Whittlesey, P., DeWolfe, A., Harter, B., Lucas, E., Auster, U., Bonnell, J. W., Cully, C. M., Donovan, E., Ergun, R. E., Frey, H. U., Jackel, B., Keiling, A., Korth, H., McFadden, J. P., Nishimura, Y., Plaschke, F., Robert, P., Turner, D. L., Weygand, J. M., Candey, R. M., Johnson, R. C., Kovalick, T., Liu, M. H., McGuire, R. E., Breneman, A., Kersten, K., and Schroeder, P. The Space Physics Environment Data Analysis System (SPEDAS), 2019. ISSN 15729672. URL http://dx.doi.org/10.1007/s11214-018-0576-4.

Ashour-Abdalla, M. and Kennel, C. F. (1978). Nonconvective and Convective Electron Cyclotron Harmonic Instability. *Journal of Geophysical Research*, 83(A4):1531–1543. doi: 10.1029/JA083iA04p01531.

Aso, T., Hashimoto, T., Abe, M., Ono, T., and Ejiri, M. (1990). On the analysis of aurora stereo observations. *Journal of Geomagnetism and Geoelectricity*, 42(5):579–595. doi: 10.5636/jgg.42.579.

Aso, T., Ejiri, M., Miyaoka, H., Hashimoto, T., Abu, T. Y., and Abe, M. (1993). Aurora stereo observation in Iceland. *Proceedings of the NIPR Symposium on Upper Atmosphere Physics*, 6:1–14.

Aso, T., Ejiri, M., Urashima, A., Miyaoka, H., Steen, Å., Brändstrom, U., and Gustavsson, B. (1998). First results of auroral tomography from ALIS-Japan multi-station observations in March, 1995. *Earth, Planets and Space*, 50(1):81–86. doi: 10.1186/BF03352088.

Aso, T., Gustavsson, B., Tanabe, K., Brändström, U., Sergienko, T., and Sandahl, I. (2008). A proposed Bayesian model on the generalized tomographic inversion of aurora using multi-instrument data. *Proc. 33rd Annual European Meeting on Atmospheric Studies by Optical Methods, IRF Sci. Rep.*, (292):105–109.

Baker, D. N., Fritz, T. A., Wilken, B., Higbie, P. R., Kaye, S. M., Kivelson, M. G., Moore, T. E., Stüdemann, W., Masley, A. J., Smith, P. H., and Vampola, A. L. (1982). Observation and modeling of energetic particles at synchronous orbit on July 29, 1977. *Journal of Geophysical Research*, 87(A8):5917. doi: 10.1029/ja087ia08p05917.

Barrett, R., Berry, M., Chan, T. F., Demmel, J., Donato, J., Dongarra, J., Eijkhout, V., Pozo, R., Romine, C., and van der Vorst, H. (1994). Templates for the solution of linear systems: Building blocks for iterative methods. *Society for Industrial and Applied Mathematics*. doi: 10.1137/1.9781611971538.

Baumjohann, W., Paschmann, G., and Lühr, H. (1990). Characteristics of high-speed ion flows in the plasma sheet. *Journal of Geophysical Research*, 95(A4):3801. doi: 10.1029/ja095ia04p03801.

Bernstein, I. B. (1958). Waves in a plasma in a magnetic field. *Physical Review*, 109(1):10–21. doi: 10.1103/PhysRev.109.10.

Brown, N. B., Davis, T. N., Hallinan, T. J., and Stenbaek-Nielsen, H. C. (1976). Altitude of pulsating aurora determined by a new instrumental thechnique. *Geophysical Research Letters*, 3(7):403–404. doi: 10.1029/GL003i007p00403.

Bryant, D. A., Hall, D. S., and Lepine, D. R. (1978). Electron acceleration in an array of auroral arcs. *Planetary and Space Science*, 26(1):81–92. doi: 10.1016/0032-0633(78)90039-9.

Büchner, J. and Zelenyi, L. M. (1989). Regular and chaotic charged particle motion in magnetotaillike field reversals: 1. Basic theory of trapped motion. *Journal of Geophysical Research*, 94(A9):11821–11842. doi: 10.1029/ja094ia09p11821.

Burtis, W. J. and Helliwell, R. A. (1976). Magnetospheric chorus: Occurrence patterns and normalized frequency. *Planetary and Space Science*, 24(11). doi: 10.1016/0032-0633(76)90119-7.

Burtis, W. and Helliwell, R. (1969). Banded Chorus. a New Type of Vlf Radiation Observed in the Magnetosphere By Ogo 1 and Ogo 3. *J Geophys Res*, 74(11):3002–3010. doi: 10.1029/ja074i011p03002.

Burton, R. K. and Holzer, R. E. (1974). The origin and propagation of chorus in the outer magnetosphere. *Journal of Geophysical Research*, 79(7):1014–1023. doi: 10.1029/ja079i007p01014.

Carpenter, D. L. and Park, C. G. (1973). On what ionospheric workers should know about the plasmapause - plasmasphere. *Reviews of Geophysics and Space Physics*, 11(1):133–154. doi: 10.1029/RG011i001p00133.

Cowley, S. W. H. (1995). The Earth's magnetosphere: A brief begginer's guide. *EOS Trans. AGU*, 76(51): 525–532. doi: 10.1029/95EO00322.

Cuperman, S. and Landau, R. W. (1974). On the enhancement of the whistler mode instability in the magnetosphere by cold plasma injection. *Journal of Geophysical Research*, 79(1):128–134. doi: 10.1029/JA079i001p00128.

Dahlgren, H., Lanchester, B. S., Ivchenko, N., and Whiter, D. K. (2017). Variations in energy, flux, and brightness of pulsating aurora measured at high time resolution. *Annales Geophysicae*, 35(3):493–503. doi: 10.5194/angeo-35-493-2017.

Eather, R. H. (1969). Short-period auroral pulsations in 6300 OI. *Journal of Geophysical Research: Space Physics*, 74(21):4998–5004.

Ebihara, Y. and Miyoshi, Y. *Dynamic Inner Magnetosphere: A Tutorial and Recent Advances. In Dynamic Magnetosphere*, volume 3. Springer, iaga speci edition, 2011. ISBN 9789400705012. doi: 10.1007/978-94-007-0501-2.

Evans, D. S., Davidson, G. T., Voss, H. D., Imhof, W. L., Mobilia, J., and Chiu, Y. T. (1987). Interpretation of electron spectra in morningside pulsating aurorae. *Journal of Geophysical Research*, 92(A11):12295–12306. doi: 10.1029/JA092iA11p12295.

Folkestad, K., Hagfors, T., and Westerlund, S. (1983). EISCAT: An updated description of technical characteristics and operational capabilities. *Radio Science*, 18(6):867–879. doi: 10.1029/RS018i006p00867.

Frey, S., Frey, H. U., Carr, D. J., Bauer, O. H., and Haerendel, G. (1996). Auroral emission profiles extracted from three-dimensionally reconstructed arcs. *Journal of Geophysical Research: Space Physics*, 101 (A10):21731–21741. doi: 10.1029/96ja01899.

Fu, X., Cowee, M. M., Friedel, R. H., Funsten, H. O., Gary, S. P., Hospodarsky, G. B., Kletzing, C., Kurth, W., Larsen, B. A., Liu, K., Macdonald, E. A., Min, K., Reeves, G. D., Skoug, R. M., and Winske, D. (2014). Whistler anisotropy instabilities as the source of banded chorus: Van Allen Probes observations and particle-in-cell simulations. *Journal of Geophysical Research: Space Physics*, 119(10):8282–8298. doi: 10.1002/2014JA020364.

Fujii, R., Oguti, T., and Yamamoto, T. (1985). Relationships between pulsating auroras and field-aligned electric currents. *Memoirs of National Institute of Polar Research. Special issue*, 36:95–1003.

Fukizawa, M., Sakanoi, T., Miyoshi, Y., Hosokawa, K., Shiokawa, K., and Katoh, Y. (2018). Electrostatic electron cyclotron harmonic waves as a candidate to cause pulsating auroras. *Geophysical Research Letters*, 45(12):661–668. doi: 10.1029/2018GL080145.

Fukizawa, M., Sakanoi, T., Miyoshi, Y., Kazama, Y., Katoh, Y., Kasahara, Y., Matsuda, S., Matsuoka, A., Kurita, S., Shoji, M., Teramoto, M., Imajo, S., Sinohara, I., Wang, S. Y., Tam, S. W., Chang, T. F., Wang, B. J., and Jun, C. W. (2020). Pitch-angle scattering of inner magnetospheric electrons caused by ECH waves obtained with the Arase satellite. *Geophysical Research Letters*, 47(23):1–9. doi: 10.1029/2020GL089926.

Fukizawa, M., Sakanoi, T., Ogawa, Y., Tsuda, T. T., and Hosokawa, K. (2021). Statistical Study of Electron Density Enhancements in the Ionospheric F Region Associated With Pulsating Auroras . *Journal of Geophysical Research: Space Physics*, 126(12):1–14. doi: 10.1029/2021ja029601.

Fukizawa, M., Sakanoi, T., Miyoshi, Y., Kazama, Y., Katoh, Y., Kasahara, Y., Matsuda, S., Kumamoto, A., Tsuchiya, F., Matsuoka, A., Kurita, S., Nakamura, S., Shoji, M., Teramoto, M., Imajo, S., Shinohara, I., Wang, S.-Y., Tam, S. W.-Y., Chang, T.-F., Wang, B.-J., and Jun, C.-W. (2022a). Statistical Study of Strong Diffusion of Low-Energy Electrons by Chorus and ECH Waves Based on In Situ Observations. *Earth and Space Science Open Archive*, pages 1–14. doi: 10.1002/essoar.10510087.1.

Fukizawa, M., Sakanoi, T., Tanaka, Y., Ogawa, Y., Hosokawa, K., Gustavsson, B., Kauristie, K., Kozlovsky, A., Raita, T., Brändström, U., and Sergienko, T. (2022b). Reconstruction of precipitating electrons and three-dimensional structure of a pulsating auroral patch from monochromatic auroral images obtained from multiple observation points. *Annales Geophysicae Discussions*, pages 1–15. doi: 10.5194/angeo-2022-5.

Gao, Z., Su, Z., Zhu, H., Xiao, F., Zheng, H., Wang, Y., Shen, C., and Wang, S. (2016). Intense low-frequency chorus waves observed by Van Allen Probes: Fine structures and potential effect on radiation belt electrons. *Geophysical Research Letters*, 43(3):967–977. doi: 10.1002/2016GL067687.

Glauert, S. A. and Horne, R. B. (2005). Calculation of pitch angle and energy diffusion coefficients with the PADIE code. *Journal of Geophysical Research: Space Physics*, 110(A4):1–15. doi: 10.1029/2004JA010851.

Gough, M., CHristiansen, P., Martelli, G., and Gershuny, E. (1979). Interaction of electrostatic waves with warm electrons at the geomagnetic equator. *Nature*, 279(5713):515–517. doi: 10.1038/279515a0.

Grono, E. and Donovan, E. (2018). Differentiating diffuse aurora based on phenomenology. *Annales Geophysicae*, 36(3):891–898. doi: 10.5194/angeo-36-891-2018.

Gurnett, D. A. and Bhattacharjee, A. *Introduction to plasma physics: With space and laboratory applications*, volume 9780521364. Cambridge University Press, 2005. ISBN 9780511809125. doi: 10.1017/CBO9780511809125.

Hayakawa, M., Yamanaka, Y., Parrot, M., and Lefeuvre, F. (1984). Wave Normals of Magnetospheric Chorus Emissions Observed on Board Geos 2. *Journal of Geophysical Research*, 89(A5):2811–2821. doi: 10.1029/JA089iA05p02811.

Hestenes, M. and Stiefel, E. (1952). Methods of conjugate gradients for solving linear systems. *Journal of Research of the National Bureau of Standards*, 49(6):409–436. doi: 10.6028/jres.049.044.

Horne, R. B. (1989). Path-integrated growth of electrostatic waves: The generation of terrestrial myriametric radiation. *J. Geophys. Res.*, 94(A7):8895–8909. doi: http://dx.doi.org/10.1029/JA094iA07p08895.

Horne, R. B. and Thorne, R. M. (2000). Electron pitch angle diffusion by electrostatic electron cyclotron harmonic waves: The origin of pancake distributions. *Journal of Geophysical Research*, 105:5391–5402. doi: 10.1029/1999JA900447.

Horne, R. B., Thorne, R. M., Meredith, N. P., and Anderson, R. R. (2003). Diffuse auroral electron scattering by electron cyclotron harmonic and whistler mode waves during an isolated substorm. *Journal of Geophysical Research: Space Physics*, 108(A7):1–12. doi: 10.1029/2002JA009736.

Hosokawa, K., Ogawa, Y., Kadokura, A., Miyaoka, H., and Sato, N. (2010). Modulation of ionospheric conductance and electric field associated with pulsating aurora. *Journal of Geophysical Research: Space Physics*, 115(3):1–11. doi: 10.1029/2009JA014683.

Hosokawa, K., Miyoshi, Y., Ozaki, M., Oyama, S. I., Ogawa, Y., Kurita, S., Kasahara, Y., Kasaba, Y., Yagitani, S., Matsuda, S., Tsuchiya, F., Kumamoto, A., Kataoka, R., Shiokawa, K., Raita, T., Turunen, E., Takashima, T., Shinohara, I., and Fujii, R. (2020). Multiple time-scale beats in aurora: precise orchestration via magnetospheric chorus waves. *Scientific reports*, 10(1):3380. doi: 10.1038/s41598-020-59642-8.

Hosokawa, K., Miyoshi, Y., Oyama, S. I., Ogawa, Y., Kurita, S., Kasahara, Y., Kasaba, Y., Yagitani, S., Matsuda, S., Ozaki, M., Tsuchiya, F., Kumamoto, A., Takashima, T., Shinohara, I., and Fujii, R. (2021). Over-Darkening of Pulsating Aurora. *Journal of Geophysical Research: Space Physics*, 126(4):1–15. doi: 10.1029/2020JA028838.

Hubbard, R. F., Birmingham, T. J., and Hones, E. W. (1979). Magnetospheric electrostatic emissions and cold plasma densities. *Journal of Geophysical Research*, 84:5828–5838. doi: 10.1029/JA084iA10p05828.

Inan, U. S., Chiu, Y. T., and Davidson, G. T. (1992). Whistler-mode chorus and morningside aurorae. *Geophysical Research Letters*, 19(7):653–656. doi: 10.1029/92GL00402.

Jones, A. *Aurora*. D. Reidel Publishing Company, Dordrecht, 1974. ISBN 978-90-277-0273-9. doi: 10.1007/978-94-010-2099-2.

Jones, S. L., Lessard, M. R., Fernandes, P. A., Lummerzheim, D., Semeter, J. L., Heinselman, C. J., Lynch, K. A., Michell, R. G., Kintner, P. M., Stenbaek-Nielsen, H. C., and Asamura, K. (2009). PFISR and ROPA observations of pulsating aurora. *Journal of Atmospheric and Solar-Terrestrial Physics*, 71(6-7): 708–716. doi: 10.1016/j.jastp.2008.10.004.

Kasaba, Y., Ishisaka, K., Kasahara, Y., Imachi, T., Yagitani, S., Kojima, H., Matsuda, S., Shoji, M., Kurita, S., Hori, T., Shinbori, A., Teramoto, M., Miyoshi, Y., Nakagawa, T., Takahashi, N., Nishimura, Y., Matsuoka, A., Kumamoto, A., Tsuchiya, F., and Nomura, R. (2017). Wire Probe Antenna (WPT) and Electric Field Detector (EFD) of Plasma Wave Experiment (PWE) aboard the Arase satellite: specifications and initial evaluation results. *Earth, Planets and Space*, 69(1). doi: 10.1186/s40623-017-0760-x.

Kasahara, S., Miyoshi, Y., Yokota, S., Mitani, T., Kasahara, Y., Matsuda, S., Kumamoto, A., Matsuoka, A., Kazama, Y., Frey, H. U., Angelopoulos, V., Kurita, S., Keika, K., Seki, K., and Shinohara, I. (2018a). Pulsating aurora from electron scattering by chorus waves. *Nature*, 554(7692):337–340. doi: 10.1038/nature25505.

Kasahara, S., Yokota, S., Mitani, T., Asamura, K., Hirahara, M., Shibano, Y., and Takashima, T. (2018b). Medium-energy particle experiments—electron analyzer (MEP-e) for the exploration of energization and radiation in geospace (ERG) mission. *Earth, Planets and Space*, 70(1):1–16. doi: 10.1186/s40623-018-0847-z.

Kasahara, S., Miyoshi, Y., Kurita, S., Yokota, S., Keika, K., Hori, T., Kasahara, Y., Matsuda, S., Kumamoto, A., Matsuoka, A., Seki, K., and Shinohara, I. (2019). Strong Diffusion of Energetic Electrons by Equatorial Chorus Waves in the Midnight-to-Dawn Sector. *Geophysical Research Letters*, 46(22):12685–12692. doi: 10.1029/2019GL085499.

Kasahara, Y., Kasaba, Y., Kojima, H., Yagitani, S., Ishisaka, K., Kumamoto, A., Tsuchiya, F., Ozaki, M., Matsuda, S., Imachi, T., Miyoshi, Y., Hikishima, M., Katoh, Y., Ota, M., Shoji, M., Matsuoka, A., and Shinohara, I. (2018c). The Plasma Wave Experiment (PWE) on board the Arase (ERG) satellite. *Earth, Planets and Space*, 70(1). doi: 10.1186/s40623-018-0842-4.

Kasahara, Y., Kojima, H., Matsuda, S., Ozaki, M., Yagitani, S., Shoji, M., Nakamura, S., Kitahara, M., Miyoshi, Y., and Shinohara, I. The PWE/OFA instrument Level-2 power spectrum data of Exploration of energization and Radiation in Geospace (ERG) Arase satellite, 2018d.

Kasahara, Y., Kumamoto, A., Tsuchiya, F., Kojima, H., Matsuda, S., Matsuoka, A., Teramoto, M., Shoji, M., Nakamura, S., Kitahara, M., Maeda, A., Miyoshi, Y., and I., S. The PWE/HFA instrument Level-3 electron density data of Exploration of energization and Radiation in Geospace (ERG) Arase satellite, 2021.

Kataoka, R., Fukuda, Y., Uchida, H. A., Yamada, H., Miyoshi, Y., Ebihara, Y., Dahlgren, H., and Hampton, D. (2016). High-speed stereoscopy of aurora. *Annales Geophysicae*, 34(1):41–44. doi: 10.5194/angeo-34-41-2016.

Kataoka, R., Miyoshi, Y., Hampton, D., Ishii, T., and Kozako, H. (2012). Pulsating aurora beyond the ultra-low-frequency range. *Journal of Geophysical Research: Space Physics*, 117(8):1–5. doi: 10.1029/2012JA017987.

Kazama, Y., Wang, B. J., Wang, S. Y., Ho, P. T., Tam, S. W., Chang, T. F., Chiang, C. Y., and Asamura, K. (2017). Low-energy particle experiments–electron analyzer (LEPe) onboard the Arase spacecraft. *Earth, Planets and Space*, 69(1). doi: 10.1186/s40623-017-0748-6.

Kazama, Y., Kojima, H., Miyoshi, Y., Kasahara, Y., Usui, H., Wang, B. J., Wang, S. Y., Tam, S. W., Chang, T. F., Ho, P. T., Asamura, K., Kumamoto, A., Tsuchiya, F., Kasaba, Y., Matsuda, S., Shoji, M., Matsuoka, A., Teramoto, M., Takashima, T., and Shinohara, I. (2018). Density Depletions Associated With Enhancements of Electron Cyclotron Harmonic Emissions: An ERG Observation. *Geophysical Research Letters*, 45(19):10,075–10,083. doi: 10.1029/2018GL080117.

Kazama, Y., Miyoshi, Y., Kojima, H., Kasahara, Y., Kasahara, S., Usui, H., Wang, B. J., Wang, S. Y., Tam, S. W., Chang, T. F., Asamura, K., Matsuda, S., Kumamoto, A., Tsuchiya, F., Kasaba, Y., Shoji, M., Matsuoka, A., Teramoto, M., Takashima, T., and Shinohara, I. (2021). Arase Observation of Simultaneous Electron Scatterings by Upper-Band and Lower-Band Chorus Emissions. *Geophysical Research Letters*, 48(14):1–10. doi: 10.1029/2021GL093708.

Kennel, C. F. and Engelmann, F. (1966). Velocity space diffusion from weak plasma turbulence in a magnetic field. *Physics of Fluids*, 9(12):2377–2388. doi: 10.1063/1.1761629.

Kennel, C. F. and Petschek, H. E. (1966). Limit on stably trapped particle fluxes. *Journal of Geophysical Research*, 71(1):1–28. doi: 10.1029/JZ071i001p00001.

Kennel, C. F., Scarf, F. L., Fredricks, R. W., McGehee, J. H., and Coroniti, F. V. (1970). VLF electric field observations in the magnetosphere. *Journal of Geophysical Research*, 75(31):6136–6152. doi: 10.1029/JA075i031p06136.

Khazanov, G. V., Glocer, A., and Himwich, E. W. (2014). Magnetosphere-ionosphere energy interchange in the electron diffuse aurora. *Journal of Geophysical Research: Space Physics*, 119(1):171–184. doi: 10.1002/2013JA019325.

Khazanov, G. V., Tripathi, A. K., Sibeck, D., Himwich, E., Glocer, A., and Singhal, R. P. (2015a). Electron distribution function formation in regions of diffuse aurora. *Journal of Geophysical Research: Space Physics*, 120(11):9891–9915. doi: 10.1002/2015JA021728.

Khazanov, G. V., Tripathi, A. K., Singhal, R. P., Himwich, E. W., Glocer, A., and Sibeck, D. G. (2015b). Superthermal electron magnetosphere-ionosphere coupling in the diffuse aurora in the presence of ECH waves. *Journal of Geophysical Research: Space Physics*, 120(1):445–459. doi: 10.1002/2014JA020641.

Knudsen, D. J., Burchill, J. K., Cameron, T. G., Enno, G. A., Howarth, A., and Yau, A. W. (2015). The CASSIOPE/e-POP Suprathermal Electron Imager (SEI). *Space Science Reviews*, 189(1-4):65–78. doi: 10.1007/s11214-015-0151-1.

Kondo, H. (2016). *Coordinated EISCAT and optical observation of omega-band pulsating aurora and electron density enhancement in the D-region ionosphere*. PhD thesis, Tohoku University.

Kumamoto, A., Tsuchiya, F., Kasahara, Y., Kasaba, Y., Kojima, H., Yagitani, S., Ishisaka, K., Imachi, T., Ozaki, M., Matsuda, S., Shoji, M., Matsuoka, A., Katoh, Y., Miyoshi, Y., and Obara, T. (2018). High Frequency Analyzer (HFA) of Plasma Wave Experiment (PWE) onboard the Arase spacecraft. *Earth, Planets and Space*, 70(1):1–14. doi: 10.1186/s40623-018-0854-0.

Kurita, S., Miyoshi, Y., Cully, C. M., Angelopoulos, V., Contel, O. L., Hikishima, M., and Misawa, H. (2014). Observational evidence of electron pitch angle scattering driven by ECH waves. *Geophysical Research Letters*, 41(22):8076–8080. doi: 10.1002/2014GL061927.

Lessard, M. A review of pulsating aurora. In Keiling, A., Donovan, E., Bagenal, F., and Karlsson, T., editors, *Auroral Phenomenology and Magnetospheric Processes: eEarth and Other Planets*. American Geophysical Union, 2012. doi: https://doi.org/10.1029/2011GM001187.

Li, W., Bortnik, J., Thorne, R. M., Nishimura, Y., Angelopoulos, V., and Chen, L. (2011). Modulation of whistler mode chorus waves: 2. Role of density variations. *Journal of Geophysical Research: Space Physics*, 116(6):1–13. doi: 10.1029/2010JA016313.

Li, W., Bortnik, J., Thorne, R. M., Cully, C. M., Chen, L., Angelopoulos, V., Nishimura, Y., Tao, J. B., Bonnell, J. W., and Lecontel, O. (2013). Characteristics of the poynting flux and wave normal vectors of whistler-mode waves observed on THEMIS. *Journal of Geophysical Research: Space Physics*, 118(4): 1461–1471. doi: 10.1002/jgra.50176.

Liang, J., Uritsky, V., Donovan, E., Ni, B., Spanswick, E., Trondsen, T., Bonnell, J., Roux, A., Auster, U., and Larson, D. (2010). THEMIS observations of electron cyclotron harmonic emissions, ULF waves, and pulsating auroras. *Journal of Geophysical Research: Space Physics*, 115(10):1–24. doi: 10.1029/2009JA015148.

Liang, J., Donovan, E., Jackel, B., Spanswick, E., and Gillies, M. (2016). On the 630nm red-line pulsating aurora: Red-line Emission Geospace Observatory observations and model simulations. *Journal of Geophysical Research: Space Physics RESEARCH*, 121:7988–8012. doi: 10.1002/2016JA022901.

Liang, J., Yang, B., Donovan, E., Burchill, J., and Knudsen, D. (2017). Ionospheric electron heating associated with pulsating auroras: A Swarm survey and model simulation. *Journal of Geophysical Research: Space Physics*, 122(8):8781–8807. doi: 10.1002/2017JA024127.

Liang, J., Donovan, E., Reimer, A., Hampton, D., Zou, S., and Varney, R. (2018). Ionospheric electron heating associated with pulsating auroras: joint optical and PFISR observations. *Journal of Geophysical Research: Space Physics*, 123(5):4430–4456. doi: 10.1029/2017JA025138.

Looper, M. D., Blake, J. B., and Mewaldt, R. A. (2005). Response of the inner radiation belt to the violent Sun-Earth connection events of October-November 2003. *Geophysical Research Letters*, 32(3):1–4. doi: 10.1029/2004GL021502.

Lyons, L. R. and Williams, D. J. (1984). Quantitative aspects of magnetospheric physics. *Quantitative aspects of magnetospheric physics.* doi: 10.1029/eo066i046p00781-02.

Lyons, L. R. (1974). Electron diffusion driven by magnetospheric electrostatic waves. *Journal of Geophysical Research*, 79(4):575–580. doi: 10.1029/ja079i004p00575.

Lyons, L. R. and Thorne, R. M. (1973). Equilibrium structure of radiation belt electrons. *Journal of Geophysical Research*, 78(13):2142–2149. doi: 10.1029/ja078i013p02142.

Ma, Q., Artemyev, A. V., Mourenas, D., Li, W., Thorne, R. M., Kletzing, C. A., Kurth, W. S., Hospodarsky, G. B., Reeves, G. D., Spence, H. E., and Wygant, J. (2017). Very Oblique Whistler Mode Propagation in the Radiation Belts: Effects of Hot Plasma and Landau Damping. *Geophysical Research Letters*, 44(24): 12,057–12,066. doi: 10.1002/2017GL075892.

Ma, Q., Connor, H. K., Zhang, X. J., Li, W., Shen, X. C., Gillespie, D., Kletzing, C. A., Kurth, W. S., Hospodarsky, G. B., Claudepierre, S. G., Reeves, G. D., and Spence, H. E. (2020). Global Survey of Plasma Sheet Electron Precipitation due to Whistler Mode Chorus Waves in Earth's Magnetosphere. *Geophysical Research Letters*, 47(15):1–11. doi: 10.1029/2020GL088798.

Matsuda, S., Kasahara, Y., Kojima, H., Kasaba, Y., Yagitani, S., Ozaki, M., Imachi, T., Ishisaka, K., Kumamoto, A., Tsuchiya, F., Ota, M., Kurita, S., Miyoshi, Y., Hikishima, M., Matsuoka, A., and Shinohara, I. (2018). Onboard software of Plasma Wave Experiment aboard Arase: instrument management and signal processing of Waveform Capture/Onboard Frequency Analyzer. *Earth, Planets and Space*, 70(1). doi: 10.1186/s40623-018-0838-0.

Matsuoka, A., Teramoto, M., Imajo, S., Kurita, S., Miyoshi, Y., and Shinohara, I. The MGF instrument Level-2 spin-averaged magnetic field data of Exploration of energization and Radiation in Geospace (ERG) Arase satellite, 2018a.

Matsuoka, A., Teramoto, M., Nomura, R., Nose, M., Fujimoto, A., Tanaka, Y., Shinohara, M., Nagatsuma, T., Shiokawa, K., Obana, Y., Miyoshi, Y., Mita, M., Takashima, T., and Shinohara, I. (2018b). The ARASE (ERG) magnetic field investigation. *Earth, Planets and Space*, 70(1):1–16. doi: 10.1186/s40623-018-0800-1.

McCrea, I., Aikio, A., Alfonsi, L., Belova, E., Buchert, S., Clilverd, M., Engler, N., Gustavsson, B., Heinselman, C., Kero, J., Kosch, M., Lamy, H., Leyser, T., Ogawa, Y., Oksavik, K., Pellinen-Wannberg, A., Pitout, F., Rapp, M., Stanislawska, I., and Vierinen, J. (2015). The science case for the EISCAT_3D radar. *Progress in Earth and Planetary Science*, 2(21). doi: https://doi.org/10.1186/s40645-015-0051-8.

McEwen, D. J., Yee, E., Whalen, B. A., and Yau, A. W. (1981). Electron energy measurements in pulsating auroras. *Canadian Journal of Physics*, 59(8):1106–1115. doi: 10.1139/p81-146.

McPherron, R. L., Russell, C. T., and Aubry, M. P. (1973). Satellite studies of magnetospheric substorms on August 15, 1968: 9. Phenomenological model for substorms. *Journal of Geophysical Research*, 78 (16):3131–3149. doi: 10.1029/ja078i016p03131.

Mende, S. B., Harris, S. E., Frey, H. U., Angelopoulos, V., Russell, C. T., Donovan, E., Jackel, B., Greffen, M., and Peticolas, L. M. (2008). The THEMIS array of ground-based observatories for the study of auroral substorms. *Space Science Reviews*, 141(1-4):357–387. doi: 10.1007/s11214-008-9380-x.

Meredith, N. P., Horne, R. B., Johnstone, A. D., and Anderson, R. R. (2000). The temporal evolution of electron distributions and associated wave activity following substorm injections in the inner magnetosphere. *J. Geophys. Res.*, 105(A6):12907–12917. doi: 10.1029/2000ja900010.

Meredith, N. P., Horne, R. B., Anderson, R. R., and Horne, B. (2001). Substorm dependence of chorus amplitudes: implications for the acceleration of electrons to relativistic energies. *Journal of Geophysical Research*, 106(A7):13165. doi: 10.1029/2000JA900156.

Meredith, N. P., Horne, R. B., Thorne, R. M., and Anderson, R. R. (2003). Favored regions for chorus-driven electron acceleration to relativistic energies in the Earth's outer radiation belt. *Geophysical Research Letters*, 30(16):5–8. doi: 10.1029/2003GL017698.

Meredith, N. P., Horne, R. B., Thorne, R. M., and Anderson, R. R. (2009). Survey of upper band chorus and ECH waves: Implications for the diffuse aurora. *Journal of Geophysical Research: Space Physics*, 114(7):1–11. doi: 10.1029/2009JA014230.

Meredith, N. P., Horne, R. B., Sicard-Piet, A., Boscher, D., Yearby, K. H., Li, W., and Thorne, R. M. (2012). Global model of lower band and upper band chorus from multiple satellite observations. *Journal of Geophysical Research: Space Physics*, 117(10):1–14. doi: 10.1029/2012JA017978.

Miyashita, Y., Machida, S., Kamide, Y., Nagata, D., Liou, K., Fujimoto, M., Ieda, A., Saito, M. H., Russell, C. T., Christon, S. P., Nosé, M., Frey, H. U., Shinohara, I., Mukai, T., Saito, Y., and Hayakawa, H. (2009). A state-of-the-art picture of substorm-associated evolution of the near-Earth magnetotail obtained from superposed epoch analysis. *Journal of Geophysical Research: Space Physics*, 114(1). doi: 10.1029/2008JA013225.

Miyoshi, Y., Katoh, Y., Nishiyama, T., Sakanoi, T., Asamura, K., and Hirahara, M. (2010). Time of flight analysis of pulsating aurora electrons, considering wave-particle interactions with propagating whistler mode waves. *Journal of Geophysical Research: Space Physics*, 115(10):1–7. doi: 10.1029/2009JA015127.

Miyoshi, Y., Oyama, S., Saito, S., Kurita, S., Fujiwara, H., Kataoka, R., Ebihara, Y., Kletzing, C., Reeves, G., Santolik, O., Clilverd, M., Rodger, C. J., Turunen, E., and Tsuchiya, F. (2015a). Energetic electron precipitation associated with pulsating aurora: EISCAT and Van Allen Probe observations. *Journal of Geophysical Research : Space Physics*, 120:2754–2766. doi: 10.1002/2014JA020690.

Miyoshi, Y., Saito, S., Seki, K., Nishiyama, T., Kataoka, R., Asamura, K., Katoh, Y., Ebihara, Y., Sakanoi, T., Hirahara, M., Oyama, S., Kurita, S., and Santolik, O. (2015b). Relation between energy spectra of pulsating aurora electrons and frequency spectra of whistler-mode chorus waves. *Journal of Geophysical Research: Space Physics*, 120(9):7728–7736. doi: 10.1002/2015JA021562.

Miyoshi, Y., Hori, T., Shoji, M., Teramoto, M., Chang, T. F., Segawa, T., Umemura, N., Matsuda, S., Kurita, S., Keika, K., Miyashita, Y., Seki, K., Tanaka, Y., Nishitani, N., Kasahara, S., Yokota, S., Matsuoka, A., Kasahara, Y., Asamura, K., Takashima, T., and Shinohara, I. (2018a). The ERG Science Center. *Earth, Planets and Space*, 70(1). doi: 10.1186/s40623-018-0867-8.

Miyoshi, Y., Shinohara, I., and Jun, C.-W. The Level-2 orbit data of Exploration of energization and Radiation in Geospace (ERG) Arase satellite, 2018b.

Miyoshi, Y., Shinohara, I., and Jun, C.-W. The Level-3 orbit data of Exploration of energization and Radiation in Geospace (ERG) Arase satellite, 2018c.

Miyoshi, Y., Shinohara, I., Takashima, T., Asamura, K., Higashio, N., Mitani, T., Kasahara, S., Yokota, S., Kazama, Y., Wang, S.-Y., Tam, S. W. Y., Ho, P. T. P., Kasahara, Y., Kasaba, Y., Yagitani, S., Matsuoka, A., Kojima, H., Katoh, Y., Shiokawa, K., and Seki, K. (2018d). Geospace exploration project ERG. *Earth, Planets and Space*, 70(1):101. doi: 10.1186/s40623-018-0862-0.

Miyoshi, Y., Saito, S., Kurita, S., Asamura, K., Hosokawa, K., Sakanoi, T., Mitani, T., Ogawa, Y., Oyama, S., Tsuchiya, F., Jones, S. L., Jaynes, A. N., and Blake, J. B. (2020). Relativistic Electron Microbursts as High-Energy Tail of Pulsating Aurora Electrons. *Geophysical Research Letters*, 47(21). doi: 10.1029/2020GL090360.

Miyoshi, Y., Hosokawa, K., Kurita, S., Oyama, S. I., Ogawa, Y., Saito, S., Shinohara, I., Kero, A., Turunen, E., Verronen, P. T., Kasahara, S., Yokota, S., Mitani, T., Takashima, T., Higashio, N., Kasahara, Y., Matsuda, S., Tsuchiya, F., Kumamoto, A., Matsuoka, A., Hori, T., Keika, K., Shoji, M., Teramoto, M., Imajo, S., Jun, C., and Nakamura, S. (2021). Penetration of MeV electrons into the mesosphere accompanying pulsating aurorae. *Scientific Reports*, 11(1):1–9. doi: 10.1038/s41598-021-92611-3.

Moen, J., Gulbrandsen, N., Lorentzen, D. A., and Carlson, H. C. (2007). On the MLT distribution of F region polar cap patches at night. *Geophysical Research Letters*, 34(14):7–10. doi: 10.1029/2007GL029632.

Nagai, T., Fujimoto, M., Saito, Y., Machida, S., Terasawa, T., Nakamura, R., Yamamoto, T., Mukai, T., Nishida, A., and Kokubun, S. (1998). Structure and dynamics of magnetic reconnection for substorm onsets with Geotail observations. *Journal of Geophysical Research*, 103(A3):4419–4440. doi: 10.1029/97JA02190.

Nakamura, R. and Oguti, T. (1987). Drifts of auroral structures and magnetospheric electric fields. *Journal of Geophysical Research*, 92(A10):11241. doi: 10.1029/ja092ia10p11241.

Newell, P. T., Sotirelis, T., and Wing, S. (2009). Diffuse, monoenergetic, and broadband aurora: The global precipitation budget. *Journal of Geophysical Research: Space Physics*, 114(9):1–20. doi: 10.1029/2009JA014326.

Ni, B., Thorne, R. M., Shprits, Y. Y., and Bortnik, J. (2008). Resonant scattering of plasma sheet electrons by whistler-mode chorus: Contribution to diffuse auroral precipitation. *Geophysical Research Letters*, 35(11):1–5. doi: 10.1029/2008GL034032.

Ni, B., Liang, J., Thorne, R. M., Angelopoulos, V., Horne, R. B., Kubyshkina, M., Spanswick, E., Donovan, E. F., and Lummerzheim, D. (2012). Efficient diffuse auroral electron scattering by electrostatic electron cyclotron harmonic waves in the outer magnetosphere: A detailed case study. *Journal of Geophysical Research: Space Physics*, 117(1):1–13. doi: 10.1029/2011JA017095.

Ni, B., Gu, X., Fu, S., Xiang, Z., and Lou, Y. (2017). A statistical survey of electrostatic electron cyclotron harmonic waves based on THEMIS FFF wave data. *Journal of Geophysical Research: Space Physics*, 122(3):3342–3353. doi: 10.1002/2016JA023433.

Nishimura, Y., Bortnik, J., Li, W., Thorne, R. M., Lyons, L. R., Angelopoulos, V., Mende, S. B., Bonnell, J. W., Le Contel, O., Cully, C., Ergun, R., and Auster, U. (2010). Identifying the driver of pulsating aurora. *Science*, 330(6000):81–84. doi: 10.1126/science.1193186.

Nishimura, Y., Bortnik, J., Li, W., Thorne, R. M., Chen, L., Lyons, L. R., Angelopoulos, V., Mende, S. B., Bonnell, J., Le Contel, O., Cully, C., Ergun, R., and Auster, U. (2011). Multievent study of the correlation between pulsating aurora and whistler mode chorus emissions. *Journal of Geophysical Research: Space Physics*, 116(11):1–11. doi: 10.1029/2011JA016876.

Nishimura, Y., Bortnik, J., Li, W., Liang, J., Thorne, R. M., Angelopoulos, V., Le Contel, O., Auster, U., and Bonnell, J. W. (2015). Chorus intensity modulation driven by time-varying field-aligned low-energy plasma. *Journal of Geophysical Research A: Space Physics*, 120(9):7433–7446. doi: 10.1002/2015JA021330.

Nishiyama, T., Miyoshi, Y., Katoh, Y., Sakanoi, T., Kataoka, R., and Okano, S. (2016). Substructures with luminosity modulation and horizontal oscillation in pulsating patch: Principal component analysis application to pulsating aurora. *Journal of Geophysical Research A: Space Physics*, 121(3):2360–2373. doi: 10.1002/2015JA022288.

Nygrén, T., Markkanen, M., Lehtinen, M., and Kaila, K. (1997). Application of stochastic inversion in auroral tomography. *Annales Geophysicae*, 14(11):1124–1133. doi: 10.1007/s00585-996-1124-1.

Obuchi, Y., Sakanoi, T., Yamazaki, A., Ino, T., Okano, S., Kasaba, Y., Hirahara, M., Kanai, Y., and Takeyama, N. (2008). Initial observations of auroras by the multi-spectral auroral camera on board the Reimei satellite. *Earth, Planets and Space*, 60(8):827–835. doi: 10.1186/BF03352834.

Ogawa, Y., Tanaka, Y., Kadokura, A., Hosokawa, K., Ebihara, Y., Motoba, T., Gustavsson, B., Brändström, U., Sato, Y., Oyama, S., Ozaki, M., Raita, T., Sigernes, F., Nozawa, S., Shiokawa, K., Kosch, M., Kauristie, K., Hall, C., Suzuki, S., Miyoshi, Y., Gerrard, A., Miyaoka, H., and Fujii, R. (2020). Development of low-cost multi-wavelength imager system for studies of aurora and airglow. *Polar Science*, 23(April 2019). doi: 10.1016/j.polar.2019.100501.

Omholt, A. (1957). The red and near-infra-red auroral spectrum. *Journal of Atmospheric and Solar-Terrestrial Physics*, 10:320–331.

Ono, T. and Miyoshi, Y. **太陽地球圏**. 共立出版, 2012. ISBN 978-4-320-04710-5.

Ono, T. (1993). Derivation of Energy Parameters of Precipitating Auroral Electrons by Using the Intensity Ratios of Auroral Emissions. *Journal of geomagnetism and geoelectricity*, 45(6):455–472. doi: https://doi.org/10.5636/jgg.45.455.

Oyama, S., Miyoshi, Y., Shiokawa, K., Kurihara, J., Tsuda, T. T., and Watkins, B. J. (2014). Height - dependent ionospheric variations in the vicinity of nightside poleward expanding aurora after substorm onset. *J. Geophys. Res. Space Physics*, 119:4146–4156. doi: 10.1002/2013JA019704.

Oyama, S.-i., Tsuda, T. T., Hosokawa, K., Ogawa, Y., Miyoshi, Y., Kurita, S., Kero, A. E., Fujii, R., Tanaka, Y., Mizuno, A., Kawabata, T., Gustavsson, B., and Leyser, T. (2018). Auroral molecular-emission effects on the atomic oxygen line at 777.4 nm. *Earth, Planets and Space*, 70(166). doi: 10.1186/s40623-018-0936-z.

Ozaki, M., Yagitani, S., Kasahara, Y., Kojima, H., Kasaba, Y., Kumamoto, A., Tsuchiya, F., Matsuda, S., Matsuoka, A., Sasaki, T., and Yumoto, T. (2018). Magnetic Search Coil (MSC) of Plasma Wave Experiment (PWE) aboard the Arase (ERG) satellite. *Earth, Planets and Space*, 70(1):1–13. doi: 10.1186/s40623-018-0837-1.

Picone, J. M., Hedin, A. E., Drob, D. P., and Aikin, A. C. (2002). NRLMSISE-00 empirical model of the atmosphere: Statistical comparisons and scientific issues. *Journal of Geophysical Research: Space Physics*, 107(A12):SIA 15–1 – SIA 15–16. doi: 10.1029/2002JA009430.

Press, W. H., Teukolsky, S. A., Vetterling, W. T., and Flannery, B. P. *Numerical Recipes in C (2nd Ed.): The Art of Scientific Computing*. Cambridge University Press, USA, 1992. ISBN 0521431085.

Rees, M. H. (1963). Auroral ionization and excitation by incident energetic electrons. *Planetary and Space Science*, 11(10):1209–1218. doi: 10.1016/0032-0633(63)90252-6.

Reidy, J. A., Horne, R. B., Glauert, S. A., Clilverd, M. A., Meredith, N. P., Woodfield, E. E., Ross, J. P., Allison, H. J., and Rodger, C. J. (2021). Comparing Electron Precipitation Fluxes Calculated From Pitch Angle Diffusion Coefficients to LEO Satellite Observations. *Journal of Geophysical Research: Space Physics*, 126(3). doi: 10.1029/2020JA028410.

Roederer, J. (1970). Dynamics of geomagnetically trapped radiation. *Physics and Chemistry in Space*, 2: 187. doi: 10.1007/978-3-642-49300-3.

Royrvik, O. and Davis, T. N. (1977). Pulsating Aurora: Local and Global Morphology. *Journal of Geophysical Research*, 82(29):4720–4740.

Russell, C. (1991). The Magnetosphere. *Annual Review of Earth and Planetary Sciences*, 19(1):169–182. doi: 10.1146/annurev.earth.19.1.169.

Saito, Y., Machida, S., Hirahara, M., Mukai, T., and Miyaoka, H. (1992). Rocket observation of electron fluxes over a pulsating aurora. *Planetary and Space Science*, 40(8):1043–1054. doi: 10.1016/0032-0633(92)90033-K.

Sakanoi, T., Okano, S., Obuchi, Y., Kobayashi, T., Ejiri, M., Asamura, K., and Hirahara, M. (2003). Development of the multi-spectral auroral camera onboard the INDEX satellite. *Advances in Space Research*, 32(3):379–384. doi: 10.1016/S0273-1177(03)90276-6.

Samara, M., Michell, R. G., and Redmon, R. J. (2015). Low-altitude satellite measurements of pulsating auroral electrons. *Journal of Geophysical Research A: Space Physics*, 120(9):8111–8124. doi: 10.1002/2015JA021292.

Sandahl, I., Eliasson, L., and Lundin, R. (1980). Rocket observations of precipitating electrons over a pulsating aurora. *Geophysical Research Letters*, 7(5):309–312. doi: 10.1029/GL007i005p00309.

Sangalli, L., Partamies, N., Syrjäsuo, M., Enell, C. F., Kauristie, K., and Mäkinen, S. (2011). Performance study of the new EMCCD-based all-sky cameras for auroral imaging. *International Journal of Remote Sensing*, 32(11):2987–3003. doi: 10.1080/01431161.2010.541505.

Santolík, O., Parrot, M., and Lefeuvre, F. (2003). Singular value decomposition methods for wave propagation analysis. *Radio Science*, 38(1):1–13. doi: 10.1029/2000RS002523.

Semeter, J. and Kamalabadi, F. (2005). Determination of primary electron spectra from incoherent scatter radar measurements of the auroral e region. *Radio Science*, 40(2):n/a–n/a. doi: 10.1029/2004RS003042.

Sergienko, T. and Ivanov, V. (1993). A new approach to calculate the excitation of atmospheric gases by auroral electron impact. *Annales Geophysicae- European Geophysical Society*, 11(8):717–727.

Sheeley, B. W., Moldwin, M. B., Rassoul, H. K., and Anderson, R. R. (2001). An empirical plasmasphere and trough density model: VRESS observations. *Journal of Geophysical Research*, 106(A11):25631–25641. doi: http://dx.doi.org/10.1029/2000JA000286.

Shprits, Y. Y. and Ni, B. (2009). Dependence of the quasi-linear scattering rates on the wave normal distribution of chorus waves. *Journal of Geophysical Research: Space Physics*, 114(11):1–10. doi: 10.1029/2009JA014223.

Shprits, Y. Y., Thorne, R. M., Horne, R. B., and Summers, D. (2006). Bounce-averaged diffusion coefficients for field-aligned chorus waves. *Journal of Geophysical Research: Space Physics*, 111(10):1–6. doi: 10.1029/2006JA011725.

Smith, M. J., Bryant, D. A., and Edwards, T. (1980). Pulsations in auroral electrons and positive ions. *Journal of Atmospheric and Terrestrial Physics*, 42(2):167–178. doi: 10.1016/0021-9169(80)90077-X.

Solomon, S. C., Hays, P. B., and Abreu, V. J. (1988). The auroral 6300 Å emission : observations and modeling. *J. Geophys. Res.*, 93:9867–9882. doi: 10.1029/JA093iA09p09867.

Stenbaek-Nielsen, H. C. and Hallinan, T. J. (1979). Pulsating auroras: Evidence for noncollisional thermalization of precipitating electrons. *Journal of Geophysical Research*, 84(A7):3257–3271. doi: 10.1029/JA084iA07p03257.

Stone, M. (1974). Cross-validatory choice and assessment of statistical predictions (with discussion). *Journal of the Royal Statistical Society: Series B (Methodological)*, 38(1):102–102. doi: 10.1111/j.2517-6161.1976.tb01573.x.

Su, Z., Zheng, H., and Wang, S. (2009). Evolution of electron pitch angle distribution due to interactions with whistler mode chorus following substorm injections. *Journal of Geophysical Research: Space Physics*, 114(8):1–10. doi: 10.1029/2009JA014269.

Su, Z., Zheng, H., and Wang, S. (2010). A parametric study on the diffuse auroral precipitation by resonant interaction with whistler mode chorus. *Journal of Geophysical Research: Space Physics*, 115(A5):1–22. doi: 10.1029/2009JA014759.

Sugiyama, H., Singh, S., Omura, Y., Shoji, M., Nunn, D., and Summers, D. (2015). Electromagnetic ion cyclotron waves in the Earth's magnetosphere with a kappa-Maxwellian particle distribution. *Journal of Geophysical Research A: Space Physics*, 120(10):8426–8439. doi: 10.1002/2015JA021346.

Summers, D., Tang, R., and Thorne, R. M. (2009). Limit on stably trapped particle fluxes in planetary magnetospheres. *Journal of Geophysical Research: Space Physics*, 114(10):1–21. doi: 10.1029/2009JA014428.

Summers, D., Tang, R., and Omura, Y. (2011). Effects of nonlinear wave growth on extreme radiation belt electron fluxes. *Journal of Geophysical Research: Space Physics*, 116(10):1–15. doi: 10.1029/2011JA016602.

Swift, D. W. (1981). Mechanisms for auroral precipitation: A review. *Reviews of Geophysics*, 19(1):185–211. doi: 10.1029/RG019i001p00185.

Tanaka, Y. M., Aso, T., Gustavsson, B., Tanabe, K., Ogawa, Y., Kadokura, A., Miyaoka, H., Sergienko, T., Brändström, U., and Sandahl, I. (2011). Feasibility study on Generalized-Aurora Computed Tomography. *Annales Geophysicae*, 29(3):551–562. doi: 10.5194/angeo-29-551-2011.

Tao, X., Thorne, R. M., Li, W., Ni, B., Meredith, N. P., and Horne, R. B. (2011). Evolution of electron pitch angle distributions following injection from the plasma sheet. *Journal of Geophysical Research: Space Physics*, 116(4):1–8. doi: 10.1029/2010JA016245.

Tesema, F., Partamies, N., Tyssøy, H. N., Kero, A., Smith-Johnsen, C., and Smith ‐ Johnsen, C. (2020a). Observations of electron precipitation during pulsating aurora and its chemical impact. *Journal of Geophysical Research: Space Physics*, 125(6):e2019JA027713. doi: 10.1029/2019ja027713.

Tesema, F., Partamies, N., Tyssøy, H. N., and Mckay, D. (2020b). Observations of precipitation energies during different types of pulsating aurora. *Annales Geophysicae*, 38(6):1191–1202. doi: 10.5194/angeo-38-1191-2020.

Thorne, R. M. (1977). Energetic radiation belt electron precipitation: A natural depletion mechanism for stratospheric ozone. *Science*, 195(4275):287–289. doi: 10.1126/science.195.4275.287.

Thorne, R. M. (2010). Radiation belt dynamics: The importance of wave-particle interactions. *Geophysical Research Letters*, 37(22):1–7. doi: 10.1029/2010GL044990.

Thorne, R. M., Shprits, Y. Y., Meredith, N. P., Horne, R. B., Li, W., and Lyons, L. R. (2007). Refilling of the slot region between the inner and outer electron radiation belts during geomagnetic storms. *Journal of Geophysical Research: Space Physics*, 112(6):1–11. doi: 10.1029/2006JA012176.

Thorne, R. M., Ni, B., Tao, X., Chen, L., Li, W., Meredith, N. P., Horne, R. B., and Shprits, Y. Y. (2013). Correction to " Resonant scattering of plasma sheet electrons leading to diffuse auroral precipitation : 1 . Evaluation for electrostatic electron cyclotron harmonic waves, " " Resonant scattering of plasma sheet electrons leading to diffuse auroral precip. *Journal of Geophysical Research : Space Physics*, 118: 839–842. doi: 10.1002/jgra.50154.

Torrence, C. and Compo, G. P. (1998). A Practical Guide to Wavelet Analysis. *Bulletin of the American Meteorological Society*, 79(1):61–78. doi: 10.1175/1520-0477(1998)079⟨0061:APGTWA⟩2.0.CO;2.

Tripathi, A. K., Singhal, R. P., and Singh, K. P. (2011). Pitch-angle diffusion coefficients from resonant interactions with electrostatic electron cyclotron harmonic waves in planetary magnetospheres. *Annales Geophysicae*, 29(2):321–330. doi: 10.5194/angeo-29-321-2011.

Tripathi, A. K., Singhal, R. P., Singh, K. P., and Singh, O. N. (2013). Diffuse auroral precipitation by resonant interaction with electron cyclotron harmonic and whistler mode waves. *Journal of Atmospheric and Solar-Terrestrial Physics*, 97:125–134. doi: 10.1016/j.jastp.2013.01.013.

Tsuda, T. T., Li, C., Hamada, S., Hosokawa, K., Oyama, S. I., Nozawa, S., Kawabata, T., Mizuno, A., Kurihara, J., Nishiyama, T., and Kosch, M. J. (2020). OI 630.0-nm and N2 1PG Emissions in Pulsating Aurora Events Observed by an Optical Spectrograph at Tromsø, Norway. *Journal of Geophysical Research: Space Physics*, 125(12):1–11. doi: 10.1029/2020JA028250.

Tsurutani, B. T. and Smith, E. J. (1974). Postmidnight Chorus : A Substorm Phenomenon. *Journal of Geophysical Research*, 79(1):118–127. doi: 10.1029/JA079i001p00118.

Tsyganenko, N. A. and Sitnov, M. I. (2005). Modeling the dynamics of the inner magnetosphere during strong geomagnetic storms. *Journal of Geophysical Research: Space Physics*, 110(A3):1–16. doi: 10.1029/2004JA010798.

Turunen, E., Kero, A., Verronen, P. T., Miyoshi, Y., Oyama, S. I., and Saito, S. (2016). Mesospheric ozone destruction by high-energy electron precipitation associated with pulsating aurora. *Journal of Geophysical Research*, 121(19):11852–11861. doi: 10.1002/2016JD025015.

Van Allen, J. and Frank, L. (1959). Radiation Around the Earth to a Radial Distance of 107,400 km. *Nature*, 183:430–434. doi: https://doi.org/10.1038/183430a0.

Vickrey, J. F., Vondrak, R. R., and Matthews, S. J. (1982). Energy deposition by precipitating particles and Joule dissipation in the auroral ionosphere. *Journal of Geophysical Research: Space Physics*, 87(A7): 5184–5196. doi: 10.1029/ja087ia07p05184.

Walls, F. L. and Dunn, G. H. (1974). Measurement of total cross sections for electron recombination with NO + and O 2 + using ion storage techniques. *Journal of Geophysical Research*, 79(13):1911–1915. doi: 10.1029/ja079i013p01911.

Walt, M. *Introduction to Geomagnetically Trapped Radiation*. Cambridge University Press, nov 1994. doi: 10.1017/CBO9780511524981.

Whalen, B. A., Miller, J. R., and McDiarmid, I. B. (1971). Energetic particle measurements in a pulsating aurora. *NACA TN No. 1326*, 76(4):978–986. doi: 10.1029/JA076i004p00978.

Yamamoto, T. (1988). On the temporal fluctuations of pulsating auroral luminosity. *Journal of Geophysical Research*, 93(A2):897–911. doi: 10.1029/JA093iA02p00897.

Yang, B., Spanswick, E., Liang, J., Grono, E., and Donovan, E. (2019). Responses of Different Types of Pulsating Aurora in Cosmic Noise Absorption. *Geophysical Research Letters*, 46(11):5717–5724. doi: 10.1029/2019GL083289.

Young, S. L., Denton, R. E., Anderson, B. J., and Hudson, M. K. (2008). Magnetic field line curvature induced pitch angle diffusion in the inner magnetosphere. *Journal of Geophysical Research: Space Physics*, 113(3):A03210. doi: 10.1029/2006JA012133.

Zhang, X., Angelopoulos, V., Ni, B., Thorne, R. M., and Horne, R. B. (2014). Extent of ECH wave emissions in the Earth's magnetotail. *Journal of Geophysical Research: Space Physics*, 119(7):5561–5574. doi: 10.1002/2014JA019931.

Zhou, Q., Xiao, F., Yang, C., Liu, S., He, Y., Baker, D. N., Spence, H. E., Reeves, G. D., and Funsten, H. O. (2017). Generation of lower and upper bands of electrostatic electron cyclotron harmonic waves in the Van Allen radiation belts. *Geophysical Research Letters*, 44(11):5251–5258. doi: 10.1002/2017GL073051.